Numerical Studies of Quantum Spin Systems

Dissertation zur Erlangung des
naturwissenschaftlichen Doktorgrades
der Julius-Maximilians-Universität Würzburg

11. Dezember 2007

vorgelegt von

Christian Brünger

aus Bad Oeynhausen

Würzburg 2007

Eingereicht am: 11. Dezember 2007
bei der Fakultät für Physik und Astronomie

1. Gutachter: Prof. Dr. Fakher Assaad
2. Gutachter: Prof. Dr. Mikhail Kiselev
der Dissertation

1. Prüfer: Prof. Dr. Fakher Assaad
2. Prüfer: Prof. Dr. Mikhail Kiselev
3. Prüfer: Prof. Dr. Ralph Claessen
im Promotionskolloquium

Tag des Promotionskolloquiums: 15. Februar 2008

Doktorurkunde ausgehändigt am:

Abstract

The understanding of matter does not only require a precise analysis of individual characteristics of the fundamental constituents, but also the study of their collective behavior. Solid state physics, and in particular research in strongly correlated electron systems, deals with such collective phenomena. The properties of the electrons, charge and spin quantum numbers, do not on their own explain the rich world of states of matter, however mutual interactions lead to various states or *phases* of matter. This work focuses on phases in quantum spin systems. On the basis of the Heisenberg model one (1D) and two dimensional (2D) spin lattices are investigated.

In a first part the bilayer Heisenberg Model and the 2D Kondo necklace model are studied. Both models exhibit a quantum phase transition between an ordered and disordered phase. For small interlayer couplings the models have antiferromagnetic long-range order, which is destroyed by increasing the coupling. However, even in the disordered phase the models show global features in terms of collective excitations called magnons. Coming from the disordered phase the gapped magnons condense at a critical coupling and form the order of the ordered phase. Here, another interesting question arises, namely that of the coupling of a single doped hole to such critical fluctuations. A self-consistent Born approximation predicts that the doped hole couples to the magnons such that the quasiparticle residue vanishes at the quantum critical point. In this work the delicate question about the fate of the quasiparticle residue across the quantum phase transition is also tackled by means of large scale quantum Monte Carlo simulations. Furthermore the dynamics of a single hole doped in the magnetic background is investigated.

In the second part an analysis of the spiral staircase Heisenberg ladder is presented. The ladder consists of two ferromagnetic coupled spin-1/2 chains, where the coupling within the second chain can be tuned by twisting the ladder. For large interleg coupling the spins on a rung form triplets and the ladder can be understood as an effective spin-1 chain. Hence, within this model the crossover between an ungapped spin-1/2 system and a gapped spin-1 system can be studied. In this work the emphasis is on the opening of the spin gap with respect to the ferromagnetic rung coupling. It is shown that there are essential differences in the scaling behavior of the spin gap depending on the twist of the model. The origin of the different scaling behavior lies in a new energy scale which emerges in the low coupling

region of strongly twisted ladders where the coupling along the second leg almost vanishes. The new energy scale can be interpreted by an RKKY-like interaction which is mediated via the spins on the first leg. This so-called Suhl-Nakamura interaction induces long-range correlation which causes a different scaling behavior. Moreover, by means of the string order parameter it is shown, that the system remains in the Haldane phase within the whole parameter range although the spin gap scales differently.

The tools which are used for the analyses are mainly large scale quantum Monte Carlo methods, but also exact diagonalization techniques as well as mean field approaches.

Kurzfassung

Für das Verständnis von Materie reicht es allein nicht aus, sich auf die Untersuchung der fundamentalen Einzelbausteine zu beschränken. Ebenso wichtig ist die Betrachtung des kollektiven Verhaltens aller Elemente. Die Festkörperphysik und insbesondere die Analyse stark korrelierter Elektronensysteme beschäftigt sich mit diesen kollektiven Phänomenen. So erklären die Eigenschaften eines einzelnen Elektrons, wie Ladung und Spin, nicht die verschiendenartigen Formen der Materie. Erst die gegenseitige Wechselwirkung der Elektronen ermöglicht eine Vielfalt von Zuständen bzw. Phasen. Diese Arbeit richtet ihr Augenmerk auf Phasen in Quantenspinsystemen. Auf der Basis des Heisenberg-Modells werden ein- und zweidimensionale Spingitter untersucht.

Der erste Teil der Arbeit widmet sich der Untersuchung des Bilayer-Heisenberg-Modells und des zweidimensionalen Kondo-Necklace-Modells. Beide Modelle weisen einen Quantenphasenübergang zwischen einer geordneten und einer ungeordneten Phase auf. Ist die Kopplung der Ebenen eines Modells schwach, so befindet sich das System in einer antiferromagnetisch geordneten Phase. Diese langreichweitige Ordnung wird bei zunehmender Kopplung zerstört. Aber auch in der magnetisch ungeordneten Phase weist das System ein kollektives Verhalten in Form von Spinanregungen, auch Magnonen genannt, auf. Hier sind die Anregungen durch eine Energielücke vom Grundzustand getrennt, welche sich jedoch bei schwächer werdender Kopplung schließt. Dies führt dazu, dass die Magnonen am quantenkritischen Punkt kondensieren und die Ordnung der geordneten Phase bilden. In dieser Arbeit richtet sich das Interesse insbesondere auf die Kopplung der kritischen Fluktuationen an ein in das System eingebundenes Loch. Mittels eines selbstkonsistenten Born'schen Näherungsverfahrens wird gezeigt, dass das Loch mit den Magnonen derart wechselwirkt, dass dessen Quasiteilchengewicht am quantenkritischen Punkt verschwindet. Um diesen Aspekt weiter zu untersuchen, wird das Verhalten des Quasiteilchengewichts im Bereich der kritischen Kopplung auch mit Quanten-Monte-Carlo-Methoden analysiert. Desweiteren werden die dynamischen Eigenschaften des Loches im magnetischen Hintergrund untersucht.

Im zweiten Teil dieser Arbeit gilt das Interesse der Untersuchung des Spiral-Staircase-Heisenberg-Modells. Dieses besteht aus zwei, zu einer Spinleiter ferromagnetisch gekopplten Spin-1/2-Ketten, wobei die antiferromagnetische Kopplung innerhalb der zweiten

Kette durch Windung der Leiter variiert werden kann. Bei starker Kopplung der Leiterbeine formieren sich die Spins der Sprossen zu Tripletts, und die gesamte Leiter kann als effektive Spin-1-Kette aufgefasst werden. Dieses Modell eignet sich somit, den Übergang zwischen einer Spin-1/2-Kette ohne Spinlücke und einer Spin-1-Kette mit Spinlücke zu studieren. Besondere Beachtung ist dem Öffnen der Spinlücke in Abhängigkeit der ferromagnetischen Kopplung zwischen den Leiterbeinen geboten. Es stellt sich heraus, dass das System, abhängig von der Leiterwindung, wesentliche Unterschiede im Skalierungsverhalten der Spinlücke aufweist. Der Ursprung des unterschiedlichen Skalierungsverhaltens ist auf eine bei stark gewundener Leiter im Bereich schwacher Kopplung auftretende neue Energieskala zurückzuführen. Diese kann durch einen der RKKY-Wechselwirkung sehr ähnlichen indirekten Kopplungsmechanismus zwischen den Spins des zweiten Leiterbeines vermittelt durch die Polarisation der Spins des ersten Leiterbeines erklärt werden. Diese sogenannte Suhl-Nakamura Wechselwirkung bewirkt langreichweitige Korrelationen zwischen den Spins und ist ursächlich für das unterschiedliche Skalierungsverhalten der Spinlücke. Desweiteren wird mittels der String-Order-Parameter gezeigt, dass das Spiral-Staircase-Heisenberg-Modell trotz des unterschiedlichen Skalierungsverhaltens der Spinlücke und unabhängig von der Wahl der Parameter sich stets in der Haldane-Phase befindet.

Die Analyse der Modelle bedient sich hauptsächlich Quanten-Monte-Carlo-Methoden, aber auch exakter Diagonalisierungstechniken, sowie auf Molekularfeldnäherungen gestützten Rechnungen.

Contents

1 Introduction **9**

2 Quantum Phases and Phase Transitions **17**
- 2.1 Basic Concepts in General 17
- 2.2 Quantum Phase Transitions 19
- 2.3 The Antiferromagnetic Phase 21
- 2.4 The Haldane Phase 23

3 Quantum Monte Carlo **27**
- 3.1 Path Integral Formulation and World Lines 28
- 3.2 Monte Carlo Sampling 31
- 3.3 Implementation of Single Hole Dynamics 34
- 3.4 Implementation of Observables 36
  - 3.4.1 Energy 37
  - 3.4.2 Spin Correlation Function 38
  - 3.4.3 String Order Parameters 39
  - 3.4.4 Spin Stiffness 39

4 Exact Diagonalization **41**
- 4.1 Basic Mathematical Principles 41
- 4.2 Lanczos Method 43
- 4.3 Dynamical Properties 44

5 The Kondo Necklace and Bilayer Heisenberg Model on a Square Lattice **47**
- 5.1 Quantum Phase Transition 47
- 5.2 Spin Dynamics in the BHM 49
  - 5.2.1 Dynamical Spin Susceptibility 50
  - 5.2.2 Bond Mean Field Approach 52
- 5.3 Single Hole Dynamics 54
  - 5.3.1 Bond Mean Field Approach with Single Hole 54
  - 5.3.2 Spectra and Effective Mass of a Mobile Hole 57

5.4 Quasiparticle Residue . . . 63
5.4.1 Analytical Approach . . . 63
5.4.2 QMC Approach . . . 66

6 The Spiral Staircase Heisenberg Model 71
6.1 Jordan-Wigner Mean Field Approach . . . 73
6.1.1 Ladder System . . . 74
6.1.2 1D Kondo Necklace . . . 78
6.2 Exact Diagonalization Analysis . . . 80
6.3 Quantum Monte Carlo Analysis . . . 84
6.3.1 Spin-Spin Correlations . . . 84
6.3.2 Spin Gap . . . 87
6.3.3 String Order Parameters . . . 89

Summary 93

A Calculation of First Order Self-Energy 97

B Scaling Behavior of the String Order Parameters 101
B.1 Temperature Scaling . . . 101
B.2 Size Scaling . . . 103

C Convergence of the Lanczos Method 105

D Loop Length and Correlation Time 109
D.1 Correlation Time for BHM . . . 109
D.2 Correlation Time for the 1D Kondo Necklace . . . 110

Acknowledgments 113

Bibliography 115

Curriculum Vitae 123

Introduction

1

Strongly correlated electron systems are one of the most interesting and recent problems in condensed matter physics. The study of correlation effects is essential for the understanding of many fascinating phenomena like high-temperature superconductivity [1] and the physics of heavy fermion systems [2, 3], for example. Strong correlations emerge if the electrostatic interaction energy between the electrons becomes of the order of their kinetic energy. Therefore in an appropriate model both the kinetic energy, leading to Bloch extended states, and the Coulomb repulsion, favoring localization, have to be included. The most fundamental model that takes the kinetic energy as well as the electrostatic repulsion energy into account in a complex many electron system was presented in the early 1960s by J. Hubbard [4]. The basic assumption of Hubbard was to neglect all inter atomic interactions due to the small overlap of the atomic wave functions, so that the electron-electron repulsion is restricted to the on-site interaction U between electrons on the same site. On the basis of the tight-binding approximation [5] the electrons are also allowed to tunnel between the atomic orbitals of neighboring sites. Thus, the kinetic energy is scaled by the transfer integral or hopping matrix element t. The Hubbard Hamiltonian in second quantization reads

$$\hat{\mathcal{H}}_{\text{Hub}} = -t \sum_{\langle ij \rangle} \sum_{\sigma} \left(\hat{c}^{\dagger}_{i,\sigma} \hat{c}_{j,\sigma} + \text{H. c.} \right) + \frac{U}{2} \sum_{i} \sum_{\sigma} \hat{n}_{i,\sigma} \hat{n}_{i,-\sigma} \ . \tag{1.1}$$

Here, $\hat{c}^{\dagger}_{i,\sigma}$ and $\hat{c}_{i,\sigma}$ create and annihilate electrons with spin σ at site i. $\hat{n}_{i,\sigma} = \hat{c}^{\dagger}_{i,\sigma} \hat{c}_{i,\sigma}$ stands for the particle density operator. Although the Hubbard model is for most physical systems an over simplified model, it is of great importance for the study of the interplay between the kinetic energy and the potential energy, the influence of the Pauli exclusion principle [6] and the effects of lattice structures [7]. In spite of its simplicity an analytic description of the ground state of the Hubbard model is only known for the one dimensional (1D) case [8, 9]. For higher dimensionality it is still an unsolved problem. Nevertheless, the Hubbard model is the basis of many low energy models including quantum spin systems which are the central subject of this work.

The low energy physics of the Hubbard model in the large-U regime near half filling is given by the t-J model [10, 11]. Taking the hopping term of Eq. (1.1) as a perturbation one obtains the effective t-J Hamiltonian where, due to the large on-site repulsion, double occupancy only appears as virtual intermediate states. Furthermore the so-called three-site-terms are neglected. They describe processes where an electron virtually hops to an occupied site, whilst obeying the Pauli exclusion principle, and finally ends up at a different unoccupied site. Those correlated hopping terms can be argued to be neglected near half filling since the density of holes is very small. The t-J model then reads

$$\hat{\mathcal{H}}_{tJ} = \hat{P}_S \left[-t \sum_{\langle ij \rangle} \sum_{\sigma} \left(\hat{c}^{\dagger}_{i,\sigma} \hat{c}_{i,\sigma} + \mathrm{H.\,c.} \right) + J \sum_{\langle ij \rangle} \left(\hat{\mathbf{S}}_i \cdot \hat{\mathbf{S}}_j - \tfrac{1}{4} \hat{n}_i \hat{n}_j \right) \right] \hat{P}_S \ . \tag{1.2}$$

Here, the second order term is scaled by $J \equiv 4t^2/U$. The operator $\hat{P}_S$ projects onto the subspace with no double occupancy. $\hat{n}_i = \sum_\sigma \hat{c}^{\dagger}_{i,\sigma} \hat{c}_{i,\sigma}$ denotes the occupation number operator and $\hat{\mathbf{S}}_i$ is the spin operator at site i with components

$$\hat{S}^z_i = \frac{1}{2} \left(\hat{c}^{\dagger}_{i,\uparrow} \hat{c}_{i,\uparrow} - \hat{c}^{\dagger}_{i,\downarrow} \hat{c}_{i,\downarrow} \right) \quad , \quad \hat{S}^+_i = \hat{c}^{\dagger}_{i,\uparrow} \hat{c}_{i,\downarrow} \quad \text{and} \quad \hat{S}^-_i = \hat{c}^{\dagger}_{i,\downarrow} \hat{c}_{i,\uparrow} \ . \tag{1.3}$$

Hence the very origin of *quantum spin* systems lies in the Coulomb repulsion. Since $J > 0$ one finds antiferromagnetic interaction within the Hubbard model. Such doped antiferromagnets are discussed in the context of high-temperature superconductivity in cooper oxides [1, 12, 13]. In section 3.3 the t-J model is used to implement the single hole dynamics into the considered spin model.

Exactly at half filling the charge fluctuations cease to exist, and the model maps onto a pure spin model described by the isotropic Heisenberg Hamiltonian:

$$\hat{\mathcal{H}}_{\mathrm{Heis}} = J \sum_{\langle ij \rangle} \hat{\mathbf{S}}_i \cdot \hat{\mathbf{S}}_j \ . \tag{1.4}$$

In a pure spin model the exchange constant J describes the magnetic coupling between neighboring spins and can be either positive (antiferromagnetic coupling) or negative (ferromagnetic coupling). Classically, the exchange coupling may be interpreted as the influence of the magnetic moments of the electrons on each other by dipol-dipol interaction. In fact the dipolar interaction is relatively weak and can be neglected. The underlying mechanisms of the magnetic order are based on pure quantum mechanical effects [11], such as the electron spin, the delocalization energy, Heisenberg's uncertainty principle [14] and Pauli's exclusion [6] principle, and of course the Coulomb repulsion.

A ferromagnetic (FM) ordering of spins causes an anti-symmetric orbital wave function: $\psi(\ldots \mathbf{r}_i \ldots \mathbf{r}_j \ldots) = -\psi(\ldots \mathbf{r}_j \ldots \mathbf{r}_i \ldots)$, where electrons i and j can never be at the same place: $\mathbf{r}_i \neq \mathbf{r}_j$. This reduces, in general, the Coulomb interaction energy and is the basic principle of Hund's rule [15]. On the other hand, an antiferromagnetic (AF) coupling $J > 0$

enables more delocalization of the electron, because the electron is not restricted by Pauli's exclusion principle. As a consequence of Heisenberg's uncertainty principle a delocalized electron reduces the momentum uncertainty, thus reducing the kinetic energy. Which of these effects is more significant and thus which kind of magnetic coupling is preferred depends on the molecular structure of the considered physical system. In general, FM ordering is favored if the orbitals are orthogonal but occupy the same region is space, whereas AF ordering is preferred if the orbitals are non-orthogonal but located in different regions in space [11].

In this work the focus is on pure spin models described in terms of the Heisenberg model. It is structured in two parts. The first part presented in chapter 5 discusses the single-hole dynamics in the two dimensional (2D) Kondo necklace model [see below] and bilayer Heisenberg model. In the second part (chapter 6) the 1D spiral staircase Heisenberg model is considered, and the question primarily addressed is the opening of the spin gap as a function of coupling.

The analyses in the first part are motivated by the modeling of heavy fermion systems. Such systems are based on an array of localized spin degrees of freedom coupled antiferromagnetically to conduction electrons and show competing interactions which lead to magnetic quantum phase transitions between an antiferromagnetically ordered and disordered phase as a function of the AF exchange interaction J. For large J the localized magnetic moments are screened by the conduction electrons. This so-called Kondo screening leads to a paramagnetic heavy fermion ground state. In contrast, the Ruderman-Kittel-Kasuya-Yosida (RKKY) interaction favors antiferromagnetic ordering and is dominant at small values of J. The RKKY [16, 17, 18, 19] interaction is an indirect exchange coupling between the localized spin degrees of freedom and is mediated by the polarization of the spins in the conduction band. It is given by $J_{\mathrm{RKKY}} \propto J_{\perp}^2 \chi(\mathbf{q}, \omega = 0)$ where $\chi(\mathbf{q}, \omega)$ corresponds to the spin susceptibility of the conduction electrons. Typically, heavy fermion systems are captured by the 2D Kondo lattice model (KLM) and its variations. In this work a very simplified situation is considered, namely that of a doped hole in the Kondo insulating state as realized by the Kondo necklace. However, it allows to investigate the form of the quasiparticle dispersion relation from strong to weak coupling.

The KLM emerges from the periodic Anderson model (PAM), which consists of localized orbitals (LO) with on-site Hubbard interaction U_f and extended orbitals (EO), which form a conduction band with dispersion $\varepsilon(\mathbf{p}) = -2t\left(\cos(p_x) + \cos(p_y)\right)$. The overlap between the LOs and the EOs within each unit cell is described by the hybridization matrix element V. For large U_f charge fluctuations on the localized orbitals becomes negligible and the PAM maps via the Schrieffer-Wolff transformation onto the KLM [20, 21]:

$$\hat{\mathcal{H}}_{\mathrm{KLM}} = \sum_{\mathbf{p},\sigma} \varepsilon(\mathbf{p}) \hat{c}^{\dagger}_{\mathbf{p},\sigma} \hat{c}_{\mathbf{p},\sigma} + \mathcal{J} \sum_{i} \hat{\mathbf{S}}^{c}_{\mathbf{i}} \cdot \hat{\mathbf{S}}^{f}_{\mathbf{i}} \ . \tag{1.5}$$

Here, $\hat{\mathbf{S}}^c_{\mathbf{i}}$ and $\hat{\mathbf{S}}^f_{\mathbf{i}}$ are spin-1/2 operators for the extended orbitals and the localized orbitals respectively. In the first term, which represents the hopping processes, the fermionic operators $\hat{c}^\dagger_{\mathbf{p},\sigma}$ ($\hat{c}_{\mathbf{p},\sigma}$) create (annihilate) electrons in the conduction band with wave vector $\mathbf{p}$ and z-component of spin σ. At half filling – one conduction electron per localized spin – the 2D KLM is an insulator and shows a magnetic order-disorder quantum phase transition at a critical value of $\mathcal{J}_c/t = 1.45 \pm 0.05$ [22].

By taking into account an additional Coulomb repulsion U between electrons within the conduction band, one obtains a modification of the KLM, the UKLM:

$$\hat{\mathcal{H}}_{\mathrm{UKLM}} = \sum_{\mathbf{p},\sigma} \varepsilon(\mathbf{p}) \hat{c}^\dagger_{\mathbf{p},\sigma} \hat{c}_{\mathbf{p},\sigma} + \mathcal{J} \sum_{i} \hat{\mathbf{S}}^c_{\mathbf{i}} \cdot \hat{\mathbf{S}}^f_{\mathbf{i}} + U \sum_{\mathbf{i}} \left(\hat{n}_{\mathbf{i},\uparrow} - \tfrac{1}{2}\right)\left(\hat{n}_{\mathbf{i},\downarrow} - \tfrac{1}{2}\right) . \qquad (1.6)$$

Here, $\hat{n}_{\mathbf{i},\sigma} = \hat{c}^\dagger_{\mathbf{i},\sigma}\hat{c}_{\mathbf{i},\sigma}$ is the density operator for electrons with spin σ in the conduction band. The additional Coulomb repulsion displaces the quantum critical point towards smaller value of $\mathcal{J}_c/t$. However, the physics, in particular the single hole dynamics, remains unchanged [23]. This allows to take the limit $U/t \to \infty$ to map the UKLM onto a Kondo necklace model (KNM) which one writes as

$$\hat{\mathcal{H}} = J_\perp \sum_{\mathbf{i}} \hat{\mathbf{S}}^{(1)}_{\mathbf{i}} \cdot \hat{\mathbf{S}}^{(2)}_{\mathbf{i}} + \sum_{\langle \mathbf{ij} \rangle} \sum_{m} J^{(m)}_{\parallel} \hat{\mathbf{S}}^{(m)}_{\mathbf{i}} \cdot \hat{\mathbf{S}}^{(m)}_{\mathbf{j}} . \qquad (1.7)$$

Here, $\hat{\mathbf{S}}^{(m)}_{\mathbf{i}}$ is a spin-1/2 operator, which acts on a spin degree of freedom at site $\mathbf{i}$. $J^{(m)}_{\parallel}$ stands for the intralayer exchange and the upper index $m = 1, 2$ labels the two different layers. The interlayer exchange, formerly the AF coupling $\mathcal{J}$ between LOs and EOs, is now characterized by $J_\perp$. Clearly, since the KNM is motivated from a strong coupling limit of the UKLM, one has to set:

$$J^{(1)}_{\parallel} \equiv J_\parallel \quad \text{and} \quad J^{(2)}_{\parallel} = 0 \qquad \text{(KNM)}. \qquad (1.8)$$

The above models all have in common that the only interaction between the localized spins stems from the RKKY interaction. This in turn leads to the fact that at $\mathcal{J} = 0$ for the KLM and UKLM or $J_\perp = 0$ for the KNM the ground state is macroscopically degenerate. This *pathology* is lifted in the bilayer Heisenberg model (BHM) in which an independent exchange between the localized spins is explicitly included in the Hamiltonian. Hence the isotropic BHM which takes the form of Eq. (1.7) with

$$J^{(1)}_{\parallel} = J^{(2)}_{\parallel} \equiv J_\parallel \qquad \text{(BHM)} \qquad (1.9)$$

is also considered. Both, the KNM and BHM, are sketched in Fig. 5.1 and are discussed in detail in section 5. For both models the discussion includes a numerical determination of the quantum critical point which separates the antiferromagnetically ordered and paramagnetic phase at zero temperature. It also covers an analysis of the spin dynamics in the

BHM. Furthermore the single particle spectral function is extensively studied. It turns out that there are significant differences between both models based on the additional spin coupling within the second layer of the BHM. Finally attention is turned to the fate of the quasiparticle residue across the quantum phase transition. Here, the results are obtained with a self-consistent Born approximation and large scale quantum Monte Carlo methods.

The second part of this work deals with a similar situation, but in lower dimension. Here, a spin-1/2 two leg ladder is considered, where the spins on a rung are coupled ferromagnetically ($J_\perp < 0$). Whereas the AF coupling ($J_\parallel > 0$) along the first leg is fixed, the coupling along the second leg can be tuned until it completely vanishes. The extreme case of *dangling* spins which are not coupled to each other within the second leg is called the 1D Kondo necklace, even if the coupling on the rungs is considered as FM. This model is captured by the following Heisenberg Hamiltonian:

$$\hat{\mathcal{H}} \;=\; J_\parallel \sum_i \left(\hat{\mathbf{S}}_{1,i} \cdot \hat{\mathbf{S}}_{1,i+1} + \cos^2\left(\theta/2\right) \hat{\mathbf{S}}_{2,i} \cdot \hat{\mathbf{S}}_{2,i+1} \right) + J_\perp \sum_i \hat{\mathbf{S}}_{1,i} \cdot \hat{\mathbf{S}}_{2,i} \; . \tag{1.10}$$

Here, $\hat{\mathbf{S}}_{\alpha,i}$ is a spin-1/2 operator acting on leg α and lattice site i. Geometrically, this model may be understood as a continuous twist deformation of an isotropic 2-leg ladder with interleg coupling $J_\parallel$ along leg 1 by an angle θ [see Fig. 6.1] and is called the spiral staircase Heisenberg (SSH) model. As a result of the deformation the coupling between neighboring sites along leg 2 is rescaled to the form $J_\parallel \cos^2\left(\theta/2\right)$.

The motivation of this study is given by the Haldane conjecture [24] proposed more than 20 years ago which states that the properties of $SU(2)$ symmetric AF spin-S Heisenberg chains are different for integer and half-integer spins. The excitations in AF Heisenberg chains with half-integer spins are gapless [25] whereas for integer spin chains a gap exists. The pure 1D AF spin-1/2 Heisenberg chain can be mapped onto a Luttinger liquid which allows to treat such chains by means of exact fermionization and bosonization methods, resulting in a well understood gapless phase [25]. In contrast, for the AF spin-1 Heisenberg chain it is widely accepted and extensively shown by numerical analyses [26, 27, 28, 29] that the excitations exhibit a gap. However, coupling identical chains to form a spin ladder allows to analyze intermediate systems and thus to study the crossover between an AF spin-1/2 and an AF spin-1 Heisenberg chain. Moreover, from the theoretical point of view the question arises of how the spin gap behaves if two unequivalent spin-1/2 chains are coupled. Especially the behavior of the spin gap for a single chain with dangling spins is a current controversy [30, 31, 32, 33].

It is known from the seminal bosonization work of Shelton, Nersesyan und Tsvelik [35] that the FM coupling of AF spin chains induces a Haldane gap which for weak interleg couplings is proportional to $J_\perp/J_\parallel$. When the spin velocity on one of the legs vanishes the bosonization methods fails since a simple formulation of the continuum limit on which

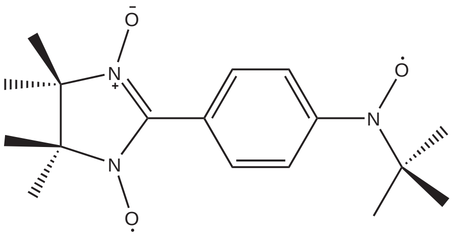

Figure 1.1: An experimental realization of the 1D Kondo necklace model is found in the organic biradical crystal PNNNO. (PNNNO $\hat{=}$ $2-[4'-(N-tert-\text{butyl}-N-\text{oxyamino})\text{phenyl}]-4,4,5,5-\text{tetramethyl}-4,5-\text{dihydro}-1H-\text{imidazol}-1-\text{oxyl}\ 3-\text{oxide})$ [34]

the approach relies breaks down. This poses the challenge to tackle this problem with other analytical and numerical methods. Beside this theoretical interest there is also an experimental motivation. The Kondo necklace ($\theta = \pi$) has been used for modeling a stable organic biradical crystal of PNNNO [34] [see Fig. 1.1]. A PNNNO molecule consists of two radical units, an $N - tert -$ butyl nitoxide unit ($tBu - NO$) and a nitronyl nitroxide (NN) unit. The units can be understood as single occupied molecular orbitals (SOMOs) each filled by an unpaired electron. In agreement with the rule of thumb that alignment of the spins is preferred for orbitals that occupy the same region in space, the spin degrees of freedom of these unpaired electrons couple ferromagnetically within the molecule. Furthermore the PNNNO molecules themselves form a lattice structure composed of one dimensional chains where the links corresponds to NN units which are coupled antiferromagnetically among each other. Whereas the coupling for an PNNNO model is of the order of $J_\perp/J_\parallel \simeq -44$ ($2J_\perp/k_B \simeq -638\,K$ and $2J_\parallel/k_B \simeq 14.5\,K$) [34] this work is mainly focused on the low coupling ($J_\perp \ll J_\parallel$) region of the SSH model. In section 6.1 Jordan-Wigner mean field calculations for the $SU(2)$ symmetric Heisenberg ladder and the 1D Kondo necklace are presented. Already on this approximate level significant differences in the scaling behavior of the spin gap become apparent. Furthermore, the results obtained by the mean field calculation are supported by exact diagonalization techniques and large scale quantum Monte Carlo methods. The different scaling behavior of the spin gap can be interpreted in terms of an emergent Suhl-Nakamura (SN) interaction in the weak coupling region of a strongly twisted ($\theta \simeq \pi$) ladder. This SN interaction [36, 37, 38] describes an indirect exchange coupling between the dangling spins via polarization effects of the spin degrees of freedom on leg 1. It is comparable to the RKKY interaction and takes the very similar form $J_{\text{SN}} \propto J_\perp^2 \chi(q, \omega = 0)$ where $\chi(q, \omega)$ is the spin susceptibility of the spins on leg 1. In addition, intermediate systems with $0 < \theta < \pi$ are also observed. Finally, by way of string order parameters an attempt is made to answer the question of whether or not the different scaling of the gap is also associated with different quantum phases.

The results presented in this work are obtained with different analytical and numerical techniques. The substantial analysis is done with large scale path integral quantum Monte Carlo simulations. Here the model is formulated in terms of world lines. The updating is done via the very efficient loop algorithm [39]. The autocorrelation length of the loop algorithm is investigated in appendix D. A short introduction to the world line formulation of spin systems and the implementation of observables into world lines is given in section 3. Numerical simulations generally are restricted to finite sized lattices, where boundary effects emerge beside bulk effects. The advantages of a Monte Carlo method is the ability to simulate comparatively large systems, where the effects of the boundaries are negligible or can be eliminated by finite size scaling. Another advantage of Monte Carlo simulations is given by the fact that they yield exact results. Here, *exact* means that the results just have a statistical error which can be arbitrarily reduced and depends on the amount of CPU time. The most prominent disadvantage of quantum Monte Carlo methods is the so-called minus sign problem which makes the simulation of certain models difficult or even unfeasible. However, in the non-frustrated spin systems dealt with in this work the minus sign problem is absent and the reader is referred to Ref. [40] for detailed informations. Another disadvantage of the QMC method is the difficulty of resolving very low energy scales which becomes explicitly apparent in chapter 6 where the spin gap of the SSH model is calculated. This disadvantage is lifted by using exact diagonalization (ED) techniques. Here, the problem is solved *exactly* in every sense. An introduction into the Lanczos method, which is the most established exact diagonalization technique for the determination of ground state properties, is given in chapter 4. The great disadvantage of the ED technique is that is only allows to compute very small systems, where often the behavior of the bulk system is not observable. Another method in the analysis of the discussed models is the mean field approach. In this approximative method the many diverse interactions are replaced by a *mean field*. In other words, the Hamiltonian of the model is expanded in fluctuations, where only the linear terms contribute. Fluctuations of higher order are neglected. This allows to solve this simplified model self-consistently. The advantage of the mean field approximation is given in its simplicity. It can be solved without huge computational effort. The disadvantage of the mean field approach is obvious: Since it it just an approximative method crucial mechanisms could be missed.

In the following section the work starts with a short introduction to phases and phase transitions. There, two quantum phases which become relevant in this work are especially emphasized: the antiferromagnetic phase and the Haldane phase.

Parts of this work are published or submitted for publication:

- C. Brünger and F. F. Assaad
  Single hole dynamics in the Kondo Necklace and Bilayer Heisenberg models on a square lattice
  Physical Review B **74**, 205107 (2006)
- C. Brünger, F. F. Assaad, S. Capponi, F. Alet, D. S. Aristov and M. N. Kiselev
  Spin gap and string order parameter in the ferromagnetic Spiral Staircase Heisenberg Ladder: a quantum Monte Carlo study
  accepted for publication in PHYSICAL REVIEW LETTERS.
  (Article is expected to be published in the January 11, 2008 issue.)
- C. Brünger, F. F. Assaad, S. Capponi, F. Alet, D. S. Aristov and M. N. Kiselev
  Twisting Ferromagnetic Spin Ladders
  to be submitted for publication in PHYSICAL REVIEW B
- S. Hochkeppel, T. C. Lang, C. Brünger, F. F. Assaad and W. Hanke
  Quantum Monte Carlo Studies of Strongly Correlated Electron Systems
  in *High Performance Computing in Science and Engineering, Garching 2007*
  in press (Springer-Verlag, 2007)

Quantum Phases and Phase Transitions

2

Different phases and phase transitions make the world rich and interesting. This becomes already obvious by the fact that one can skate on a lake during the winter and to go swimming in it in the summer time. Even more, phase transitions make the world possible since they seem to be very important for the origin of the observable universe [41]: "...indeed it is widely argued that the very existence of the observable universe is attributable to the phase change in the state of some pre-existing vacuum, and that the disposition of matter in and around galaxies should be understood in terms of fluctuations associated with some such transition ..." [42]. Also, and in particular, in solid state physics many different phases of matter are distinguishable. Besides different crystalline structures, which allow, for instance, that solids of carbon can be used for fossil burning as well as for decoration in the form of diamonds, several conducting and magnetic phases can emerge. In this work attention is turned towards different magnetic phases, however this chapter also gives an overview of the basic concepts of phases and phase transitions in general. At the end of this chapter a short introduction is given to antiferromagnetic phases and Haldane phases which are subjects in the main part of this work.

2.1 Basic Concepts in General

In nature matter emerges in different states of aggregation which can be transferred into each other by tuning external parameters like temperature and pressure, but also coupling and doping. One distinguishes between first order phase transitions, where a finite amount of latent heat has to be spent to initialize the transition, and continuous phase transitions. An example of a continuous phase transition is the transition between a paramagnetic phase and a ferromagnetic phase. For these kinds of transitions the system goes from a symmetric or disordered phase to an ordered phase with spontaneously broken symmetry. In this special case the underlying symmetry is the rotational symmetry in spin space which is broken in the ferromagnetic phase where a certain direction of the magnetic moments of the spins is preferred. Although many phase transitions in the thermodynamics of fluids

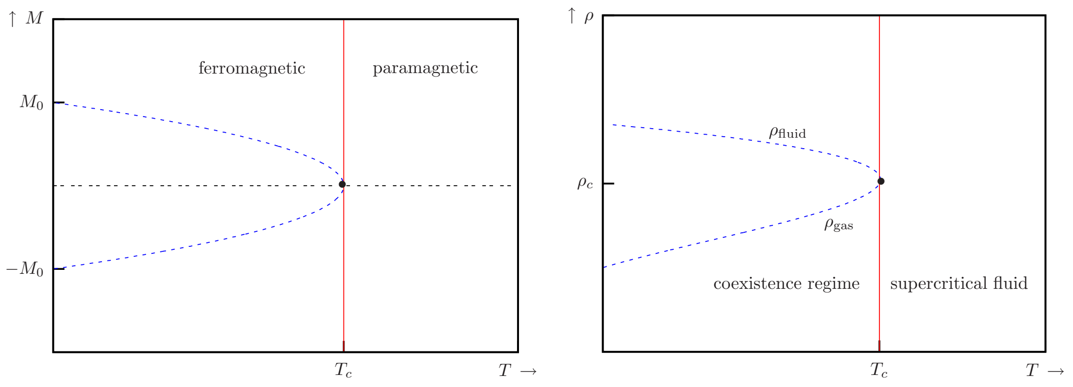

(a) Magnetic phase transition (b) Phase transition of a fluid

Figure 2.1: Example for universality: both phase diagrams show similar features. The ferromagnetic order is indicated by the magnetization M which is finite for $T < T_c$. The corresponding quantity in the liquid-gas diagram is given by the difference $\rho_{\text{fluid}} - \rho_c$ (or $\rho_c - \rho_{\text{gas}}$) between the fluid (or gas) density and the critical density.

are of first order, e. g. the boiling or freezing of water, one also finds a continuous phase transition by going along the coexistence curve of a liquid-gas diagram. At the critical point one enters a new phase, called supercritical fluid, which is characterized by only a single stable phase. The remarkable phenomenon is that the transitions between all these phases show similar fundamental characteristics [see Fig. 2.1]. In particular this implies that in the vicinity of the critical points the topology of the phase diagrams of various systems look quite similar, and the critical exponents which characterize the behavior of the system in the critical region seem to be identical for many different systems [43, 44]. This generality is pointed out in the so-called *universality hypothesis*: "All phase transition problems can be divided into a number of different classes depending upon the dimensionality of the system and the symmetries of the ordered state. Within each class all phase transitions have identical behavior in the critical region. Only the names of the thermodynamic variables are changed " [45]. The universality can be understood by the fact that in the vicinity of the phase transition the thermal or quantum fluctuations lead to long range correlations, characterized by the divergence of the correlation length ξ. Thus, in this critical region the system behaves collectively and only global features like dimensionality and symmetry are significant.

As a consequence of the divergence of the correlation length the systems behaves equally on all length scales. This means in particular that microscopic components can be combined to a cluster and an effective interaction can be introduced, so that the rescaled systems shows up unchanged. This conservation property is known as scale invariance and has a mathematical description by the renormalization group (RG) theory. The RG theory was formulated by K. G. Wilson [46] who received the Nobel price in 1982 for his seminal work [47]. A major result of the RG theory is that it provides a theoretical basis for the so-called scaling laws. Even more, the RG permits the numerical calculation of the critical exponents. One of these scaling laws describes the behavior of the order parameter within the critical region. The order parameter is a quantity which is usually finite within the ordered phase and zero within the disordered phase. Therefore it is used to indicate the critical point of a phase transition. For a ferromagnetic system a possible order parameter is given by the magnetization M [see Fig. 2.1(a)], for the phase transition in the liquid-gas diagram this could be the difference $\rho_{\text{fluid}} - \rho_c$ (or $\rho_c - \rho_{\text{fluid}}$) between the fluid (or gas) density and the critical density [see Fig. 2.1(b)]. However, in general the order parameters are not unique. For an arbitrary order parameter $\mathcal{O}$ one obtains the following power law:

$$\mathcal{O} \propto \Theta(g - g_c)\, |g - g_c|^{\beta} \quad . \tag{2.1}$$

Here, $g - g_c$ is a dimensionless *distance* to the critical point which can be associated with some kind of temperature or coupling. Θ denotes the Heaviside function and β stands for the critical exponent.

2.2 Quantum Phase Transitions

The phase transitions which one usually observes are mostly triggered by the temperature, and the macroscopic order at a critical temperature T_c is destroyed due to thermal fluctuations. But phase transitions can also take place at zero temperature [48]. Here a non-thermal control parameter, such as coupling or doping, determines the phase and can be tuned to access the transition point. Since at zero temperature no thermal fluctuations are present such transitions are induced by quantum fluctuation: Instead of exchanging energy with a heat bath, the temporary microscopic fluctuations in energy emerge due to the Heisenberg uncertainty principle.

Generally in a quantum system both thermal and quantum fluctuations occur. However, for finite temperatures the thermal fluctuations dominate in the majority of cases. Only in the absence of thermal fluctuations do the quantum fluctuations become significant, therefore such phase transitions at zero temperature are called *quantum* phase transitions. This does not imply that quantum mechanical effects are insignificant for finite temperature phase transitions. For example, the emergence of a superconducting phase or a superfluid phase can only be understood by quantum mechanics, however these phase transitions are triggered by thermal fluctuations and thus the phase transitions are classified as *classical* [48, 49]. Fig. 2.2 shows a possible phase diagram where both, thermal and quantum fluctuations, destroy the order of the ordered phase. Classically fluctuations can be understood as a temporal sequence of different states [49]. In the Ising model, for example,

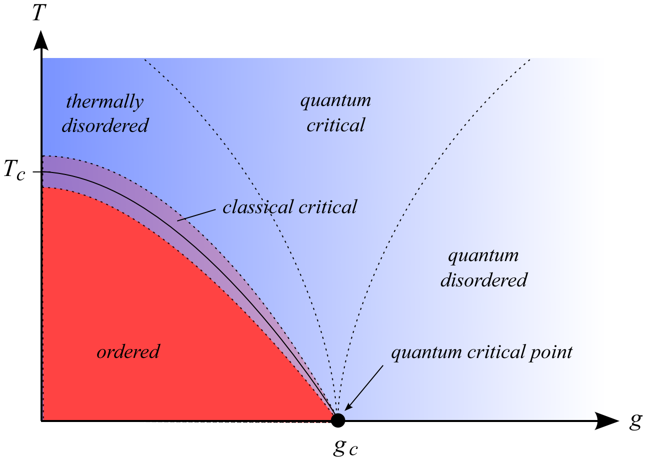

Figure 2.2: Phase diagram of a quantum mechanical system. The temperature T can be tuned to induce a classical phase transition by thermal fluctuations. A quantum phase transition occurs when a non-thermal parameter g like coupling or doping is triggered at zero temperature. The disordered phase splits into three regions with different physical properties. However, these regions are separated by gradual crossovers and not by phase transitions [49].

this could be a sequence where the spins temporarily fluctuate between up and down. The expectation value of the magnetization is then given by an averaging over the whole temporal sequence with a certain variance which indicates the fluctuations. In a quantum mechanical magnetic system the actual state is already a superposition of up-spins and down-spins. The expectation value is now determined by this single superposed state. Nevertheless, the fluctuations in terms of the variance are still finite which is a result of the non-commutativity of the quantum mechanical operators.

Therefore one may suggest that the quantum fluctuations do not take place in real time. Indeed, formally the time dimension can be analytically continued and the quantum fluctuations can then be understood as fluctuations in imaginary time. This formalism is used in section 3.1 where the partition function of a quantum mechanical system is interpreted as a path integral in imaginary time.

In classical statistical mechanics the thermodynamic properties can be derived from the partition function given by

$$Z = \int \mathrm{d}^d\mathbf{p} \int \mathrm{d}^d\mathbf{q}\; e^{-\beta\mathcal{H}(\mathbf{p},\mathbf{q})} \;, \tag{2.2}$$

where $\mathcal{H}(\mathbf{p},\mathbf{q})$ is the classical Hamilton function depending on the momentum $\mathbf{p}$ and the space coordinate $\mathbf{q}$ which splits into a kinetic part $\mathcal{T}(\mathbf{p})$ and a potential part $\mathcal{V}(\mathbf{q})$. Since classically $\mathcal{T}$ and $\mathcal{V}$ commute, the partition function factorizes: $Z = Z_{\mathcal{T}} Z_{\mathcal{V}}$. To study classical phase transitions it is usually sufficient to use effective time-independent theories where the kinetic part of the partition function does not contribute [50]. Therefore, the configuration space with dimensionality d covers only the d space dimensions. In quantum mechanics the situation is different. Here, the partition function is given by

$$Z = \mathrm{Tr}\, e^{-\beta\hat{\mathcal{H}}} \;. \tag{2.3}$$

In contrast to the classical case the partition function does not factorize, which is often expressed by saying *statics and dynamics do not decouple* [51], and the dynamics has to be incorporated. This is done by formulating the partition function as a path integral. Since the density operator $\hat{\rho} \equiv e^{-\beta\hat{\mathcal{H}}}$ looks like a time evolution operator in imaginary time $\tau = -\mathrm{i}\,t$ one identifies the inverse temperature β as an extra dimension, the imaginary time. Zero temperature corresponds to a full time dimension, whereas for $\beta \to 0$ the imaginary time dimension vanishes and the quantum mechanical system maps to a classical system where no quantum fluctuations occur.

In general time scaling differs from space scaling, so that one defines a dynamical critical exponent z [50, 51, 52]:

$$\tau_c \propto \xi^z \ , \tag{2.4}$$

where ξ is the correlation length in space and τ_c is a typical scale for the decay of the fluctuations in time. According to the universality hypothesis the scaling behavior is affected by the dimensionality. Therefore a d dimensional quantum system should correspond to a $d+z$ dimensional classical system. However, for many systems it holds: $z = 1$.

2.3 The Antiferromagnetic Phase

In an antiferromagnetically coupled system the spins favor anti-alignment, so that there is, in contrast to a ferromagnetically coupled system, no total magnetic moment in the absence of an external magnetic field. Thus, the obvious realization of the ground state seems to be that in which the spins are arranged alternately up and down. Clearly, for some lattice structures such as the triangular lattice in two dimensions or the pyrochlor lattice in three dimensions it is not possible to arrange all spins to be anti-aligned to their nearest neighbors. Those systems are called *geometrically frustrated* and shall not be discussed in this work. However, even for non-frustrated antiferromagnetic (AF) systems it is not trivial to find the ground state. Whereas in the Ising model the simple anti-aligned spin configuration $|\cdots\uparrow\downarrow\uparrow\downarrow\uparrow\downarrow\cdots\rangle$, known as Néel state, is clearly an eigenstate of the Hamiltonian, in the Heisenberg model described by the Hamiltonian of Eq. (1.4) such a configuration is not an eigenstate and thus not the ground state. To see this one has to consider the following term of the Heisenberg Hamiltonian:

$$\hat{\mathbf{S}}_{\mathbf{i}} \cdot \hat{\mathbf{S}}_{\mathbf{j}} = \hat{S}^z_{\mathbf{i}}\hat{S}^z_{\mathbf{j}} + \tfrac{1}{2}\left(\hat{S}^+_{\mathbf{i}}\hat{S}^-_{\mathbf{j}} + \hat{S}^-_{\mathbf{i}}\hat{S}^+_{\mathbf{j}}\right) \ . \tag{2.5}$$

While the $\hat{S}^z_{\mathbf{i}}\hat{S}^z_{\mathbf{j}}$-term of the Heisenberg Hamiltonian conserves the z-component of the spins, the $\hat{S}^\pm_{\mathbf{i}}\hat{S}^\mp_{\mathbf{j}}$-terms cause spin-flips. Therefore, when the Heisenberg Hamiltonian acts on a simple anti-aligned spin configuration (Néel state) this state changes and thus cannot be an eigenstate. Actually the determination of the ground state of the AF Heisenberg model is still an unsolved problem. Only for the one dimensional system with coupling between nearest neighbors has the exact ground state been found by Bethe [53]. It is also widely accepted that the one dimensional AF Heisenberg system does not exhibit magnetic long range order and thus no phase transition between an AF ordered and paramagnetic disordered phase can be observed.

Furthermore it was shown by Mermin and Wagner [54] that in an isotropic Heisenberg system with short-range interactions in one and two dimensions and for finite temperatures no ordered phase exists and thus no thermal phase transition between an ordered and disordered phase is expected. However, in a two dimensional system at zero temperature the ground state does show long-range order and at least a *quantum* phase transition can be observed for the dimensionality $d \geq 2$. To indicate the quantum phase transition an order parameter has to be introduced. One may define the staggered magnetization

$$M_s = \frac{1}{L^d} \Big\langle \sum_{\mathbf{i}} e^{\mathrm{i}\,\mathbf{Q}\cdot\mathbf{i}} \hat{S}^z_{\mathbf{i}} \Big\rangle \; , \tag{2.6}$$

which is finite in the antiferromagnetically ordered phase and zero in the disordered phase. Here, $\mathbf{Q} = (\pi, \ldots, \pi)$ is the AF wave vector and L the linear lattice size. $\hat{S}^z_{\mathbf{i}}$ denotes the z-component of the spin operator at site $\mathbf{i}$. However, the definition of the order parameter is not unique and it turns out that another quantity, called spin stiffness, which is easily obtained within quantum Monte Carlo simulations is also appropriate to indicate the quantum phase transition.

To intuitively understand the spin stiffness one can consider the free energy $\mathcal{F}$ given by

$$\mathcal{F} = -\frac{1}{\beta} \ln Z \; , \tag{2.7}$$

where β is the inverse temperature and Z stands for the partition function. To probe for long-ranged magnetic order one induces a continuous twist in spin space which, when cumulated along the length L along (e. g.) the x-axis, amounts to a twist of angle ϕ around a certain spin axis $\mathbf{e}$. This means that the boundary condition reads $\hat{\mathbf{S}}_{\mathbf{i}+L\mathbf{e}_x} = \mathsf{R}[\mathbf{e}, \phi]\hat{\mathbf{S}}_{\mathbf{i}}$ where $\mathsf{R}[\mathbf{e}, \phi]$ is a matrix describing an $SO(3)$ rotation around the axis $\mathbf{e}$ by the angle ϕ. In the disordered system the free energy should not be affected by the twist angle, whereas in the magnetically ordered system the free energy takes a minimum for $\phi = 0$. One obtains

$$\left.\frac{\partial^2 \mathcal{F}(\phi)}{\partial \phi^2}\right|_{\phi=0} = 0 \qquad \text{for the disordered system and}$$

$$\left.\frac{\partial^2 \mathcal{F}(\phi)}{\partial \phi^2}\right|_{\phi=0} > 0 \qquad \text{for the ordered system.}$$

Thus, the second derivative of the free energy is a quantity which indicates the degree of spin order. Following Eq. (2.7) this leads directly to the definition of the spin stiffness:

$$\rho_s = -\frac{1}{L^{d-2}} \frac{1}{\beta} \frac{\partial^2}{\partial \phi^2} \ln Z(\phi) \Big|_{\phi=0} \; , \tag{2.8}$$

where d is the dimensionality. In the presence of long-range order ρ_s takes a finite value and in the disordered phase it vanishes. In subsection 3.4.4 the implementation of the spin stiffness into the world line algorithm is explicitly shown.

2.4 The Haldane Phase

In this section attention is turned to one dimensional systems, especially the AF spin chains. As already mentioned in the previous section Bethe [53] proposed a solution for the ground state of the one dimensional AF Heisenberg system and determined its energy. Further studies by Lieb, Schultz and Mattis [55] and by Cloizeaux and Pearson [56] using the Bethe ansatz showed that the excitation spectrum of the spin-1/2 system is gapless where the lowest excited states are known to be triplet states [57] (for a review see Ref. [58]). In contrast, for the spin-1 chain it is widely accepted and extensively shown by numerical analyses [26, 27, 28, 29] that the excitation spectrum exhibits a gap. These results are summarized and generalized by Haldane [24] in his conjecture, which states that the excitations of an isotropic AF Heisenberg chain with half-integer spins are gapless, whereas for the integer spin chain there a gap exists. In the spirit of his assumption the gapped phase in the integer spin Heisenberg chain is nowadays known as the Haldane phase. In the following the discussion focuses on the Haldane phase of a spin-1 chain, for which Affleck *et al.* [59, 60] suggested a solution for the ground state, called valence-bond solid (VBS) state. More precisely, they presented the ground state of the bilinear-biquadratic Heisenberg Hamiltonian

$$\hat{\mathcal{H}} = \sum_i \left(\hat{\mathbf{S}}_i \cdot \hat{\mathbf{S}}_{i+1} - \beta (\hat{\mathbf{S}}_i \cdot \hat{\mathbf{S}}_{i+1})^2 \right) \tag{2.9}$$

for $\beta = \frac{1}{3}$. For $\beta = 1$ it is known from the Bethe ansatz that there is a unique ground state with no gap. On this basis Affleck *et al.* anticipate in Ref. [59] that the case $\beta = 1$ marks a critical point, below which the ungapped VBS phase – or equivalently the Haldane phase – occurs. Thus, for the case $\beta = 0$, which corresponds to the common Heisenberg model, one expects that the system is in the Haldane phase and the ground state is described by a VBS state. The VBS state is constructed in the following way: (i) Every spin-1 is decomposed into two spin-1/2 degrees of freedom. (ii) Between adjacent spin-1/2's of different sites singlet bonds are arranged as shown in Fig. 2.3. (iii) Finally, the spin-1/2's on each site have to be symmetrized to restore the spin-1 chain. Thus, the gap in the one dimensional AF spin-1 Heisenberg chain turns out to be the energy which is needed to break a singlet bond.

As a consequence it follows that if one goes along the chain and neglects all sites with magnetic quantum number $m = 0$ one finds a kind of Néel order with an alternating z-component of the total spin on each site. As den Nijs and Rommelse demonstrate in

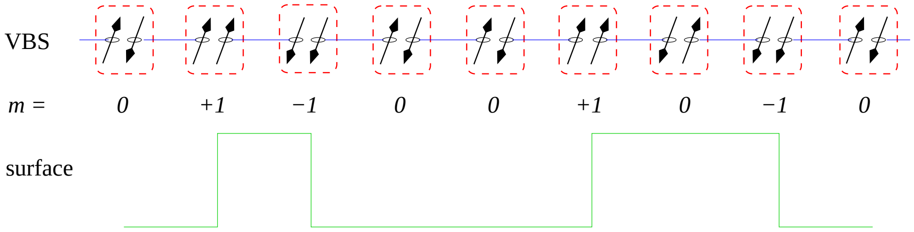

Figure 2.3: Valence-bond solid (VBS) state: Every spin-1 is decomposed into two spin-1/2 degrees of freedom. Pairs of adjacent spin-1/2 degrees of freedom form singlet bonds (blue lines). To restore the characteristics of a spin-1 chain the spin pairs on each site (red boxes) have to be symmetrized. The magnetic quantum number m denotes the z-component of the spin-1 on each site. The VBS state corresponds to the disordered flat phase (green contour) which is known from statistical mechanics of surface roughening transitions [62] and can be understood as a kind of hidden Néel order.

Ref. [61] this *hidden* AF order corresponds to the disordered flat (DOF) phase which is known from statistical mechanics of surface roughening transitions [62]. If one attributes every site with $m = +1$ to an upward step in a one dimensional contour along the chain and every site with $m = -1$ to a downward step, then the resulting structure is nearly *flat*. There are no two or more upward steps after another. Every elevated plateau is followed by a downward step [see Fig. 2.3]. Following this analogy den Nijs *et al.* defined an order parameter for the Haldane phase, which is called string order parameter and in the framework of the spin degrees of freedom reads

$$\mathcal{O}_s = \lim_{n\to\infty} \left\langle \hat{S}^z_{n_0} \exp\left(\mathrm{i}\,\pi \sum_{i=n_0}^{n_0+n} \hat{S}^z_i \right) \hat{S}^z_{n_0+n} \right\rangle . \tag{2.10}$$

$\mathcal{O}_s$ is finite in the Haldane phase. $\hat{S}^z_i$ is the z-component of the spin operator that measures the magnetic quantum number m. One has to note that there is a particular state where every site with $m = +1$ is followed by a site with $m = -1$. This *true* Néel state corresponds to a battlement structure in the framework of surface roughening physics which is named body-centered solid on solid (BCSOS) flat phase and which cannot be distinguished from the *hidden* AF order by the order parameter given in Eq. (2.10). Nevertheless the BCSOS flat phase differs essentially from the DOF phase. It has long-range order and exhibits no gap. Although such a phase is not expected in the one dimensional AF Heisenberg chain, other quasi one dimensional systems could exhibit a kind of Néel order. Therefore another order parameter should be introduced to distinguished between the hidden AF order and the Néel order [61]:

$$\mathcal{O}_H = \lim_{n\to\infty} \left\langle \exp\left(\mathrm{i}\,\pi \sum_{j=n_0}^{n_0+n} \hat{S}^z_j \right) \right\rangle . \tag{2.11}$$

	ground state	$\mathcal{O}_s$	$\mathcal{O}_H$	gap	analogon
Haldane phase	VBS state	$\neq 0$	$= 0$	yes	DOF
Néel phase	Néel state	$\neq 0$	$\neq 0$	no	BCSOS flat

Table 2.1: Characteristics of the Néel phase and the Haldane phase and their analogon in the physics of surface roughening transitions.

This string order parameter is finite in the BCSOS flat phase corresponding to the spin-1 Néel order and zero in the DOF phase which corresponds to the VBS phase with hidden AF order. A summary of the characteristics of the two different phases and their analogon in terms of surface roughening physics is given in Tab. 2.1.

Quantum Monte Carlo 3

Monte Carlo (MC) simulations are relevant in many scientific, but also non-scientific fields, where analytic approaches are not practicable. For example, it is used in mathematics to solve high dimensional integrals. Furthermore, MC methods are applied in the financial engineering and insurance industry for the estimate of risks, in meteorology for weather forecasting or in chemistry for molecular modeling. Moreover, MC simulation is one of the most and powerful numerical methods applied in strongly correlated electron systems. Although the fields of applications still flourish, the origins of MC simulations are traced back to the 18th century when the French scientist G.-L. Leclerc, Compte de Buffon (1707-1788), estimated the value of π using his famous needles experiment [63]. In modern physics the MC methods were introduced by J. von Neumann and S. Ulam during the Manhattan project in the 1940s. Neumann and Ulam solved integrals by means of random numbers and coined the name *Monte Carlo* for such random experiments. Since then a lot of progress, in particular in the development of improved sampling techniques, has been made. Nowadays, by applying cluster algorithms the efficiency is dramatically enhanced and with the use of supercomputers complex quantum many body systems can be simulated. However, the development of new algorithms, which for instance avoid the so-called *minus sign problem* [64] in quantum Monte Carlo methods, is still an ongoing challenge. By the term *quantum* Monte Carlo (QMC) various MC methods are summarized which are applied to quantum systems, for instance auxiliary field QMC [65, 66] or the recently developed Gaussian QMC [67, 68]. In this work the path integral QMC method is used. Here the d dimensional quantum system can be mapped to an $d+1$ dimensional classical system and the calculation of the observables corresponds to that known from classical MC methods in statistical mechanics.

In classical statistical mechanics the properties of a macroscopic many particle system can be derived from the microscopic properties of each single particle. The macroscopic observables are usually distributed around a mean value due to thermal fluctuations of the microscopic properties. Thus, the expectation value of an observable can be computed by averaging over the whole configuration space, in which every configuration x occurs with a certain weight determined by the Boltzmann factor $e^{-\beta E(x)}$, where β is the inverse temperature and $E(x)$ gives the total energy of configuration x. In statistical quantum mechanics the phase space is given by the Hilbert space of the total system. Each state of the Hilbert space occurs with a certain probability, summarized in the so-called density matrix ρ.

Because the configuration space usually increases exponentially with increasing system size, averaging over the whole configuration space very soon becomes impossible. The quantum Monte Carlo method, as well as the classical Monte Carlo method, can therefore be a tool to estimate the mean value of an observable without averaging over the whole configuration space. In a series of random experiments only the most likely and important configurations are considered (importance sampling).

In this chapter the path integral QMC method based on a world line description in discrete time is introduced. For the updating the very efficient loop algorithm is applied.

3.1 Path Integral Formulation and World Lines

Static properties in thermal equilibrium can be deduced from the thermal density operator $\hat{\rho} = e^{-\beta\hat{\mathcal{H}}}$, where $\hat{\mathcal{H}}$ is the Hamiltonian of the system. An observable can then be computed by

$$\langle\hat{\mathcal{O}}\rangle = Z^{-1}\,\mathrm{Tr}\,\rho\,\hat{\mathcal{O}}\ . \tag{3.1}$$

Z stands for the partition function

$$Z = \mathrm{Tr}\,\rho = \sum_\lambda \langle\lambda|e^{-\beta\hat{\mathcal{H}}}|\lambda\rangle\ , \tag{3.2}$$

where $\{|\lambda\rangle\}$ is an arbitrary orthonormal basis of the Hilbert space. If one associates β with some sort of imaginary time, then the thermal density operator looks like the propagation operator in imaginary time. Hence, the partition function can be interpreted as a path integral in imaginary time:

$$Z = \lim_{\Delta\tau\to 0}\int\left(\prod_{i=1}^{\beta/\Delta\tau}\mathrm{d}\lambda_i\right)\langle\lambda_1|e^{-\Delta\tau\hat{\mathcal{H}}}|\lambda_N\rangle\ldots\langle\lambda_2|e^{-\Delta\tau\hat{\mathcal{H}}}|\lambda_1\rangle\ . \tag{3.3}$$

The imaginary time axis can be understood as an additional dimension. The variations of the path along this extra dimension reflect the quantum fluctuations. The paths in imaginary time are called world lines.

In the following the discussion is focused on the one dimensional Heisenberg model as a simple example for the application of the path integral QMC method. The Hamiltonian is given by

$$\hat{\mathcal{H}} = J\sum_i \hat{\mathbf{S}}_i\cdot\hat{\mathbf{S}}_{i+1}\ . \tag{3.4}$$

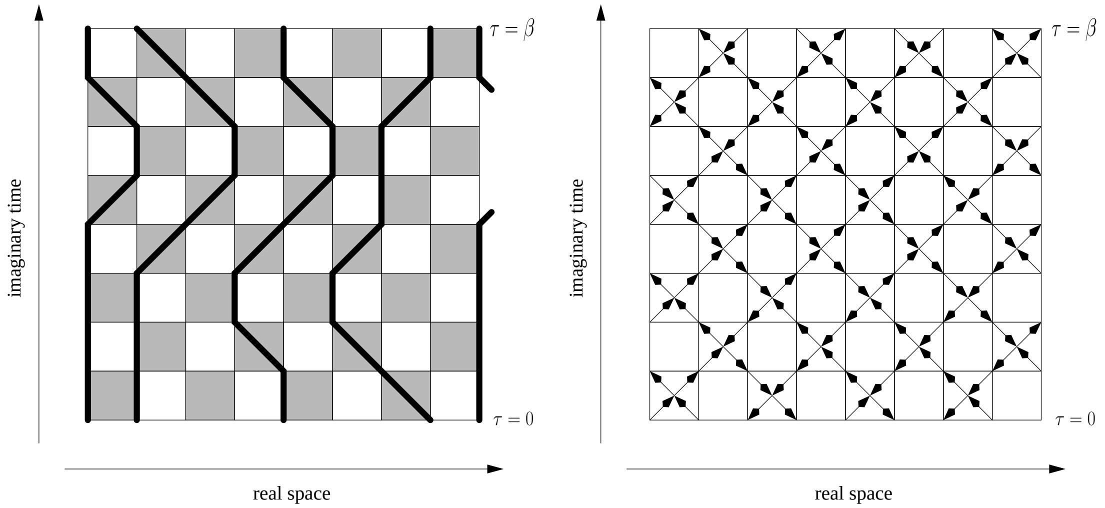

(a) World line representation

(b) Six vertex representation

Figure 3.1: (a) World line configuration: The bold lines represent the time evolution of the up-spins, the empty sites correspond to the down-spins. Periodic boundary conditions in space and imaginary time are considered. (b) Mapping to the six vertex representation of a world line configuration. According to Eq. (3.15) every plaquette in Fig. 3.1(a) corresponds to a vertex.

where the $\hat{\mathbf{S}}_i$'s are spin operators which satisfy commutation rules: $\left[\hat{S}_i^\alpha, \hat{S}_j^\beta\right] = \mathrm{i}\,\delta_{ij}\epsilon_{\alpha\beta\gamma}\hat{S}_i^\gamma$, where $\epsilon_{\alpha\beta\gamma}$ is the total antisymmetric Levi-Civita tensor. Furthermore, periodic boundary conditions are imposed: $\hat{\mathbf{S}}_{i+L} = \hat{\mathbf{S}}_i$. The basic concept of the world line algorithm is to split the Hamiltonian into sums of independent two site problems:

$$\hat{\mathcal{H}} \equiv \hat{\mathcal{H}}_1 + \hat{\mathcal{H}}_2 = \sum_i \hat{\mathcal{H}}^{(2i-1)} + \sum_i \hat{\mathcal{H}}^{(2i)} \ , \tag{3.5}$$

where each $\hat{\mathcal{H}}^{(i)}$ describes a two site interaction:

$$\hat{\mathcal{H}}^{(i)} = J\hat{\mathbf{S}}_i \cdot \hat{\mathbf{S}}_{i+1} = J\left(\hat{S}_i^z\hat{S}_{i+1}^z + \tfrac{1}{2}\left(\hat{S}_i^+\hat{S}_{i+1}^- + \hat{S}_i^-\hat{S}_{i+1}^+\right)\right) \ . \tag{3.6}$$

By using a Trotter decomposition [69] the path integral is divided into m small propagations generated in two steps by $\hat{\mathcal{H}}_1$ and $\hat{\mathcal{H}}_2$. Thus, the partition function of Eq. (3.3) reads

$$Z = \lim_{\Delta\tau\to 0} \sum_{\boldsymbol{\sigma}_1,\dots,\boldsymbol{\sigma}_{2m}} \langle\boldsymbol{\sigma}_1|e^{-\Delta\tau\hat{\mathcal{H}}_2}|\boldsymbol{\sigma}_{2m}\rangle\langle\boldsymbol{\sigma}_{2m}|e^{-\Delta\tau\hat{\mathcal{H}}_1}|\boldsymbol{\sigma}_{2m-1}\rangle \dots \langle\boldsymbol{\sigma}_2|e^{-\Delta\tau\hat{\mathcal{H}}_1}|\boldsymbol{\sigma}_1\rangle \ , \tag{3.7}$$

where $m\Delta\tau = \beta$. Each sum over $\boldsymbol{\sigma}_\tau$ runs over a complete basis of the tensor product Hilbert space spanned by the states

$$|\boldsymbol{\sigma}_\tau\rangle = \bigotimes_{i=1}^{L} |\sigma(\tau)\rangle_i \equiv |\sigma_1(\tau)\dots\sigma_L(\tau)\rangle \ , \tag{3.8}$$

where $|\sigma(\tau)\rangle_i \in \{\,|\uparrow\rangle, |\downarrow\rangle\}$ is a single site state at site i. Because $\hat{\mathcal{H}}_1$ and $\hat{\mathcal{H}}_2$ do not commute: $\left[\hat{\mathcal{H}}_1, \hat{\mathcal{H}}_2\right] \neq 0$, in the case of finite time steps an error of order $O(\Delta\tau^2)$ occurs. Fig. 3.1(a) depicts a graphical representation of the path integral of Eq. (3.7) for the one dimensional Heisenberg model. At $\tau = 0$ the system starts with configuration $\boldsymbol{\sigma}_1$ and ends up with configuration $\boldsymbol{\sigma}_1$ again at $\tau = \beta$. During this time interval the system is allowed to fluctuate. Every bold line in Fig. 3.1(a) represents the world line of a single up-spin [39, 40].

The partition function Z now writes

$$Z = \sum_w \Omega_w \quad \text{with} \quad \Omega_w = \prod_{t=1}^{m} \langle \boldsymbol{\sigma}_{2t+1}|e^{-\Delta\tau\hat{\mathcal{H}}_2}|\boldsymbol{\sigma}_{2t}\rangle\langle\boldsymbol{\sigma}_{2t}|e^{-\Delta\tau\hat{\mathcal{H}}_1}|\boldsymbol{\sigma}_{2t-1}\rangle \ , \tag{3.9}$$

where the sum runs over all possible world line configurations. Ω_w denotes the statistical weight of each world line configuration. Note, periodic boundary conditions are used: $\boldsymbol{\sigma}_{2m+1} = \boldsymbol{\sigma}_1$. The expectation value of an observables can be computed via

$$\langle\hat{\mathcal{O}}\rangle = \frac{\sum_w \Omega_w \mathcal{O}_w}{\sum_w \Omega_w} \ , \tag{3.10}$$

where $\mathcal{O}_w$ denotes the observable for world line configuration w. Because the Hamiltonians $\hat{\mathcal{H}}_i$ with $i = 1, 2$ consist of independent two site interactions each matrix element $\langle\boldsymbol{\sigma}_{\tau+1}|e^{-\Delta\tau\hat{\mathcal{H}}_i}|\boldsymbol{\sigma}_\tau\rangle$ of Eq. (3.9) can be decomposed into products:

$$\begin{aligned}
\langle\boldsymbol{\sigma}_{\tau+1}|e^{-\Delta\tau\hat{\mathcal{H}}_1}|\boldsymbol{\sigma}_\tau\rangle &= \prod_{i=1}^{L/2}\langle\sigma_{2i-1}(\tau+1)\sigma_{2i}(\tau+1)|e^{-\Delta\tau\hat{\mathcal{H}}^{(2i-1)}}|\sigma_{2i-1}(\tau)\sigma_{2i}(\tau)\rangle \ , \\
\langle\boldsymbol{\sigma}_{\tau+1}|e^{-\Delta\tau\hat{\mathcal{H}}_2}|\boldsymbol{\sigma}_\tau\rangle &= \prod_{i=1}^{L/2}\langle\sigma_{2i}(\tau+1)\sigma_{2i+1}(\tau+1)|e^{-\Delta\tau\hat{\mathcal{H}}^{(2i)}}|\sigma_{2i}(\tau)\sigma_{2i+1}(\tau)\rangle \ .
\end{aligned} \tag{3.11}$$

with $\sigma_{L+1} = \sigma_1$ and $|\sigma_i(\tau)\sigma_j(\tau)\rangle \equiv |\sigma(\tau)\rangle_i \otimes |\sigma(\tau)\rangle_j$. Every matrix element corresponds to the weight of a single plaquette shown in Fig. 3.1. Each plaquette describes a two site interaction between neighboring sites. There are six possible spin configurations on a plaquette which respect spin conservation. The matrix elements for each possible spin configuration can be easily computed and are given by

$$\begin{aligned}
&\left.\begin{array}{l}
W(\text{◧}) = \langle\uparrow\downarrow|e^{-\Delta\tau\hat{\mathcal{H}}^{(i)}}|\uparrow\downarrow\rangle = e^{\Delta\tau J/2}\cosh(\Delta\tau J/2) \\
W(\text{◨}) = \langle\downarrow\uparrow|e^{-\Delta\tau\hat{\mathcal{H}}^{(i)}}|\downarrow\uparrow\rangle = e^{\Delta\tau J/2}\cosh(\Delta\tau J/2)
\end{array}\right\} \equiv W(\pm 1) \\
&\left.\begin{array}{l}
W(\text{⧄}) = \langle\uparrow\downarrow|e^{-\Delta\tau\hat{\mathcal{H}}^{(i)}}|\downarrow\uparrow\rangle = -e^{\Delta\tau J/2}\sinh(\Delta\tau J/2) \\
W(\text{⧅}) = \langle\downarrow\uparrow|e^{-\Delta\tau\hat{\mathcal{H}}^{(i)}}|\uparrow\downarrow\rangle = -e^{\Delta\tau J/2}\sinh(\Delta\tau J/2)
\end{array}\right\} \equiv W(\pm 2) \\
&\left.\begin{array}{l}
W(\text{▥}) = \langle\uparrow\uparrow|e^{-\Delta\tau\hat{\mathcal{H}}^{(i)}}|\downarrow\downarrow\rangle = e^{-\Delta\tau J/4} \\
W(\text{□}) = \langle\downarrow\downarrow|e^{-\Delta\tau\hat{\mathcal{H}}^{(i)}}|\uparrow\uparrow\rangle = e^{-\Delta\tau J/4}
\end{array}\right\} \equiv W(\pm 3) \ .
\end{aligned} \tag{3.12}$$

	FM $(J < 0)$	AF $(J > 0)$
$W(\pm 1)$	$e^{-\Delta\tau\lvert J\rvert/4}\cosh(\Delta\tau\lvert J\rvert/2)$	$e^{\Delta\tau J/4}\cosh(\Delta\tau J/2)$
$W(\pm 2)$	$e^{-\Delta\tau\lvert J\rvert/4}\sinh(\Delta\tau\lvert J\rvert/2)$	$e^{\Delta\tau J/4}\sinh(\Delta\tau J/2)$
$W(\pm 2)$	$e^{\Delta\tau\lvert J\rvert/4}$	$e^{-\Delta\tau J/4}$

Table 3.1: Weights $W(s)$ for different plaquettes s for the ferromagnetic (FM) and antiferromagnetic (AF) case in a non-frustrated spin system. The straight forward calculation leads to negative weights in the AF system for $s = \pm 2$ [see Eq. (3.12)], thus a canonical transformation is applied to preserve exclusively positive weights.

One can identify each matrix element with a weight $W(s)$ of a spin configuration s on a plaquette. One should note that the weights of the spin-flip processes ($s = \pm 2$) come with a minus sign for $J > 0$. Since in non-frustrated lattices each world line configuration has an even number of spin-flip processes, the overall weight for a world line configuration remains positive. In other words for $J > 0$ one can apply a canonical transformation to yield exclusively positive weights on a plaquette. In Tab. 3.1 the weights $W(s)$ of the different spin configurations s on a plaquette for the antiferromagnetic case ($J > 0$) and ferromagnetic ($J < 0$) case in a non-frustrated spin system are listed.

3.2 Monte Carlo Sampling

The objective is to calculate the expectation values of physical observables in a quantum system, e. g. described by the one dimensional Heisenberg model defined in Eq. (3.4). Since the configuration space grows exponentially with system size, averaging over the whole configuration space becomes impossible for larger system sizes. In this case a Monte Carlo simulation provides an efficient tool to estimate the expectation value without averaging over the whole configuration space. In the previous section it is shown how to calculate the statistical weight Ω_w for each world line configuration w in the one dimensional Heisenberg model. Each world line corresponds to a trajectory in the configuration space. The Monte Carlo simulation produces a random walk through the configuration space selecting configurations depending on their statistical weight. Since the world line representation maps the d dimensional quantum system onto a $d+1$ dimensional classical system classical Monte Carlo still can be used, but with higher dimensionality because quantum fluctuations have to be included. Such a random walk through the configuration space is called a *Markov process*. For the Markov process two conditions have to be satisfied:

(i) Stationarity

The probability distribution $W(s)$ of a configuration s does not change during the Markov process. If $P[s \to s']$ is the probability of going from configuration s to configuration s', then one has to demand

$$\sum_s P\left[s \to s'\right] W(s) = W(s') \ . \tag{3.13}$$

There exists a tougher condition, where stationarity is automatically satisfied. It is called *detailed balance* and it reads

$$P\left[s \to s'\right] W(s) = P\left[s' \to s\right] W(s') \ . \tag{3.14}$$

(ii) Ergodicity

Within a finite number of steps every configuration s can be reached from an arbitrary configuration with finite probability.

Each interaction on a plaquette is described by a local Hamilton operator, thus detailed balance and ergodicity can be satisfied locally on individual plaquettes. This allows to create global updates with local stochastic decisions [39].

The task is now to find an updating scheme which provides an adequate path through the configuration space. For this the world line representation is mapped onto a six vertex model. Each plaquette corresponds to a vertex:

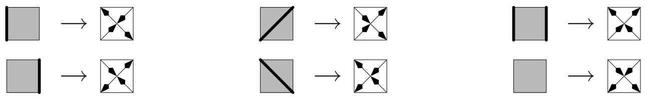

(3.15)

A world line configuration in terms of vertices is shown in Fig. 3.1(b). A new configuration can be produced as follows: One starts at a randomly chosen vertex and follows one of the outgoing arrows to the next vertex. At the next vertex there are two possibilities to continue the path. One chooses, in an appropriate way to be discussed later, one of these possibilities and pursues the path until one arrives at the initial vertex again. Such closed paths are called *loops*. A new configuration is then given by flipping all the arrows along the loop.

The different possibilities for a move on a plaquette are described by graphs: graph 1 stands for a vertical move ()(), graph 2 for a horizontal move (≍) and graph 3 describes a diagonal move (⤫). In Tab. 3.2 all possible graphs for a given vertex are listed. By introducing the graphs the space of vertices is expanded to a space of vertices and graphs. If $W(s)$ is the statistical weight of a vertex, the following identity for the weight $W(g|s)$ of the graph g by a given vertex s holds:

$$\sum_g W(g|s) = W(s) \ . \tag{3.16}$$

			possible graphs
$(s=\pm 1)$	/	:	$)($ $\vee$ $\asymp$
$(s=\pm 2)$	/	:	$\asymp$ $\vee$ $\times$
$(s=\pm 3)$	/	:	$)($ $\vee$ $\times$

Table 3.2: Possible graphs g for a given vertex s. If a graph is related to a vertex, its weight $V(g)$ is independent of the associated vertex. If a graph is not related to a vertex the weight is $V(g) = 0$ [see Eq. (3.17)].

In order to achieve a constant acceptance rate one proposes the following rule for choosing a graph which fulfils ergodicity:

$$\begin{aligned} W(g|s) &= V(g) \qquad &\text{for} \qquad & W(g|s) \neq 0 \\ W(g|s) &= 0 \qquad &\text{for} \qquad & W(g|s) = 0 \ . \end{aligned} \tag{3.17}$$

This implies, that the weights of graphs are independent of a given vertex s for all $W(g|s) \neq 0$. The probability of flipping the spins on a plaquette according to the graph g is then, for example, given by the Metropolis algorithm:

$$P\left[(g,s) \to (g,s')\right] = \min\left[1, \frac{W(g|s')}{W(g|s)}\right] = 1 \ . \tag{3.18}$$

Detailed balance in the space of vertices and graphs is trivially satisfied:

$$W(g|s) P\left[(g,s) \to (g,s')\right] = W(g|s') P\left[(g,s') \to (g,s)\right] \ . \tag{3.19}$$

Now the space of vertices and graphs is again reduced to the space of vertices. The actual transition probability $P\left[s \to s'\right]$ from one vertex to the other is given by

$$P\left[s \to s'\right] = \sum_g \frac{W(g|s)}{W(s)} P\left[(g,s) \to (g,s')\right] \ . \tag{3.20}$$

By combining Eq. (3.19) and Eq. (3.20) detailed balance in the space of vertices can also be seen very easily:

$$W(s) P\left[s \to s'\right] = W(s') P\left[s' \to s\right] \ . \tag{3.21}$$

Thus, the rule for choosing a graph proposed in Eq. (3.17) fulfils both ergodicity and stationarity. According to Eq. (3.16) and Eq. (3.17) the weights of graphs $V(g)$ are determined by the following equations:

$$W(\pm 1) = V(\,)(\,) + V(\,\asymp\,) \tag{3.22}$$

$$W(\pm 2) = V(\,\asymp\,) + V(\,\times\,) \tag{3.23}$$

$$W(\pm 3) = V(\,)(\,) + V(\,\times\,) \ . \tag{3.24}$$

The weights of the vertices $W(s)$ are taken from Tab. 3.1. The resulting probabilities $P(g) \equiv V(g)/\sum_g V(g)$ of the graphs are summarized in Tab. 3.3. Now, if the probability of a graph for a given vertex is known, one can allot a graph to a vertex by stochastic decisions. The so chosen graph decides the path of the loop, where the spins have to be flipped.

	AF $(J > 0)$	FM $(J < 0)$
$P($)($)$	$2/\left(1+\exp(\Delta\tau J)\right)$	$e^{-\Delta\tau\lvert J\rvert/2}\cosh(\Delta\tau\lvert J\rvert/2)$
$P($ ≍ $)$	$\tanh(\Delta\tau J/2)$	0
$P($ ⤫ $)$	0	$e^{-\Delta\tau\lvert J\rvert/2}\sinh(\Delta\tau\lvert J\rvert/2)$

Table 3.3: The probabilities for choosing an allowed graph for antiferromagnetic (AF) and ferromagnetic (FM) couplings. The allowed graphs for a given vertex are listed in Tab. 3.2.

3.3 Implementation of Single Hole Dynamics

In the following it is shown how to implement the dynamics of a single doped hole within the magnetic environment of the Heisenberg model into the world line algorithm. To incorporate the dynamics and to allow hopping the Heisenberg model has to be extended. This can be done within the framework of the t-J model [11]:

$$\hat{\mathcal{H}}_{tJ} = \hat{P}_S\left[-t\sum_{\langle ij\rangle}\sum_{\sigma}\left(\hat{c}^{\dagger}_{i,\sigma}\hat{c}_{j,\sigma}+\mathrm{H.\,c.}\right)+J\sum_{\langle ij\rangle}\left(\hat{\mathbf{S}}_i\cdot\hat{\mathbf{S}}_j-\tfrac{1}{4}\hat{n}_i\hat{n}_j\right)\right]\hat{P}_S\ . \tag{3.25}$$

The sums run over all nearest neighbors. σ stands for the spin degree of freedom. $\hat{c}^{\dagger}_{i,\sigma}$ creates a fermionic particle with spin σ at site i: $\left\{\hat{c}_{i,\sigma},\hat{c}^{\dagger}_{j,\sigma'}\right\}=\delta_{ij}\delta_{\sigma\sigma'}$. $\hat{n}_i=\sum_\sigma\hat{c}^{\dagger}_{i,\sigma}\hat{c}_{i,\sigma}$ is the occupation number operator. The operator $\hat{P}=\prod_i\left(\mathbb{1}-\hat{n}_{i,\uparrow}\hat{n}_{i,\downarrow}\right)$ with $\hat{n}_{i,\sigma}=\hat{c}^{\dagger}_{i,\sigma}\hat{c}_{i,\sigma}$ projects onto the subspace S with only unoccupied or single occupied states:

$$S=\left\{\,|\varsigma\rangle=\bigotimes_i|\varsigma\rangle_i\;\middle|\;\langle\varsigma|\sum_\sigma\hat{n}_{i,\sigma}|\varsigma\rangle\le 1\ \forall i\,\right\}\ . \tag{3.26}$$

Here, $|\varsigma\rangle_i\in\{|\,0\,\rangle,|\uparrow\rangle,|\downarrow\rangle,|\uparrow\downarrow\rangle\}$ is a single site state. In the case of half filling the hopping term in Eq. (3.25) vanishes and one can easily see that the t-J model maps to the Heisenberg model of Eq. (3.4) up to constant.

To implement the single hole dynamics into the world line formulation a canonical transformation, introduced by A. Angelucci [70], has to be applied. This transformation separates the spin degree of freedom and the occupation number:

$$\begin{array}{lclclcl}
|\uparrow\rangle & \rightarrow & |1,\Uparrow\rangle & \qquad & \hat{c}_{i,\uparrow} & \rightarrow & \hat{\sigma}^{z,+}_i\hat{f}^{\dagger}_i-\hat{\sigma}^{z,-}_i\hat{f}_i\\
|\downarrow\rangle & \rightarrow & |1,\Downarrow\rangle & & \hat{c}^{\dagger}_{i,\uparrow} & \rightarrow & \hat{\sigma}^{z,+}_i\hat{f}_i-\hat{\sigma}^{z,-}_i\hat{f}^{\dagger}_i\\
|\,0\,\rangle & \rightarrow & |0,\Uparrow\rangle & & \hat{c}_{i,\downarrow} & \rightarrow & \left(\hat{f}_i+\hat{f}^{\dagger}_i\right)\hat{\sigma}^{+}_i\\
|\uparrow\downarrow\rangle & \rightarrow & |0,\Downarrow\rangle & & \hat{c}^{\dagger}_{i,\downarrow} & \rightarrow & \hat{\sigma}^{-}_i\left(\hat{f}^{\dagger}_i+\hat{f}_i\right)\ .
\end{array} \tag{3.27}$$

$\hat{f}^{\dagger}_i$ and $\hat{f}_i$ are spinless fermion operators which act on the charge degree of freedom and create (annihilate) a hole at site i: $\hat{f}^{\dagger}_i|1,\sigma\rangle=|0,\sigma\rangle$, $\hat{\sigma}^{\pm}_i$ are ladder operators for the spin degree of freedom and $\hat{\sigma}_i^{z,\pm} = \frac{1}{2}\left(\hat{\mathbb{1}} \pm \hat{\sigma}_i^z\right)$ are projection operators acting on the spin degree of freedom. Within this basis the Hamiltonian of the t-J model writes

$$\hat{\mathcal{H}}_{tJ} = \hat{\mathcal{P}}_S \left[t \sum_{\langle ij \rangle} \left(\hat{f}_j^\dagger \hat{f}_i \hat{P}_{ij} + \text{H.c.} \right) + \frac{J}{2} \sum_{\langle ij \rangle} \left(\hat{P}_{ij} - \hat{\mathbb{1}} \right) \hat{\Delta}_{ij} \right] \hat{\mathcal{P}}_S \tag{3.28}$$

with $\hat{P}_{ij} = \frac{1}{2}\left(\hat{\boldsymbol{\sigma}}_i \cdot \hat{\boldsymbol{\sigma}}_j + \hat{\mathbb{1}}\right)$ where $\hat{\boldsymbol{\sigma}} = (\hat{\sigma}^x, \hat{\sigma}^y, \hat{\sigma}^z)^\mathsf{T} \equiv 2\hat{\mathbf{S}}$ is related to the spin operator $\hat{\mathbf{S}}$ and $\hat{\Delta}_{ij} = \hat{\mathbb{1}} - \hat{f}_i^\dagger \hat{f}_i - \hat{f}_j^\dagger \hat{f}_j$. $\hat{\mathcal{P}}_S = \prod_i \left(\hat{\mathbb{1}} - \hat{f}_i^\dagger \hat{f}_i \hat{\sigma}_i^+ \hat{\sigma}_i^- \right)$ is a projection operator in Angelucci representation which projects onto the subspace S. This representation has two important advantages which facilitate the numerical simulations:

(i) Because the Hamiltonian commutes with the projection operator, $\left[\hat{\mathcal{H}}_{tJ}, \hat{\mathcal{P}}_S\right] = 0$, the bare Hamiltonian ($\hat{\mathcal{H}}_{tJ}$ without projections) generates only states of subspace S provided that the initial state is in the relevant subspace.

(ii) The Hamiltonian is bilinear in the spinless fermion operators.

The dynamics of the doped hole are determined by the Green's function. Without loss of generality in the following the determination of the Green's function is restricted to the up-spin sector. Following Refs. [71, 72] one defines

$$\mathcal{G}(j-i, \tau) = \langle \mathcal{T} \hat{c}_{j,\uparrow}^\dagger(\tau) \hat{c}_{i,\uparrow}(0) \rangle \ . \tag{3.29}$$

Here, $\mathcal{T}$ induces time ordering. In the following $\tau \geq 0$ is assumed. The Green's function can also be reformulated in the basis of Eq. (3.27). Within the Angelucci representation it writes

$$\mathcal{G}(j-i, \tau) = \frac{1}{Z} \operatorname{Tr} \left[e^{-(\beta-\tau)\hat{\mathcal{H}}_{tJ}} \hat{\sigma}_j^{z,+} \hat{f}_j e^{-\tau \hat{\mathcal{H}}_{tJ}} \hat{\sigma}_i^{z,+} \hat{f}_i^\dagger \right] \ , \tag{3.30}$$

where $Z = \operatorname{Tr} e^{-\beta \hat{\mathcal{H}}_{tJ}}$ is the partition function. Here, the time evolution of the operators is explicitly introduced: $\hat{\mathcal{O}}(\tau) = e^{\tau \hat{\mathcal{H}}_{tJ}} \hat{\mathcal{O}} e^{-\tau \hat{\mathcal{H}}_{tJ}}$. To derive a world line formulation of the Green's function a complete set of basis states with no hole are introduced by

$$\hat{\mathbb{1}} = \sum_{\boldsymbol{\sigma}} |v, \boldsymbol{\sigma}\rangle\langle v, \boldsymbol{\sigma}| \quad \text{with} \quad |v, \boldsymbol{\sigma}\rangle = \bigotimes_{i=1}^{L} |1, \sigma\rangle_i \ , \tag{3.31}$$

where $|1, \sigma\rangle_i$ denotes a single site state in Angelucci representation. Analogically, one finds for the Hilbert space with a single doped hole

$$\hat{\mathbb{1}} = \sum_{h, \boldsymbol{\sigma}} |h, \boldsymbol{\sigma}\rangle\langle h, \boldsymbol{\sigma}| \quad \text{with} \quad |h, \boldsymbol{\sigma}\rangle = \hat{\sigma}_h^{z,+} \hat{f}_h^\dagger |v, \boldsymbol{\sigma}\rangle \ . \tag{3.32}$$

Next, the Hamiltonian $\hat{\mathcal{H}}_{tJ}$ is split into two sets of independent two site problems by a Trotter decomposition similar to the splitting of the Heisenberg Hamiltonian in section 3.1: $\hat{\mathcal{H}}_{tJ} = \hat{\mathcal{H}}_1 + \hat{\mathcal{H}}_2$. For the Green's function in Eq. (3.30) one obtains

$$\mathcal{G} = \frac{1}{Z} \sum_{\boldsymbol{\sigma}_1} \langle v, \boldsymbol{\sigma}_1 | \left(e^{-\Delta\tau \hat{\mathcal{H}}_2} e^{-\Delta\tau \hat{\mathcal{H}}_1} \right)^{m-n} \hat{\sigma}_j^{z,+} \hat{f}_j \left(e^{-\Delta\tau \hat{\mathcal{H}}_2} e^{-\Delta\tau \hat{\mathcal{H}}_1} \right)^{n} \hat{\sigma}_i^{z,+} \hat{f}_i^\dagger | v, \boldsymbol{\sigma}_1 \rangle \tag{3.33}$$

with $n\Delta\tau = \tau$ and $m\Delta\tau = \beta$. The systematic error of order $O(\Delta\tau^2)$ due to the discretization of the imaginary time is neglected. By inserting the unit operators of Eq. (3.31) and Eq. (3.32) at every time step one arrives at the Green's function in the following form:

$$\mathcal{G}(i-j,\tau) = \frac{\sum_w \Omega_w \mathcal{G}_w(i-j,\tau)}{\sum_w \Omega_w} \ , \tag{3.34}$$

where the sums run over all possible world line configurations with no hole. The weight Ω_w of a world line configuration w is given by

$$\Omega_w = \prod_{t=1}^{n} \langle v, \boldsymbol{\sigma}_{2t+1} | e^{-\Delta\tau\hat{\mathcal{H}}_2} | v, \boldsymbol{\sigma}_{2t}\rangle \langle v, \boldsymbol{\sigma}_{2t} | e^{-\Delta\tau\hat{\mathcal{H}}_1} | v, \boldsymbol{\sigma}_{2t-1}\rangle \ . \tag{3.35}$$

Note, that within the basis of configurations with no hole the t-J Hamiltonian maps to the Heisenberg Hamiltonian, and the weights correspond exactly to the weights of the world line configurations in the Heisenberg model. The Green's function for a given world line configuration is of the form

$$\begin{aligned} &\mathcal{G}_w(i-j,\tau) = \\ &= \sum_{h_2,\ldots,h_{2n}} \frac{\langle v, \boldsymbol{\sigma}_{2n+1} | \hat{\sigma}_j^{z,+} \hat{f}_j e^{-\Delta\tau\hat{\mathcal{H}}_2} | h_{2n}, \boldsymbol{\sigma}_{2n}\rangle \times \ldots \times \langle h_2, \boldsymbol{\sigma}_2 | e^{-\Delta\tau\hat{\mathcal{H}}_1} \hat{\sigma}_i^{z,+} \hat{f}_i^{\dagger} | v, \boldsymbol{\sigma}_1\rangle}{\langle v, \boldsymbol{\sigma}_{2n+1} | e^{-\Delta\tau\hat{\mathcal{H}}_2} | v, \boldsymbol{\sigma}_{2n}\rangle \times \ldots \times \langle v, \boldsymbol{\sigma}_2 | e^{-\Delta\tau\hat{\mathcal{H}}_1} | v, \boldsymbol{\sigma}_1\rangle} \ . \end{aligned} \tag{3.36}$$

This expression for the Green's function corresponds to a multiple matrix multiplication:

$$\mathcal{G}_w(i-j,\tau) = \left[\mathbf{A}_1(\boldsymbol{\sigma}_{2n+1}, \boldsymbol{\sigma}_{2n}) \times \mathbf{A}_2(\boldsymbol{\sigma}_{2n}, \boldsymbol{\sigma}_{2n-1}) \times \ldots \times \mathbf{A}_2(\boldsymbol{\sigma}_2, \boldsymbol{\sigma}_1)\right]_{ij} \ , \tag{3.37}$$

where the matrix element

$$\left[\mathbf{A}_\alpha(\boldsymbol{\sigma}_{\tau+1}, \boldsymbol{\sigma}_\tau)\right]_{ij} = \frac{\langle v, \boldsymbol{\sigma}_{\tau+1} | \hat{\sigma}_j^{z,+} \hat{f}_j e^{-\Delta\tau\hat{\mathcal{H}}_\alpha} \hat{\sigma}_i^{z,+} \hat{f}_i^{\dagger} | v, \boldsymbol{\sigma}_\tau\rangle}{\langle v, \boldsymbol{\sigma}_{\tau+1} | e^{-\Delta\tau\hat{\mathcal{H}}_\alpha} | v, \boldsymbol{\sigma}_\tau\rangle} \tag{3.38}$$

describes the weight of the hole to propagate from site i to site j within the time step $\Delta\tau$. It can be easily shown that the evaluation of the matrix elements reduces to the subspace of a two site problem, so that it only depends on the spin configuration (vertex s) of the plaquette, on which the hole propagation takes place:

$$\mathsf{A}_{lr}(s) = \frac{{}_l\langle v, \sigma_{\tau+1} | \otimes {}_r\langle v, \sigma_{\tau+1} | \hat{\sigma}_j^{z,+} \hat{f}_j e^{-\Delta\tau\hat{\mathcal{H}}^{(lr)}} \hat{\sigma}_i^{z,+} \hat{f}_i^{\dagger} | v, \sigma_\tau\rangle_l \otimes | v, \sigma_\tau\rangle_r}{{}_l\langle v, \sigma_{\tau+1} | \otimes {}_r\langle v, \sigma_{\tau+1} | e^{-\Delta\tau\hat{\mathcal{H}}^{(lr)}} | v, \sigma_\tau\rangle_l \otimes | v, \sigma_\tau\rangle_r} \ . \tag{3.39}$$

Here, $\hat{\mathcal{H}}^{(lr)}$ denotes the Hamiltonian of the two site interaction between site l and site r where the hole is supposed to propagate: $i, j \in \{l, r\}$. There are four possible processes for a given vertex s. The matrix elements $\mathsf{A}_{lr}(s)$ for these processes are listed in Tab. 3.4.

3.4 Implementation of Observables

In this section some observables and their implementation into the world line algorithm are introduced.

s	$l \rightarrow l$	$l \rightarrow r$	$r \rightarrow l$	$r \rightarrow r$
	$\frac{\cosh(-\Delta\tau t)}{e^{\Delta\tau J/2}\cosh(\Delta\tau J/2)}$	0	0	0
	0	0	0	$\frac{\cosh(-\Delta\tau t)}{e^{\Delta\tau J/2}\cosh(\Delta\tau J/2)}$
	0	0	$\frac{\sinh(-\Delta\tau t)}{-e^{\Delta\tau J/2}\sinh(\Delta\tau J/2)}$	0
	0	$\frac{\sinh(-\Delta\tau t)}{-e^{\Delta\tau J/2}\sinh(\Delta\tau J/2)}$	0	0
	$\cosh(-\Delta\tau t)$	$\sinh(-\Delta\tau t)$	$\sinh(-\Delta\tau t)$	$\cosh(-\Delta\tau t)$
	0	0	0	0

Table 3.4: Calculated matrix elements defined in Eq. (3.39), which represent the weight of the hole to propagate at a given plaquette, depending on the spin configuration or the corresponding vertex s. The plaquette is bordered by a left (l) and right (r) site. In this table the four possible moves within a time step $\Delta\tau$ are listed.

3.4.1 Energy

The total energy E of a system is given by the expectation value of the Hamilton operator, which for instance is given by Eq. (3.4). Using the Trotter decomposition ($\beta = m\Delta\tau$) and neglecting the quadratic error in $\Delta\tau$ one writes

$$\langle\hat{\mathcal{H}}\rangle = \frac{1}{Z}\,\mathrm{Tr}\left[\left(e^{-\Delta\tau\hat{\mathcal{H}}_2}e^{-\Delta\tau\hat{\mathcal{H}}_1}\right)^m\left(\hat{\mathcal{H}}_1+\hat{\mathcal{H}}_2\right)\right] , \tag{3.40}$$

where a splitting of the Hamiltonian analog to Eq. (3.5) is done. If one inserts the unity operator at each time steps, one obtains

$$\begin{aligned}\langle\hat{\mathcal{H}}\rangle \;=\; \frac{1}{Z}\sum_{\boldsymbol{\sigma}_1,\ldots,\boldsymbol{\sigma}_{2m}} & \left[\prod_{t=1}^{m}\langle\boldsymbol{\sigma}_{2t+1}|e^{-\Delta\tau\hat{\mathcal{H}}_2}|\boldsymbol{\sigma}_{2t}\rangle\langle\boldsymbol{\sigma}_{2t}|e^{-\Delta\tau\hat{\mathcal{H}}_1}|\boldsymbol{\sigma}_{2t-1}\rangle\right]\times \\ & \times\left[\frac{\langle\boldsymbol{\sigma}_3|e^{-\Delta\tau\hat{\mathcal{H}}_2}\hat{\mathcal{H}}_2|\boldsymbol{\sigma}_2\rangle}{\langle\boldsymbol{\sigma}_3|e^{-\Delta\tau\hat{\mathcal{H}}_2}|\boldsymbol{\sigma}_2\rangle}+\frac{\langle\boldsymbol{\sigma}_2|e^{-\Delta\tau\hat{\mathcal{H}}_1}\hat{\mathcal{H}}_1|\boldsymbol{\sigma}_1\rangle}{\langle\boldsymbol{\sigma}_2|e^{-\Delta\tau\hat{\mathcal{H}}_1}|\boldsymbol{\sigma}_1\rangle}\right] ,\end{aligned} \tag{3.41}$$

where the periodic boundary condition $\boldsymbol{\sigma}_{2m+1} = \boldsymbol{\sigma}_1$ has to be considered. This formula takes the form

$$\langle\hat{\mathcal{H}}\rangle = \frac{\sum_w \Omega_w E_w}{\sum_w \Omega_w} , \tag{3.42}$$

which is convenient for the Monte Carlo simulation. The weight Ω_w corresponds to the weight of a world line configuration given in Eq. (3.9). The energy E_w for a given world line configuration writes

$$E_w = -\frac{\partial}{\partial\Delta\tau}\left[\ln\langle\boldsymbol{\sigma}_3|e^{-\Delta\tau\hat{\mathcal{H}}_2}|\boldsymbol{\sigma}_2\rangle + \ln\langle\boldsymbol{\sigma}_2|e^{-\Delta\tau\hat{\mathcal{H}}_1}|\boldsymbol{\sigma}_1\rangle\right] . \tag{3.43}$$

			$\varepsilon(s)$
$(s=\pm 1)$	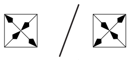	:	$-\frac{J}{4}\left(1+2\tanh\left(\frac{\Delta\tau J}{2}\right)\right)$
$(s=\pm 2)$	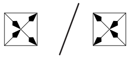	:	$-\frac{J}{4}\left(1+2\coth\left(\frac{\Delta\tau J}{2}\right)\right)$
$(s=\pm 3)$	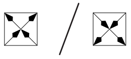	:	$J/4$

Table 3.5: Energy $\varepsilon(s)$ as defined in Eq. (3.44) for two site interactions on a plaquette. The energy depends on the spin configuration or equivalently the vertex s of the plaquette.

Thus, the energy is nothing but the logarithmic derivative of the weight of a single time slice with respect to $\Delta\tau$. Since the trace of Eq. (3.40) is invariant under cyclic permutation, the choice of the time slice is arbitrary. Therefore it is reasonable to average over all time slices to reduce fluctuations. According to Eq. (3.11) the weight of a time slice can be split into a product of weights of plaquettes. Thus, for the energy it holds

$$E_w = -\sum_{i=1}^{L} \frac{\partial}{\partial \Delta\tau} \langle \sigma_i(\tau+1)\sigma_{i+1}(\tau+1)| e^{-\Delta\tau \hat{\mathcal{H}}^{(i)}} |\sigma_i(\tau)\sigma_{i+1}(\tau)\rangle = \sum_{i=1}^{L} \varepsilon_i(s) \tag{3.44}$$

with periodic boundary condition $L+i=i$. It is obvious that the energy splits into a sum of energy fractions where each fraction stands for a two site interaction energy depending on the vertex s that corresponds to the plaquette between two neighboring sites. For the Heisenberg Hamiltonian the different energies for a plaquette depending on the vertex are listed in Tab. 3.5.

3.4.2 Spin Correlation Function

In the case of an $SU(2)$ symmetric model, for instance the Heisenberg model of Eq. (3.4), there is no difference between the longitudinal and the transversal correlation function. Since the world line approach is formulated in a basis of the z-components of the spins a natural definition of the spin correlation function is

$$S_{ij}(\tau) = \langle \hat{S}_i^z(\tau)\hat{S}_j^z(0)\rangle \ , \tag{3.45}$$

where $\hat{S}_i^z$ locally conserves the z-component of the spin: $\hat{S}_i^z|\boldsymbol{\sigma}_\tau\rangle = \sigma_i(\tau)|\boldsymbol{\sigma}_\tau\rangle$ with $|\boldsymbol{\sigma}_\tau\rangle$ as defined in Eq. (3.8). The spin correlation function is then given by

$$S_{ij}(\tau) = \frac{\sum_w \Omega_w \mathcal{S}_w(i-j,\tau)}{\sum_w \Omega_w} \quad \text{with} \quad \mathcal{S}_w(i-j,\tau) = \sigma_i(\tau)\sigma_j(0) \ , \tag{3.46}$$

where the sums run over all possible world line configurations and the weight Ω_w is given by Eq. (3.9). $\sigma_i(\tau) = \pm\frac{1}{2}$ denotes the z-component of the spin at site i and imaginary time τ.

3.4.3 String Order Parameters

The string order parameters $\mathcal{O}_s$ and $\mathcal{O}_H$ are non-local order parameters which are used to characterize phases in one dimensional systems. An illustration and the definitions of the string order parameters are given in section 2.4. Since the definitions of the string order parameters only contain $\hat{S}^z$-operators they can be computed in the same easy way as it is done for the spin correlation function. The expectation value is given by

$$\langle \hat{\mathcal{O}}_{s,H} \rangle = \frac{\sum_w \Omega_w \mathcal{O}_w}{\sum_w \Omega_w} \ , \tag{3.47}$$

where the sums run over all possible world line configurations and the weight of each world line configuration is given by Eq. (3.9). The observables of each world line configuration are given by

$$\langle \hat{\mathcal{O}}_s \rangle \quad : \quad \mathcal{O}_w = \sigma_{n_0} \left[\prod_{i=n_0}^{n_0+L/2} \exp\left(\mathrm{i}\,\pi \sigma_i\right) \right] \sigma_{n_0+L/2} \tag{3.48}$$

$$\langle \hat{\mathcal{O}}_H \rangle \quad : \quad \mathcal{O}_w = \prod_{i=n_0}^{n_0+L/2} \exp\left(\mathrm{i}\,\pi \sigma_i\right) \tag{3.49}$$

where $\sigma_i = \pm\frac{1}{2}$ denotes the z-component of the spin at site i. L stands for the lattice size and n_0 can be an arbitrary site. Since there is no preference for the time slice where the measurement is done, averaging over all time slices is reasonable to reduce fluctuations.

3.4.4 Spin Stiffness

The spin stiffness is a quantity which indicates the degree of spin order in a system. In section 2.3 a motivation of its definition is given:

$$\rho_s = -\frac{1}{L^{d-2}} \frac{1}{\beta} \frac{\partial^2}{\partial \phi^2} \ln Z(\phi) \bigg|_{\phi=0} \ , \tag{3.50}$$

where L is the linear system size and d is the dimensionality. β stands for the inverse temperature. The partition function $Z(\phi)$ depends on a twist angle ϕ [see section 2.3]. According to Eq. (3.9) the partition function is given by

$$Z(\phi) = \sum_w \left[\prod_p W(s_p, \phi) \right] \quad \text{with} \quad W(s_p, \phi) = \langle \boldsymbol{\sigma}_{\tau+1} | e^{-\Delta\tau \hat{\mathcal{H}}_p(\phi)} | \boldsymbol{\sigma}_\tau \rangle \ , \tag{3.51}$$

Here, $W(s_p, \phi)$ denotes the weight of a single plaquette p. Thus, the product over p runs over all plaquettes of a world line configuration. Each plaquette is related to a vertex s_p depending on the spin configuration on the plaquette. The interaction on a plaquette is determined by the two site Hamiltonian $\hat{\mathcal{H}}_p(\phi)$ which depends on the twist angle ϕ. By

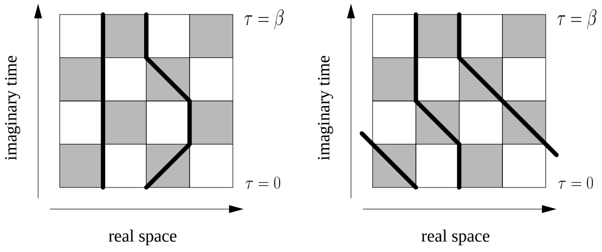

(a) No winding (b) With winding

Figure 3.2: (a) If the number of right and left going paths is equal, the world lines do not wind. (b) For an unequal number of left and right going paths winding occurs.

taking the derivatives in the definition (3.50) and regarding Eq. (3.51) one ends up with the following form:

$$\rho = \frac{\sum_w \Omega_w \rho_w}{\sum_w \Omega_w} \ , \tag{3.52}$$

where $\Omega_w = \prod_p W(s_p, \phi)$ denotes the weight of a world line configuration w. The spin stiffness of a certain world line configuration is determined by

$$\rho_w = -\frac{1}{L^{d-2}} \frac{1}{\beta} \left(\sum_p \frac{\frac{\partial}{\partial \phi} W(s_p, \phi)}{W(s_p, \phi)} \right)^2 \Bigg|_{\phi=0} \ . \tag{3.53}$$

For small time steps, as required in the world line approach, the exponential function in Eq. (3.51) can be expanded and the weights $W_p(s, \phi)$ can be approximated by

$$W(s_p, \phi) \simeq {}_l\langle \sigma_{\tau+1}| \otimes {}_r\langle \sigma_{\tau+1}| \left(\hat{\mathbb{1}} - \Delta\tau \hat{\mathcal{H}}_p(\phi) \right) |\sigma_\tau\rangle_l \otimes |\sigma_\tau\rangle_r \ , \tag{3.54}$$

where l and r denote the left and right hand sites of a plaquette p. Assuming a one dimensional Heisenberg system which is twisted along the $\mathbf{e}_z$-spin-axis, the spin operators are transformed by $\hat{\mathbf{S}} \to \hat{\mathbf{S}}' = \mathbf{R}[\mathbf{e}_z, \phi]\, \hat{\mathbf{S}}$ where $\mathbf{R}$ is a $SO(3)$ rotation matrix, and the twisted Hamiltonian of a two site interaction is given by

$$\hat{\mathcal{H}}_p(\phi) = J \left(\hat{S}_l^z \hat{S}_r^z + \frac{1}{2} \left(e^{\mathrm{i}\,\phi/L} \hat{S}_l^+ \hat{S}_r^- + e^{-\mathrm{i}\,\phi/L} \hat{S}_l^- \hat{S}_r^+ \right) \right) \ , \tag{3.55}$$

where $\hat{S}_i^\pm = \hat{S}_i^x \pm \hat{S}_i^y$ are spin-flip operators. The spin stiffness of a world line configuration given in Eq. (3.53) reduces to

$$\rho_w = \frac{1}{L} \frac{1}{\beta} \Big(\sum_p \delta_{s_p, \pm 2} \, \mathrm{sign}\,(s_p) \Big)^2 \ . \tag{3.56}$$

Here, the sum over all plaquettes counts the number of vertices with $s = \pm 2$, which correspond to spin-flip processes. Since the counting also takes the sign of the vertex into consideration two different spin-flip processes cancel each other. If the spin stiffness takes a finite value, one kind of spin-flip process dominates. In the world line representation this corresponds to an imbalance between right and left going paths leading to world line winding [see Fig. 3.2]. Thus, the winding number $W \equiv \sum_p \delta_{s_p, \pm 2} \, \mathrm{sign}(s_p)$ is directly related to the spin stiffness.

Exact Diagonalization

4

The goal of many theoretical analyses is to solve a given model exactly. Unfortunately, this can only be done for just a small amount of simple models and in a few special cases. The exact diagonalization (ED) technique which is discussed in this chapter is a method which does solve the considered problem exactly, but has the great disadvantage that it is limited to very small system sizes. If the interest is in the properties of the thermodynamic limit this method cannot necessarily predict reliable results. However, the ED technique can be used for an extrapolation to the thermodynamic limit and thus it stands as a complementary method beside other numerical methods like quantum Monte Carlo simulation.

The principle of the ED technique is rather simple: One represents the Hamiltonian in an adequate basis and solves the problem by diagonalization of the matrix. The difficulty of this method is obvious. If one considers just a pure spin model with two possible alignments of the spin on each lattice site the Hilbert space in which the model is defined grows tremendously as 2^N if N denotes the lattice size. Therefore diagonalization of the corresponding Hamilton matrix very soon becomes impossible.

The Lanczos method extends the ED technique to larger system sizes. As described in this chapter, here the Hilbert space is reduced to a smaller subspace in which the ground state and the ground state energy can be determined more easily. Furthermore, within the Lanczos method dynamical properties can also be obtained as shown in section 4.3

4.1 Basic Mathematical Principles

Suppose $\mathbf{H}$ is a $N \times N$ matrix which cannot be diagonalized due to the large value of N and thus its eigenvectors and eigenvalues cannot be determined. The space $\mathfrak{H}$ in which $\mathbf{H}$ is defined obviously has the dimension N and is spanned by the vectors $\{\boldsymbol{\phi}_i\}$ with $i = 1, \ldots, N$. One chooses a subspace $\mathfrak{G} \subset \mathfrak{H}$ with dimension $M < N$ which is spanned by a set of vectors $\{\boldsymbol{\gamma}_i\}$. By reasons which become apparent in the following one defines a $N \times M$ matrix G which is composed by the vectors $\{\boldsymbol{\gamma}_i\}$:

$$[\mathsf{G}]_{ji} = [\gamma_i]_j \quad . \tag{4.1}$$

Furthermore, another matrix H_G is introduced:

$$\mathsf{H}_\mathsf{G} \equiv \mathsf{G}^\dagger \mathsf{H} \mathsf{G} \; . \tag{4.2}$$

with $\mathsf{G}^\dagger \mathsf{G} = \mathbf{1}$. As apparent, H_G has to be a $M \times M$ matrix and, if $M \ll N$, its eigenvalue equation can be solved much easier than for the matrix H:

$$\mathsf{H}_\mathsf{G}\, \boldsymbol{\psi}_i = \epsilon_i\, \boldsymbol{\psi}_i \; . \tag{4.3}$$

Here, $\boldsymbol{\psi}_i$ is an eigenvector of H_G and ϵ_i is the corresponding eigenvalue. By using Eq. (4.2) it follows

$$\mathsf{H} \left(\mathsf{G}\, \boldsymbol{\psi}_i \right) = \epsilon_i \left(\mathsf{G}\, \boldsymbol{\psi}_i \right) \; . \tag{4.4}$$

Obviously, ϵ_i is also an eigenvalue of the initial matrix H. Since the number of eigenvalues of H is larger than the number of eigenvalues of H_G not every eigenvalue of H can be obtained via the eigenvalue equation of H_G. Which eigenvalues one obtains depends on the choice of the subspace $\mathfrak{G}$. Furthermore, every eigenvector $\boldsymbol{\varphi}_i$ of H which belongs to an eigenvalue determined by Eq. (4.3) can be explicitly represented within the basis $\{\boldsymbol{\gamma}_i\}$. Let $\psi_j^{(i)}$ be the i-th component of the eigenvector $\boldsymbol{\psi}_j$. Then, according to Eq. (4.4) and Eq. (4.1) the eigenvector $\boldsymbol{\varphi}_j$ is given by

$$\boldsymbol{\varphi}_j = \mathsf{G}\, \boldsymbol{\psi}_j = \sum_i \psi_j^{(i)} \boldsymbol{\gamma}_i \; . \tag{4.5}$$

To determine the lowest eigenvalue ϵ_0 the corresponding eigenvector $\boldsymbol{\varphi}_0$ has to be within the subspace $\mathfrak{G}$. In the following it is shown how to construct a subspace $\mathfrak{K}$, called Krylov space, which contains the eigenvector $\boldsymbol{\varphi}_0$.

The idea is to generate successively elements out of $\mathfrak{H}$ by applying H to an arbitrary vector $\boldsymbol{\phi}_1 \in \mathfrak{H}$ with $\langle \boldsymbol{\varphi}_0 | \boldsymbol{\phi}_1 \rangle \neq 0$. The Krylov space is then given by

$$\mathfrak{K} = \mathrm{linspan} \left\{ \boldsymbol{\phi}_1 \, , \, \mathsf{H}\boldsymbol{\phi}_1 \, , \, \mathsf{H}^2 \boldsymbol{\phi}_1 \, , \, \ldots \, , \, \mathsf{H}^{M-1} \boldsymbol{\phi}_1 \right\} \; . \tag{4.6}$$

For the last element one obtains

$$\begin{aligned} \mathsf{H}^{M-1}\boldsymbol{\phi}_1 \quad &= \quad \mathsf{H}^{M-1} \sum_{i=0}^{N-1} c_i \boldsymbol{\varphi}_i = c_0 \epsilon_0^{M-1} \left(\boldsymbol{\varphi}_0 + \sum_{i=1}^{N-1} \frac{c_i}{c_0} \left(\frac{\epsilon_i}{\epsilon_0} \right)^{M-1} \boldsymbol{\varphi}_i \right) \\ &\simeq \quad c_0 \epsilon_0^{M-1} \boldsymbol{\varphi}_0 \quad \text{for} \quad M \gg 1 \; . \end{aligned} \tag{4.7}$$

c_i denotes expansion coefficients. Provided $|\epsilon_0| > |\epsilon_i|$ for all $i > 0$ the vector $\mathsf{H}^{M-1}\boldsymbol{\phi}_1$ converges to the eigenvector $\boldsymbol{\varphi}_0$ corresponding to the lowest eigenvalue ϵ_0. This implies that

(i) $\mathfrak{K}$ is (approximately) an invariant subspace of $\mathbf{H}$ and

(ii) $\boldsymbol{\varphi}_0$ lies within the subspace $\mathfrak{K}$.

The Lanczos method provides an orthogonalization procedure of the vectors given in Eq. (4.6). The new basis spans an (approximately) invariant subspace which contains the eigenvector $\boldsymbol{\varphi}_0$ of the lowest eigenvalue ϵ_0 of the initial matrix $\mathbf{H}$. Furthermore, the auxiliary matrix $\mathbf{H}_\mathsf{G}$ is tridiagonal within this new basis as shown in the next section 4.2 and thus can be solved very easily.

4.2 Lanczos Method

The problem under consideration is described by the Hamilton operator $\hat{\mathcal{H}}$ which is represented by the matrix $\mathbf{H}$. The basic idea of the Lanczos method is to construct a subspace $\mathscr{H}$ of the actual Hilbert space, in which the Hamiltonian has a tridiagonal representation $\mathbf{H}_n$ and can be solved more easily. If one uses the Krylov space as introduced in the previous section 4.1 for the subspace, namely

$$\mathscr{H} = \text{linspan}\left\{ |\phi_1\rangle \,, \hat{\mathcal{H}}|\phi_1\rangle \,, \hat{\mathcal{H}}^2|\phi_1\rangle \,, \ldots \,, \hat{\mathcal{H}}^n|\phi_1\rangle \right\} \,, \tag{4.8}$$

the ground state is within this subspace and the ground state energy can be determined by the Hamiltonian in tridiagonal representation. The basis states of the subspace are constructed in the following way: First one takes a randomly chosen state to be the initial state $|\phi_1\rangle$, which has only to fulfill the condition $\langle\varphi_0|\phi_1\rangle \neq 0$, where $|\varphi_0\rangle$ is the exact ground state of the problem. Then the next basis states are obtained recursively by

$$|\phi_{n+1}\rangle = \hat{\mathcal{H}}|\phi_n\rangle - a_n|\phi_n\rangle - b_n^2|\phi_{n-1}\rangle \,, \tag{4.9}$$

where $|\phi_0\rangle \equiv 0$. The coefficients a_n and b_n^2 are determined by

$$a_n = \frac{\langle\phi_n|\hat{\mathcal{H}}|\phi_n\rangle}{\langle\phi_n|\phi_n\rangle} \quad \text{and} \quad b_n^2 = \frac{\langle\phi_n|\phi_n\rangle}{\langle\phi_{n-1}|\phi_{n-1}\rangle} \tag{4.10}$$

with $b_1 \equiv 0$. The orthogonality of this set of basis states can be shown very easily by induction. Within this basis $\{|\phi_n\rangle\}$ the Hamiltonian is written in a tridiagonal form:

$$\mathbf{H}_n = \begin{pmatrix} a_1 & b_2 & 0 & 0 & \cdots & 0 \\ b_2 & a_2 & b_3 & 0 & \cdots & 0 \\ 0 & b_3 & a_3 & b_4 & \cdots & 0 \\ 0 & 0 & b_4 & a_4 & \cdots & 0 \\ \vdots & \vdots & \vdots & \vdots & \ddots & \vdots \\ 0 & 0 & 0 & 0 & \cdots & a_n \end{pmatrix} \,, \tag{4.11}$$

where n denotes the number of iterations done in Eq. (4.9). Usually, one starts with a small set of basis states and computes the eigenvalues by diagonalization of $\mathbf{H}_n$. With increasing number of iterations n the subspace $\mathscr{H}$ grows and the approximation of the ground state [see Eq. (4.7)] and thus the ground state energy becomes better. Typically for $n \approx 100$ the ground state energy is sufficiently converged [see appendix C].

Although $\mathbf{H}_n$ with $n \approx 100$ can be diagonalized very easily by computer based standard routines a bottle neck of this method is given by the limitation in memory capacity. To construct the matrix $\mathbf{H}_n$ one has to store at least three basis states within one iteration step [see Eq. (4.9)]. The dimension of each basis state corresponds to the dimension of the initial Hilbert space in which the problem is defined and thus grows exponentially with lattice size. If some prior information about the symmetries of the model is known, the initial Hilbert space can be reduced. For example, within a pure spin system the z-component $\hat{S}^z_{tot}$ of the total spin is conserved: $\left[\hat{\mathcal{H}}, \hat{S}^z_{tot}\right] = 0$. Since the Hamiltonian $\hat{\mathcal{H}}$ commutes with $\hat{S}^z_{tot}$ the Hamilton matrix $\mathbf{H}$ can be written in a block diagonal form where each block corresponds to a different magnetic quantum number. Therefore, every block in $\mathbf{H}$ can be solved separately. Of course, analog simplifications can be applied for other conserved quantities, such as lattice symmetries.

4.3 Dynamical Properties

The Lanczos method also allows to compute dynamical properties as explicitly shown in Refs. [1, 73, 74]. In this section attention is concentrated on the dynamical spin structure factor defined as [1]

$$S(\mathbf{q}, \omega) = -\frac{1}{\pi} \mathfrak{Im} \langle \varphi_0 | \hat{S}^-_{\mathbf{q}} \frac{1}{\omega + \epsilon_0 + \mathrm{i}\,\delta - \hat{\mathcal{H}}} \hat{S}^+_{\mathbf{q}} | \varphi_0 \rangle \,, \tag{4.12}$$

which expresses the spectral decomposition of the spin excitations. $|\varphi_0\rangle$ denotes the ground state of the system described by the Hamiltonian $\hat{\mathcal{H}}$. ϵ_0 stands for the ground state energy. By using the Dirac identity Eq. (4.12) can be rewritten as

$$S(\mathbf{q}, \omega) = \sum_i |\langle \varphi_i | \hat{S}^+_{\mathbf{q}} | \varphi_0 \rangle|^2 \delta\left(\omega - (\epsilon_i - \epsilon_0)\right) \,. \tag{4.13}$$

$|\varphi_i\rangle$ is an eigenstate of the Hamiltonian $\hat{\mathcal{H}}$ with energy ϵ_i. Suppose within a first Lanczos iteration the ground state of the problem is already determined, hence the initial state of a second Lanczos iteration can be set to

$$|\phi_1\rangle = \frac{\hat{S}^+_{\mathbf{q}} |\varphi_0\rangle}{\sqrt{\langle \varphi_0 | \hat{S}^-_{\mathbf{q}} \hat{S}^+_{\mathbf{q}} | \varphi_0 \rangle}} \,. \tag{4.14}$$

Eq. (4.13) then reads

$$S(\mathbf{q}, \omega) = \sum_i |\langle \varphi_i | \phi_1 \rangle|^2 \langle \varphi_0 | \hat{S}^+_{\mathbf{q}} \hat{S}^-_{\mathbf{q}} | \varphi_0 \rangle \delta\left(\omega - (\epsilon_i - \epsilon_0)\right) \,. \tag{4.15}$$

According to Eq. (4.5) an eigenstate $|\varphi_i\rangle$ can be expanded in terms of basis states $\{|\phi_j\rangle\}$ of the subspace $\mathscr{H}$:

$$|\varphi_i\rangle = \sum_j \psi_i^{(j)} |\phi_j\rangle \ . \tag{4.16}$$

The expansion coefficient $\psi_i^{(j)}$ can be taken from the i-th component of the eigenvector of the tridiagonal matrix $\mathbf{H}_n$. One obtains

$$\langle\phi_1|\varphi_i\rangle = \sum_j \psi_i^{(j)} \langle\phi_1|\phi_j\rangle = \psi_i^{(1)} \ . \tag{4.17}$$

Hence, for the dynamical spin structure factor it holds

$$S(\mathbf{q},\omega) = \sum_i |\psi_i^{(1)}|^2 \langle\varphi_0|\hat{S}^+_{\mathbf{q}}\hat{S}^-_{\mathbf{q}}|\varphi_0\rangle \delta\left(\omega - (\epsilon_i - \epsilon_0)\right) \ . \tag{4.18}$$

Thus, given an initial state as defined in Eq. (4.14) every energy ϵ_i is related to a spectral weight, which is determined by the absolute square of the first component $\psi_i^{(1)}$ of each eigenvector $\boldsymbol{\psi}_i$ when the tridiagonal Hamilton $\mathbf{H}_n$ matrix is diagonalized within a second Lanczos iteration. Usually one obtains a discrete spectrum which can be artificially broadened with Lorentz peaks.

The Kondo Necklace and Bilayer Heisenberg Model on a Square Lattice

5

The modeling of two dimensional (2D) spin systems has received attention in the context of high-temperature superconductors [75] and heavy fermion systems. This chapter focuses on the results of the study of the 2D Kondo necklace model (KNM) and the isotropic bilayer Heisenberg model (BHM). Both models are captured by the following Hamiltonian:

$$\hat{\mathcal{H}} = J_\perp \sum_{\mathbf{i}} \hat{\mathbf{S}}_{\mathbf{i}}^{(1)} \cdot \hat{\mathbf{S}}_{\mathbf{i}}^{(2)} + \sum_{\langle \mathbf{ij} \rangle} \sum_{m} J_\parallel^{(m)} \hat{\mathbf{S}}_{\mathbf{i}}^{(m)} \cdot \hat{\mathbf{S}}_{\mathbf{j}}^{(m)} \, . \tag{5.1}$$

Here, $\hat{\mathbf{S}}_{\mathbf{i}}^{(m)}$ is the spin-1/2 operator which acts on a spin degree of freedom at site $\mathbf{i}$. $J_\parallel^{(m)}$ stands for the intralayer exchange, and the upper index $m = 1, 2$ labels the two different layers. $J_\perp$ denotes the interlayer coupling. For the different types of model one has to set

$$\begin{array}{lll} J_\parallel^{(1)} \equiv J_\parallel \quad \text{and} \quad J_\parallel^{(2)} = 0 & \text{for the KNM and} \\ J_\parallel^{(1)} = J_\parallel^{(2)} = J_\parallel & \text{for the BHM.} \end{array} \tag{5.2}$$

Both models exhibit a quantum phase transition from an antiferromagnetically ordered phase to a disordered phase, which will be explicitly shown in the following section.

5.1 Quantum Phase Transition

In the weak coupling limit ($J_\perp \ll J_\parallel$) the BHM consists of two weakly coupled antiferromagnetically ordered planes. The KNM shows antiferromagnetic (AF) ordering within the first layer. However, with increasing interplane coupling both systems tend to dimerize. Due to AF coupling the spins of neighboring sites on different layers prefer to form singlets which leads to a breakdown of the AF order. Thus, both systems exhibit a magnetic order-disorder quantum phase transition as a function of the interlayer coupling $J_\perp$.

To demonstrate this quantum phase transition and to test the numerical method for both models, the BHM and the KNM, the quantum critical point as well as critical exponents are determined. For this the spin stiffness, which indicates the degree of spin order in

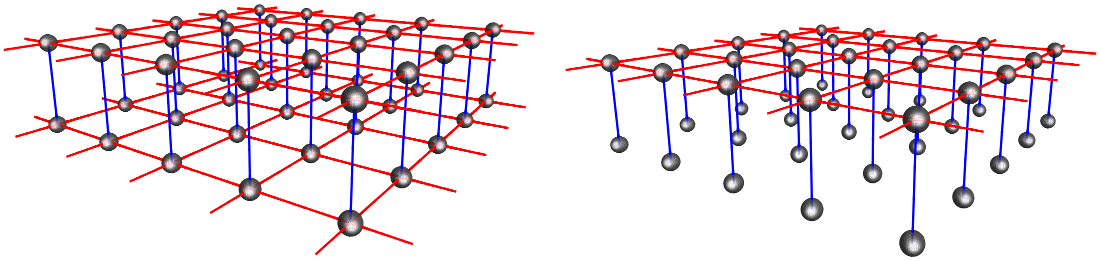

(a) Bilayer Heisenberg model

(b) Kondo necklace model

Figure 5.1: Sketch of the isotropic BHM and the 2D KNM. The red lines correspond to the antiferromagnetic coupling $J_{\|}$. The blue lines indicate the interlayer coupling $J_{\perp}$.

the system, is computed. In section 2.3 a motivation of its definition is given. The spin stiffness reads:

$$\rho_s = -\frac{1}{L^{d-2}} \frac{1}{\beta} \frac{\partial^2}{\partial \phi^2} \ln Z(\phi) \bigg|_{\phi=0} , \tag{5.3}$$

where d is the dimensionality. In the presence of long-range order ρ_s takes a finite value and in the disordered phase it vanishes. In subsection 3.4.4 the implementation of the spin stiffness into the world line algorithm is explicitly shown.

Fig. 5.2(a) and Fig. 5.2(c) plot the spin stiffness for the BHM and the KNM as a function of lattice size. The presented data still show finite size effects, so an extrapolation to the thermodynamic limit is carried out by fitting to the form $\rho_s \propto a + b/L$ in the range $L = 8 \ldots 16$. The extrapolated data for the BHM and KNM are depicted in Fig. 5.2(b) and Fig. 5.2(d) and fitted to the form

$$\rho_s \propto \left[\left(\frac{J_{\perp}}{J_{\|}} \right)_c - \left(\frac{J_{\perp}}{J_{\|}} \right) \right]^{\nu} . \tag{5.4}$$

For the KNM one obtains $\left(J_{\perp}/J_{\|}\right)_c = 1.3780 \pm 0.020$ and a critical exponent of $\nu = 0.662 \pm 0.087$. The value for the critical exponent agrees well with the value of Ref. [76]. The value for the critical point is slightly below the literature value of Ref. [77]: $\left(J_{\perp}/J_{\|}\right)_c = 1.41 \pm 0.02$, but still within the error bars. Similar simulations for the BHM yield a value of $\left(J_{\perp}/J_{\|}\right)_c \simeq 2.51$ in good agreement with the literature value: $\left(J_{\perp}/J_{\|}\right)_c = 2.525 \pm 0.002$ [78]. The critical exponent ν in the BHM is found to agree well with that of Ref. [76]; hence confirming the point of view that both the BHM and the KNM belong to the same universality class. In Ref. [79] the BHM and the KNM are approached via a dimer series expansion. Within this framework the numerical results above compare quite well. Recent high-precision calculations presented in Ref. [80] yield a critical value of $\left(J_{\perp}/J_{\|}\right)_c = 2.5220(1)$ for the BHM and $\left(J_{\perp}/J_{\|}\right)_c = 1.3888(1)$ for the KNM.

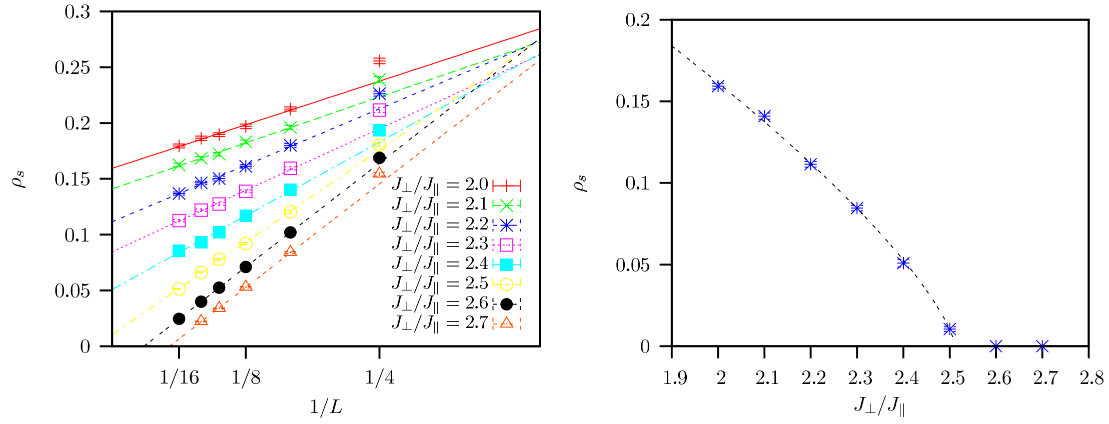

(a) Finite size scaling for the BHM

(b) Result for the BHM (Fit: $J_\perp/J_\parallel = 2.0 \ldots 2.5$)

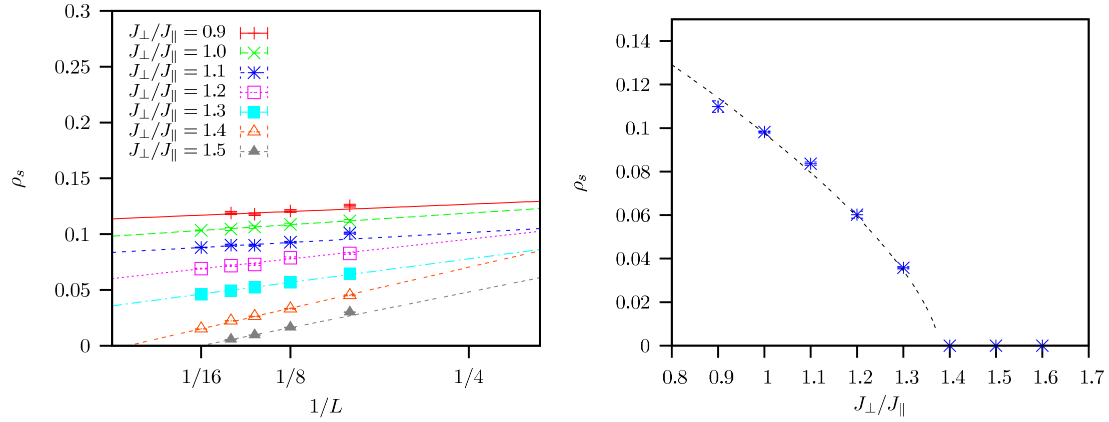

(c) Finite size scaling for the KNM

(d) Result for the KNM (Fit: $J_\perp/J_\parallel = 1.0 \ldots 1.3$)

Figure 5.2: (a,c) Spin stiffness ρ_s as a function of linear size L for different interplanar couplings $J_\perp/J_\parallel$. Extrapolation to the thermodynamic limit is carried out by fitting to the form $\rho_s \propto a + b/L$ (range of fit $L = 8 \ldots 16$). (b,d) Extrapolated values of the spin stiffness as a function of $J_\perp/J_\parallel$. The dashed lines corresponds to the fit according to the form of Eq. (5.4). Simulations are carried out at $\beta J_\parallel = 50.0$ for $L = 16$ and $\beta J_\parallel = 30.0$ for all other lattice sizes ($\Delta\tau J_\parallel = 0.02$).

5.2 Spin Dynamics in the BHM

In this section excitation spectra of the BHM in the disordered phase are presented. For $J_\perp \to \infty$ the system exclusively consists of singlet dimers. That means that the ground state wave function is a tensor product of singlets in each unit cell, which is given by two neighboring spins on different layers. Starting from this state, an excitation (magnon) corresponds to breaking a singlet to form a triplet. These excitation are reflected by the dynamical spin susceptibility.

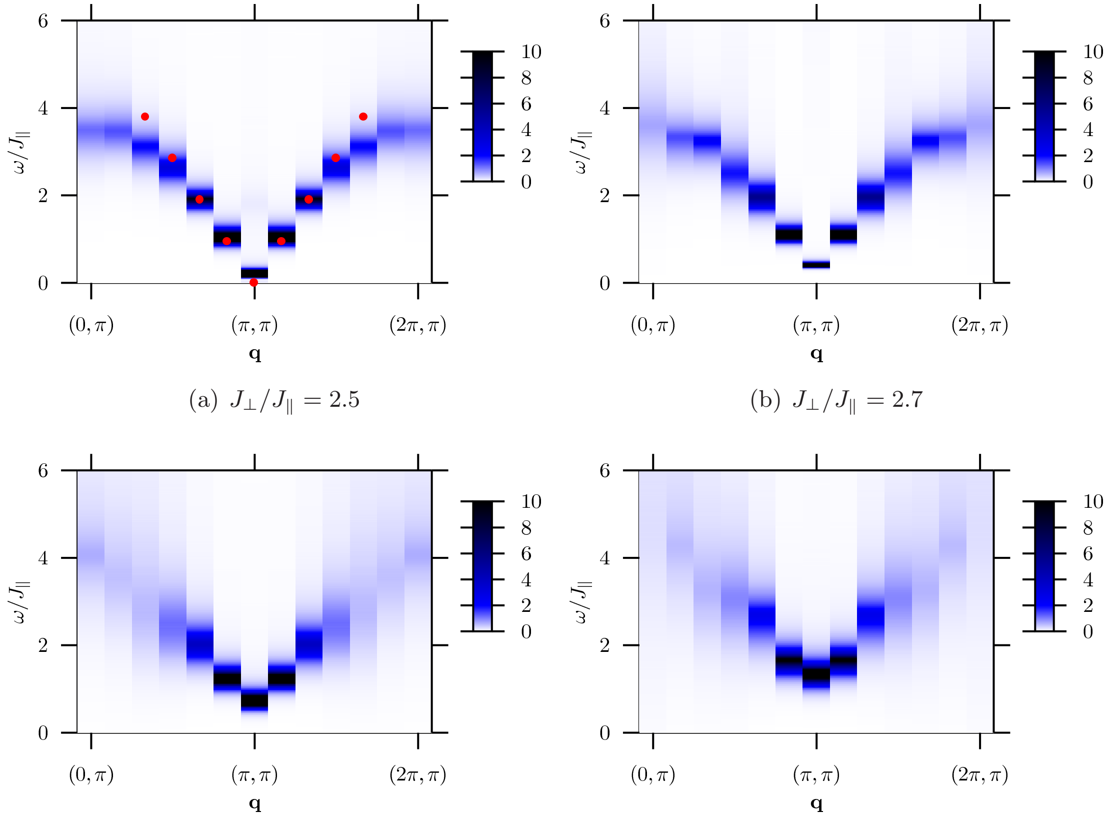

(a) $J_\perp/J_\parallel = 2.5$

(b) $J_\perp/J_\parallel = 2.7$

(c) $J_\perp/J_\parallel = 3.0$

(d) $J_\perp/J_\parallel = 3.5$

Figure 5.3: Dynamical spin susceptibility for different couplings on a 12×12 lattice in the BHM ($\beta J_\parallel = 30.0$, $\Delta\tau J_\parallel = 0.02$). The red points in 5.3(a) reflect the dispersion given by Eq. (5.21).

5.2.1 Dynamical Spin Susceptibility

Within the QMC it is easy to obtain the spin correlations $\langle \hat{S}^z_{\mathbf{i}}(\tau)\hat{S}^z_{\mathbf{j}}(0)\rangle$ in real space and imaginary time τ, where the imaginary time evolution of the spin operator reads $\hat{S}^z_{\mathbf{i}}(\tau) = e^{\tau\hat{\mathcal{H}}}\hat{S}^z_{\mathbf{i}}e^{-\tau\hat{\mathcal{H}}}$. Its representation in momentum space is related to the dynamical spin susceptibility $S(\mathbf{q},\omega)$ via

$$\langle \hat{S}^z_{\mathbf{q}}(\tau)\hat{S}^z_{-\mathbf{q}}(0)\rangle = \frac{1}{\pi}\int d\omega\, e^{-\tau\omega} S(\mathbf{q},\omega)\ . \tag{5.5}$$

By using the stochastic maximum entropy (ME) method [81] one can extract the dynamical spin susceptibility. Fig. 5.3 plots the dynamical spin structure factor as a function of $J_\perp/J_\parallel$ for the BHM. In the deeply disordered phase the dispersion has a cosine like shape. In first order perturbation theory in $J_\parallel/J_\perp$, the magnon acquires a dispersion relation

$$\Omega(\mathbf{q}) \sim J_\perp + \tfrac{1}{2}J_\parallel\gamma(\mathbf{q}) \tag{5.6}$$

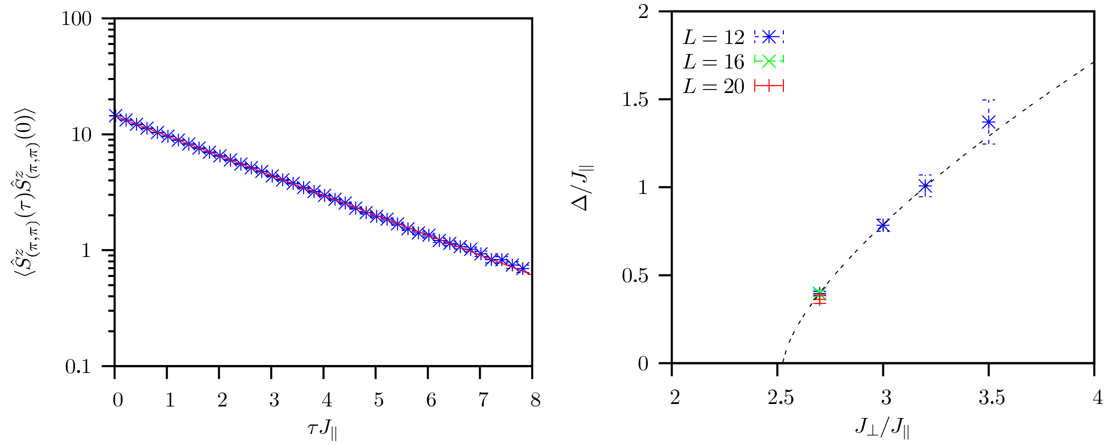

(a) Spin correlation function at $J_\perp/J_{\|} = 2.7$

(b) Spin gap as a function of $J_\perp$

Figure 5.4: (a) Spin correlation function in imaginary time τ at $J_\perp/J_{\|} = 2.7$ ($\beta J_{\|} = 30.0$, $L = 12$, $\Delta\tau J_{\|} = 0.02$). The data is fitted to the form given in Eq. (5.7) in order to extract the spin gap. (b) Spin gap as a function of interleg coupling $J_\perp$. Fit according to Eq. (5.8). Temperature used: $\beta J_{\|} = 30.0$ for $L = 12$, $\beta J_{\|} = 50.0$ for $L = 16$ and $\beta J_{\|} = 70.0$ for $L = 20$.

with $\gamma(\mathbf{q}) = 2\left(\cos(q_x) + \cos(q_y)\right)$.

This approximative approach is roughly consistent with the large-$J_\perp$ case in Fig. 5.3(d). For large values of τ and on any finite lattice, the spin correlation function is dominated by the lowest excitations:

$$\langle S^z_{\mathbf{q}}(\tau)S^z_{-\mathbf{q}}(0)\rangle \propto e^{-\Omega(\mathbf{q})\tau} \quad \text{for} \quad \tau J_{\|} \gg 1 \ , \tag{5.7}$$

where $\Omega(\mathbf{q})$ stands for the momentum dependent gap to the first spin excitation.

In Fig. 5.4 the spin correlation function for $J_\perp/J_{\|} = 2.7$ ($L = 12$) and the spin gap as a function of $J_\perp/J_{\|}$ are depicted. The gap energy Δ is obtained from the asymptotic behavior of the spin correlations: $\Delta \equiv \min\left[\Omega(\mathbf{q})\right]$. For this the spin correlation function is fitted to the form given in Eq. (5.7) as shown Fig. 5.4(a). The gap Δ is depicted in Fig. 5.4(b) for different coupling ratios $J_\perp/J_{\|}$. As a function of decreasing coupling $J_\perp$ the spin gap progressively closes as

$$\Delta \propto \left[\left(\frac{J_\perp}{J_{\|}}\right) - \left(\frac{J_\perp}{J_{\|}}\right)_c\right]^\nu \ , \tag{5.8}$$

where $\left(J_\perp/J_{\|}\right)_c = 2.525 \pm 0.02$ [78] denotes the critical coupling. At the critical coupling the magnons at $\mathbf{q} = (\pi, \pi)$ condense to form the antiferromagnetic order. This physics is also captured by the following bond mean field approximation.

5.2.2 Bond Mean Field Approach

In this subsection a bond mean field calculation for the bilayer Heisenberg model is presented. The bond mean field approach [82] is a strong coupling approximation in $J_\perp$. The spins between layers dominantly form singlets and the density of triplets is *low*. This assumption allows one to neglect triplet-triplet interaction. The bond operator representation describes the system in a basis of pairs of coupled spins, which can either be in a singlet or triplet state:

$$\begin{array}{rclcl} |s\rangle_{\mathbf{i}} & = & \hat{s}^\dagger_{\mathbf{i}}|0\rangle_{\mathbf{i}} & = & \frac{1}{\sqrt{2}}(|\uparrow\downarrow\rangle_{\mathbf{i}} - |\downarrow\uparrow\rangle_{\mathbf{i}}) \\ |t_x\rangle_{\mathbf{i}} & = & \hat{t}^\dagger_{\mathbf{i},x}|0\rangle_{\mathbf{i}} & = & \frac{-1}{\sqrt{2}}(|\uparrow\uparrow\rangle_{\mathbf{i}} - |\downarrow\downarrow\rangle_{\mathbf{i}}) \\ |t_y\rangle_{\mathbf{i}} & = & \hat{t}^\dagger_{\mathbf{i},y}|0\rangle_{\mathbf{i}} & = & \frac{\mathrm{i}}{\sqrt{2}}(|\uparrow\uparrow\rangle_{\mathbf{i}} + |\downarrow\downarrow\rangle_{\mathbf{i}}) \\ |t_z\rangle_{\mathbf{i}} & = & \hat{t}^\dagger_{\mathbf{i},z}|0\rangle_{\mathbf{i}} & = & \frac{1}{\sqrt{2}}(|\uparrow\downarrow\rangle_{\mathbf{i}} + |\downarrow\uparrow\rangle_{\mathbf{i}}) \ . \end{array} \tag{5.9}$$

However, in the limit $J_\perp \to \infty$ the ground state is a product state of singlet bonds on each rung [83]:

$$|\Psi_0\rangle = \bigotimes_{\mathbf{i}} |s\rangle_{\mathbf{i}} \ . \tag{5.10}$$

The excitations in this limit are given by localized triplets. The operators defined in Eq. (5.9) satisfy Bose commutation rules provided that one imposes the constraint

$$\hat{s}^\dagger_{\mathbf{i}}\hat{s}_{\mathbf{i}} + \sum_{\alpha} \hat{t}^\dagger_{\mathbf{i},\alpha}\hat{t}_{\mathbf{i},\alpha} = \hat{\mathbb{1}} \ . \tag{5.11}$$

The original spin-1/2 degrees of freedom read [82]

$$\hat{S}^{(1,2)}_{\mathbf{i},\alpha} \;=\; \tfrac{1}{2}\Big(\pm\, \hat{s}^\dagger_{\mathbf{i}}\hat{t}_{\mathbf{i},\alpha} \pm \hat{t}^\dagger_{\mathbf{i},\alpha}\hat{s}_{\mathbf{i}} - \mathrm{i}\sum_{\beta,\gamma} \epsilon_{\alpha\beta\gamma}\hat{t}^\dagger_{\mathbf{i},\beta}\hat{t}_{\mathbf{i},\gamma}\Big) \ . \tag{5.12}$$

On the left hand side of Eq. (5.12) the lower indices α now denote the different components of the spin operator. $\epsilon_{\alpha\beta\gamma}$ stands for the totally antisymmetric Levi-Civita tensor. The Hamiltonian (5.1) for the BHM can then be rewritten in the bond operator representation:

$$\begin{aligned} \hat{\mathcal{H}} \;=\; & J_\perp \sum_{\mathbf{i}} \Big(-\tfrac{3}{4}\hat{s}^\dagger_{\mathbf{i}}\hat{s}_{\mathbf{i}} + \tfrac{1}{4}\sum_{\alpha}\hat{t}^\dagger_{\mathbf{i},\alpha}\hat{t}_{\mathbf{i},\alpha}\Big) - \sum_{\mathbf{i}} \mu_{\mathbf{i}}\Big(\hat{s}^\dagger_{\mathbf{i}}\hat{s}_{\mathbf{i}} + \sum_{\alpha}\hat{t}^\dagger_{\mathbf{i},\alpha}\hat{t}_{\mathbf{i},\alpha} - \hat{\mathbb{1}}\Big) \\ & + \frac{J_\parallel}{2} \sum_{\langle \mathbf{ij}\rangle}\sum_{\alpha} \Big(\hat{s}^\dagger_{\mathbf{i}}\hat{s}^\dagger_{\mathbf{j}}\hat{t}_{\mathbf{i},\alpha}\hat{t}_{\mathbf{j},\alpha} + \hat{s}^\dagger_{\mathbf{i}}\hat{s}_{\mathbf{j}}\hat{t}_{\mathbf{i},\alpha}\hat{t}^\dagger_{\mathbf{j},\alpha} + \mathrm{H.\,c.}\Big) \\ & + \frac{J_\parallel}{2} \sum_{\alpha,\beta,\gamma} \Big(\hat{t}^\dagger_{\mathbf{i},\beta}\hat{t}_{\mathbf{i},\gamma}\hat{t}^\dagger_{\mathbf{j},\beta}\hat{t}_{\mathbf{j},\gamma} - \hat{t}^\dagger_{\mathbf{i},\beta}\hat{t}_{\mathbf{i},\gamma}\hat{t}^\dagger_{\mathbf{j},\gamma}\hat{t}_{\mathbf{j},\beta}\Big) \ . \end{aligned} \tag{5.13}$$

$\mu_{\mathbf{i}}$ is a Lagrange parameter which enforces locally the constraint (5.11). The interplanar part shows the characteristic Hamiltonian of two antiferromagnetically coupled spins whereas the intraplanar part includes the interaction between singlets and triplets of different bonds. Now the standard method of Sachdev and Bhatt [82] is followed. In the disordered phase one expects a singlet condensate ($\bar{s} = \langle s \rangle \neq 0$). Additionally the constraint given by Eq. (5.11) is imposed only on average ($\mu_{\mathbf{i}} = \mu$). As mentioned above one neglects triplet-triplet interactions. Apart from a constant one obtains the following mean field Hamiltonian in momentum space:

$$\hat{\mathcal{H}}_{\mathrm{MF}} = \sum_{\alpha}\sum_{\mathbf{q}} A_{\mathbf{q}} \hat{t}^{\dagger}_{\mathbf{q},\alpha}\hat{t}_{\mathbf{q},\alpha} + \sum_{\alpha}\sum_{\mathbf{q}} \frac{B_{\mathbf{q}}}{2}(\hat{t}^{\dagger}_{\mathbf{q},\alpha}\hat{t}^{\dagger}_{-\mathbf{q},\alpha} + \mathrm{H.\,c.}) \; , \tag{5.14}$$

where

$$A_{\mathbf{q}} = \frac{J_{\perp}}{4} - \mu + J_{\|}\bar{s}^2\big(\cos(q_x) + \cos(q_y)\big) \quad \text{and} \tag{5.15}$$

$$B_{\mathbf{q}} = J_{\|}\bar{s}^2\big(\cos(q_x) + \cos(q_y)\big) \; . \tag{5.16}$$

The parameters μ and $\bar{s} = \langle s \rangle$ are determined by the saddle point equations

$$\left\langle \frac{\partial \hat{\mathcal{H}}_{\mathrm{MF}}}{\partial \mu} \right\rangle = 0 \quad \text{and} \quad \left\langle \frac{\partial \hat{\mathcal{H}}_{\mathrm{MF}}}{\partial \bar{s}} \right\rangle = 0 \; . \tag{5.17}$$

The Hamiltonian is diagonalized by a Bogoliubov transformation [17]:

$$\hat{\alpha}^{\dagger}_{\mathbf{q},\alpha} = u_{\mathbf{q}}\hat{t}^{\dagger}_{\mathbf{q},\alpha} - v_{\mathbf{q}}\hat{t}_{-\mathbf{q},\alpha} \; . \tag{5.18}$$

In terms of magnon creation and annihilation operators the mean field Hamiltonian (5.14) writes

$$\hat{\mathcal{H}}_{\mathrm{MF}} = \sum_{\mathbf{q}}\sum_{\alpha} \Omega(\mathbf{q})\hat{\alpha}^{\dagger}_{\mathbf{q},\alpha}\hat{\alpha}_{\mathbf{q},\alpha} \; . \tag{5.19}$$

The Bogoliubov coefficients $u_{\mathbf{q}}$ and $v_{\mathbf{q}}$ satisfy the relation $u^2_{\mathbf{q}} - v^2_{\mathbf{q}} = 1$, which follows from the bosonic nature of the magnons: $\left[\hat{\alpha}_{\mathbf{q}}, \hat{\alpha}^{\dagger}_{\mathbf{q}'}\right] = \delta_{\mathbf{q}\mathbf{q}'}$. The coefficients are given by

$$u_{\mathbf{q}}, v_{\mathbf{q}} = \sqrt{\frac{A_{\mathbf{q}}}{2\Omega(\mathbf{q})} \pm \frac{1}{2}} \; , \tag{5.20}$$

where $\Omega(\mathbf{q}) = \sqrt{A^2_{\mathbf{q}} - B^2_{\mathbf{q}}}$ is the magnon dispersion. In the vicinity of the critical point it can be approximated by

$$\Omega(\mathbf{q}) = \sqrt{\Delta^2 + \mathrm{v}_s^2(\mathbf{q} - \mathbf{Q})^2} \tag{5.21}$$

with Δ the energy gap to magnon excitations, v_s the magnon velocity and $\mathbf{Q} = (\pi, \pi)$. Eq. (5.21) gives an accurate description of the dispersion relation in the vicinity of the critical point [see Fig. 5.3(a)]. At the critical point the gap Δ vanishes, so that the triplets can condense thus forming the AF static ordering.

5.3 Single Hole Dynamics

In this section the system is doped with a single mobile hole. The motion of the hole is restricted to one layer thereby staying in the spirit of Kondo lattice models. To understand the coupling of the hole to magnetic fluctuations within the magnetic disordered phase one can extend the previously described bond mean field approximation [see Eq. (5.19)] to account for the hole motion. This is done in the following subsection 5.3.1. In the subsequent subsection results of the spectra and a discussion of the effective mass of a mobile hole are presented. Finally, in subsection 5.4 the delicate issue of the quasiparticle residue (QPR) of the hole in the vicinity of the magnetic quantum phase transition is analyzed.

5.3.1 Bond Mean Field Approach with Single Hole

To include the single hole dynamics into the mean field approach of the BHM [see Eq. (5.19)] one initially uses an intuitive description of the doped system given by a formulation in terms of dimer states. For this one introduces the operator $\hat{c}^{\dagger}_{\mathbf{i},(\sigma_1\sigma_2)}$ which creates a dimer state at site $\mathbf{i}$ with spin σ_1 in layer 1 and spin σ_2 in layer 2:

$$\hat{c}^{\dagger}_{\mathbf{i},(\sigma_1\sigma_2)}|\mathrm{vac}\rangle = |\sigma_1\sigma_2\rangle_{\mathbf{i}} \tag{5.22}$$

with $\sigma_m = +1$ for an up-spin and $\sigma_m = -1$ for a down-spin. Furthermore an operator $\hat{h}^{\dagger}_{\mathbf{i},\sigma}$ which creates a hole with spin σ in layer 1 at site $\mathbf{i}$ is introduced:

$$\hat{h}^{\dagger}_{\mathbf{i},\sigma}|\mathrm{vac}\rangle \quad = \quad |\,0\,\sigma\rangle_{\mathbf{i}} \ . \tag{5.23}$$

Since the analysis is restricted to a single hole the considered Hilbert space is given by

$$\left\{ |\Psi\rangle = \bigotimes_{\mathbf{i}} |\sigma_1\sigma_2\rangle_{\mathbf{i}} \;\middle|\; \langle\Psi| \sum_{\mathbf{i}} \sum_{\sigma} \hat{h}^{\dagger}_{\mathbf{i},\sigma}\hat{h}_{\mathbf{i},\sigma}|\Psi\rangle = 1 \right\} \ . \tag{5.24}$$

For the explicit calculation one has to differentiate between the coupling of a propagating hole to magnons and the coupling of a hole at rest to magnons. For a hole which propagates between two sites one regards the following process: A hole is annihilated and a dimer state is created at site $\mathbf{j}$, while at site $\mathbf{i}$ a dimer state is annihilated and a hole is created. The corresponding two site Hamiltonian writes

$$\hat{\mathcal{H}}^{(ij)}_t = t \sum_{\sigma_1,\sigma_2,\sigma_3} \left[\hat{h}^{\dagger}_{\mathbf{i},\sigma_3}\hat{c}_{\mathbf{i},(\sigma_1\sigma_3)}\hat{c}^{\dagger}_{\mathbf{j},(\sigma_1\sigma_2)}\hat{h}_{\mathbf{j},\sigma_2} + \mathrm{H.\,c.} \right] \ . \tag{5.25}$$

The sums run over all possible static spin configurations. Every ancillary spin-flip process is excluded. t stands for the hopping matrix element of the propagating hole. Another possible process, where the hole can couple to the magnetic fluctuations is given, when the hole in the upper layer rests and the corresponding spins on the second layer interact.

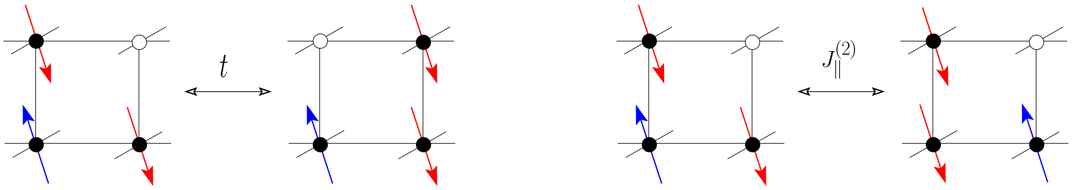

(a) Propagating hole (b) Hole at rest

Figure 5.5: Two possible processes where the hole can couple to magnons: (a) The hole moves to a nearest neighbor and couples via $g_a(\mathbf{p},\mathbf{q})$ to magnons. (b) The hole is at rest. The coupling to magnons is denoted by $g_b(\mathbf{p},\mathbf{q})$.

This interaction between two neighboring spins on layer 2 is usually characterized by the Heisenberg Hamiltonian $J_\parallel^{(2)}\sum_{\langle\mathbf{ij}\rangle}\hat{\mathbf{S}}_\mathbf{i}\cdot\hat{\mathbf{S}}_\mathbf{j}$. In terms of the operators of Eq. (5.22) and Eq. (5.23) this Hamiltonian writes

$$\begin{aligned}\hat{\mathcal{H}}_J^{(ij)} &= J_\parallel^{(2)}\sum_{\sigma_1,\sigma_2,\sigma_3}\Bigg[\frac{\sigma_2\sigma_3}{4}\,\hat{c}^\dagger_{\mathbf{i},(\sigma_1\sigma_2)}\hat{c}_{\mathbf{i},(\sigma_1\sigma_2)}\hat{h}^\dagger_{\mathbf{j},\sigma_3}\hat{h}_{\mathbf{j},\sigma_3}\\ &\qquad\qquad + \frac{\delta_{\sigma_2,-\sigma_3}}{2}\,\hat{c}^\dagger_{\mathbf{i},(\sigma_1\sigma_3)}\hat{c}_{\mathbf{i},(\sigma_1\sigma_2)}\hat{h}^\dagger_{\mathbf{j},\sigma_2}\hat{h}_{\mathbf{j},\sigma_3}\Bigg]\,. \end{aligned}\tag{5.26}$$

The first term of Eq. (5.26) corresponds to the $\hat{S}^z_\mathbf{i}\hat{S}^z_\mathbf{j}$-part of the Heisenberg Hamiltonian, the second term corresponds to the $\hat{S}^\pm_\mathbf{i}\hat{S}^\mp_\mathbf{j}$-part. The processes described by the two site Hamiltonians of Eq. (5.25) and Eq. (5.26) are sketched in Fig. 5.5 and are summed up to the total Hamiltonian that is considered to describe the coupling of a hole to magnetic fluctuations:

$$\hat{\mathcal{H}} = \sum_{\langle ij\rangle}\hat{\mathcal{H}}_t^{(ij)} + \hat{\mathcal{H}}_J^{(ij)}\,. \tag{5.27}$$

The mapping between the dimer operator of Eq. (5.22) and the bond operators introduced in Eq. (5.9) is also very intuitive

$$\begin{aligned}\hat{c}^\dagger_{\mathbf{i},(11)} &= -\tfrac{1}{\sqrt{2}}\left(\hat{t}^\dagger_{\mathbf{i},x}+\mathrm{i}\,\hat{t}^\dagger_{\mathbf{i},y}\right) & \hat{c}^\dagger_{\mathbf{i},(-11)} &= \tfrac{1}{\sqrt{2}}\left(\hat{t}^\dagger_{\mathbf{i},z}-\hat{s}^\dagger_\mathbf{i}\right)\\ \hat{c}^\dagger_{\mathbf{i},(1-1)} &= \tfrac{1}{\sqrt{2}}\left(\hat{t}^\dagger_{\mathbf{i},z}+\hat{s}^\dagger_\mathbf{i}\right) & \hat{c}^\dagger_{\mathbf{i},(-1-1)} &= \tfrac{1}{\sqrt{2}}\left(\hat{t}^\dagger_{\mathbf{i},x}-\mathrm{i}\,\hat{t}^\dagger_{\mathbf{i},y}\right)\end{aligned}\tag{5.28}$$

and is summarized by

$$\hat{c}^\dagger_{\mathbf{i},(\sigma_1\sigma_2)} = -\delta_{\sigma_1\sigma_2}\frac{\sigma_1}{\sqrt{2}}\left(\hat{t}^\dagger_{\mathbf{i},x}+\mathrm{i}\,\sigma_1\hat{t}^\dagger_{\mathbf{i},y}\right)+\delta_{\sigma_1,-\sigma_2}\frac{1}{\sqrt{2}}\left(\hat{t}^\dagger_{\mathbf{i},z}+\sigma_1\hat{s}^\dagger_\mathbf{i}\right)\,. \tag{5.29}$$

In the following the Hamiltonian of Eq. (5.27) is formulated in the representation given by Eq. (5.29) and Fourier transformed into the momentum space. By neglecting the magnon-magnon interaction, which means that one has to consider only terms that are bilinear in

$\hat{t}^{\dagger}_{\mathbf{i},\alpha}$ and $\hat{t}_{\mathbf{i},\alpha}$, one obtains the following Hamiltonian:

$$\begin{aligned}\hat{\mathcal{H}} \;=\;& \frac{t}{2N}\sum_{\mathbf{p}_1,\mathbf{p}_2}\sum_{\mathbf{q}}\sum_{\sigma}\gamma(\mathbf{q})\Big[\Big(\hat{s}^{\dagger}_{\mathbf{p}_1}\hat{s}_{\mathbf{p}_2}-\sigma\hat{t}^{\dagger}_{\mathbf{p}_1,z}\hat{s}_{\mathbf{p}_2}-\sigma\hat{s}^{\dagger}_{\mathbf{p}_1}\hat{t}_{\mathbf{p}_2,z}\Big)\hat{h}^{\dagger}_{\mathbf{p}_2+\mathbf{q},\sigma}\hat{h}_{\mathbf{p}_1+\mathbf{q},\sigma}-\\ &\qquad\Big(\hat{t}^{\dagger}_{\mathbf{p}_1,x}-\mathrm{i}\,\sigma\hat{t}^{\dagger}_{\mathbf{p}_1,y}\Big)\hat{s}_{\mathbf{p}_2}\hat{h}^{\dagger}_{\mathbf{p}_2+\mathbf{q},\sigma}\hat{h}_{\mathbf{p}_1+\mathbf{q},-\sigma}-\\ &\qquad\hat{s}^{\dagger}_{\mathbf{p}_1}\left(\hat{t}_{\mathbf{p}_2,x}+\mathrm{i}\,\sigma\hat{t}_{\mathbf{p}_2,y}\right)\hat{h}^{\dagger}_{\mathbf{p}_2+\mathbf{q},-\sigma}\hat{h}_{\mathbf{p}_1+\mathbf{q},\sigma}\Big]\\ +\;& \frac{J^{(2)}_{\parallel}}{8N}\sum_{\mathbf{p}_1,\mathbf{p}_2}\sum_{\mathbf{q}}\sum_{\sigma}\gamma(\mathbf{q})\Big[\Big(-\sigma\hat{t}^{\dagger}_{\mathbf{p}_1,z}\hat{s}_{\mathbf{p}_1+\mathbf{q}}-\sigma\hat{s}^{\dagger}_{\mathbf{p}_1}\hat{t}_{\mathbf{p}_1+\mathbf{q}}\Big)\hat{h}^{\dagger}_{\mathbf{p}_2+\mathbf{q},\sigma}\hat{h}_{\mathbf{p}_2,\sigma}-\\ &\qquad\Big(\hat{t}^{\dagger}_{\mathbf{p}_1,x}-\mathrm{i}\,\sigma\hat{t}^{\dagger}_{\mathbf{p}_1,y}\Big)\hat{s}_{\mathbf{p}_1+\mathbf{q}}\hat{h}^{\dagger}_{\mathbf{p}_2+\mathbf{q},\sigma}\hat{h}_{\mathbf{p}_2,-\sigma}-\\ &\qquad\hat{s}^{\dagger}_{\mathbf{p}_1}\left(\hat{t}_{\mathbf{p}_1+\mathbf{q},x}+\mathrm{i}\,\sigma\hat{t}_{\mathbf{p}_1+\mathbf{q},y}\right)\hat{h}^{\dagger}_{\mathbf{p}_2+\mathbf{q},-\sigma}\hat{h}_{\mathbf{p}_2,\sigma}\,\Big]\;. \end{aligned}\tag{5.30}$$

where $\gamma(\mathbf{q})=2\left(\cos(q_x)+\cos(q_y)\right)$. To handle this Hamiltonian a mean field approximation is applied as was also done in subsection 5.2.2: $\langle\hat{s}^{\dagger}_{\mathbf{i}}\rangle=\bar{s}$. Since the system is in the disordered phase one expects a singlet condensate, thus

$$\langle\hat{s}_{\mathbf{p}}\rangle=\langle\hat{s}^{\dagger}_{\mathbf{p}}\rangle=\frac{1}{\sqrt{N}}\sum_{\mathbf{i}}\langle\hat{s}^{\dagger}_{\mathbf{i}}\rangle e^{\mathrm{i}\,\mathbf{p}\cdot\mathbf{i}}=\sqrt{N}\,\bar{s}\,\delta_{\mathbf{0},\mathbf{p}}\;. \tag{5.31}$$

This approximation leads to the following mean field Hamiltonian

$$\begin{aligned}\hat{\mathcal{H}}_{\mathrm{MF}} \;=\;& \frac{t\bar{s}^2}{2}\sum_{\mathbf{q}}\gamma(\mathbf{q})\hat{\mathrm{h}}^{\dagger}_{\mathbf{q}}\hat{\mathrm{h}}_{\mathbf{q}}-\frac{t\bar{s}}{2\sqrt{N}}\sum_{\mathbf{p}}\sum_{\mathbf{q}}\gamma(\mathbf{q})\left[\hat{\mathbf{t}}^{\dagger}_{\mathbf{p}}\cdot\left(\hat{\mathrm{h}}^{\dagger}_{\mathbf{q}}\boldsymbol{\sigma}\hat{\mathrm{h}}_{\mathbf{p}+\mathbf{q}}\right)+\mathrm{H.\,c.}\right]\\ &-\frac{J^{(2)}\bar{s}}{8\sqrt{N}}\sum_{\mathbf{p}}\sum_{\mathbf{q}}\gamma(\mathbf{q})\left[\hat{\mathbf{t}}^{\dagger}_{\mathbf{q}}\cdot\left(\hat{\mathrm{h}}^{\dagger}_{\mathbf{p}}\boldsymbol{\sigma}\hat{\mathrm{h}}_{\mathbf{p}+\mathbf{q}}\right)+\mathrm{H.\,c.}\right]\end{aligned}\tag{5.32}$$

with spinor $\hat{\mathrm{h}}_{\mathbf{q}}=\left(\hat{h}_{\mathbf{p},\uparrow},\hat{h}_{\mathbf{p},\downarrow}\right)^{\mathsf{T}}$ and vector $\hat{\mathbf{t}}_{\mathbf{q}}=\left(\hat{t}_{\mathbf{q},x},\hat{t}_{\mathbf{q},y},\hat{t}_{\mathbf{q},z}\right)^{\mathsf{T}}$. $\boldsymbol{\sigma}=(\sigma_1,\sigma_2,\sigma_3)^{\mathsf{T}}$ denotes the Pauli matrices. To add the single hole dynamics to the mean field Hamiltonian of the undoped System in Eq. (5.19) the above Hamiltonian (5.32) should be rewritten in terms of magnon creation and annihilation operators as introduced in subsection 5.2.2. The inverse transformation of Eq. (5.18) is given by

$$\hat{\mathbf{t}}^{\dagger}_{\mathbf{q}}=v_{\mathbf{q}}\boldsymbol{\alpha}_{-\mathbf{q}}+u_{\mathbf{q}}\boldsymbol{\alpha}^{\dagger}_{\mathbf{q}}\;. \tag{5.33}$$

Using this Bogoliubov transformation the whole mean field Hamiltonian, which includes the kinetic energy of the magnons, the kinetic energy of the hole and the coupling of the hole to magnons is given by

$$\hat{\mathcal{H}}_{\mathrm{MF}}=\sum_{\mathbf{q}}\Omega(\mathbf{q})\hat{\boldsymbol{\alpha}}^{\dagger}_{\mathbf{q}}\hat{\boldsymbol{\alpha}}_{\mathbf{q}}+\sum_{\mathbf{p}}\varepsilon(\mathbf{p})\hat{\mathrm{h}}^{\dagger}_{\mathbf{p}}\hat{\mathrm{h}}_{\mathbf{p}}+\sum_{\mathbf{p},\mathbf{q}}\left[g(\mathbf{p},\mathbf{q})\,\boldsymbol{\alpha}_{\mathbf{q}}\cdot\left(\hat{\mathrm{h}}^{\dagger}_{\mathbf{p}+\mathbf{q}}\boldsymbol{\sigma}\hat{\mathrm{h}}_{\mathbf{p}}\right)+\mathrm{H.\,c.}\right]\;, \tag{5.34}$$

where $\varepsilon(\mathbf{p}) = t\bar{s}^2\left(\cos(q_x) + \cos(q_y)\right)$ is the mean field dispersion of the hole. The coupling $g(\mathbf{p},\mathbf{q})$ between the hole and the magnons splits into two parts:

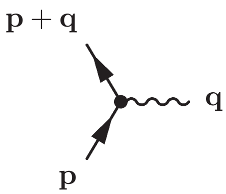

$$: \quad g(\mathbf{p},\mathbf{q}) = g_a(\mathbf{p},\mathbf{q}) + g_b(\mathbf{p},\mathbf{q}) \ . \tag{5.35}$$

One identifies the two coupling constants with the processes that are shown in Fig. 5.5: $g_a(\mathbf{p},\mathbf{q})$ is proportional to the hopping matrix element and hence describes the coupling of a mobile hole to the magnetic background, whereas $g_b(\mathbf{p},\mathbf{q})$ is proportional to $J_{\parallel}^{(2)}$ and describes the coupling of a hole at rest with the magnons. The calculations give the following momentum dependent coupling strengths:

$$g_a(\mathbf{p},\mathbf{q}) \quad = \quad -\frac{t\bar{s}}{2\sqrt{N}}\big(\gamma(\mathbf{p}+\mathbf{q})v(\mathbf{q}) + \gamma(\mathbf{p})u(\mathbf{q})\big) \tag{5.36}$$

$$g_b(\mathbf{p},\mathbf{q}) \quad = \quad -\frac{J_{\parallel}^{(2)}\bar{s}}{8\sqrt{N}}\gamma(\mathbf{q})\big(v(\mathbf{q}) + u(\mathbf{q})\big) \ . \tag{5.37}$$

A discussion of the coupling strengths is given in subsection 5.4.1 in detail.

5.3.2 Spectra and Effective Mass of a Mobile Hole

In section 3.3 as well as in Refs. [71, 84] it is shown how to implement the Green's function for a single doped hole into the world line algorithm of a quantum Monte Carlo simulation. The spin dynamics is simulated with the loop algorithm. For each fixed spin configuration one can readily compute the Green's function. From the Green's function $\mathcal{G}_{\mathbf{p}}(\tau)$ in imaginary time τ one can extract the single particle spectral function $A(\mathbf{p},\omega)$ with the stochastic maximum entropy method [81]:

$$\mathcal{G}_{\mathbf{p}}(\tau) = \frac{1}{\pi}\int_0^\infty d\omega\, e^{-\tau\omega} A(\mathbf{p},-\omega) \ . \tag{5.38}$$

For the bare hole dispersion the mean field calculation of subsection 5.3.1 yields

$$\varepsilon(\mathbf{p}) = +t\bar{s}^2\big(\cos(p_x) + \cos(p_y)\big) \ . \tag{5.39}$$

In the limit $J_\perp \to \infty$ the magnon excitation energy diverges and hence the coupling of the hole to magnetic excitations becomes negligible. In other words, in this limit the magnon excitations become quite rare, so that: $\bar{s} \equiv \langle s \rangle \approx 1$. Thus, in the strong coupling region one obtains from Eq. (5.34) a hole dispersion relation:

$$E(\mathbf{p}) = t\big(\cos(p_x) + \cos(p_y)\big) \ . \tag{5.40}$$

This agrees with the result given by applying perturbation theory in $t/J_\perp$ [21].

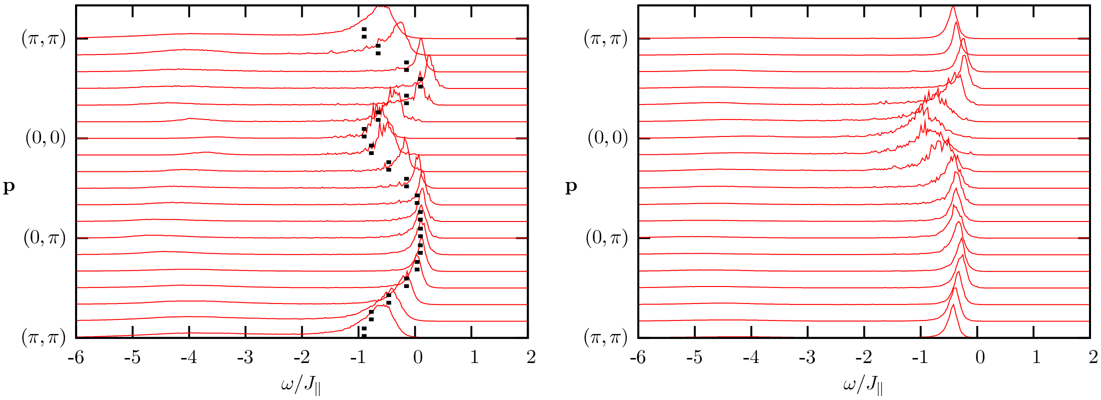

(a) $J_\perp/J_\parallel = 1.0$

(b) $J_\perp/J_\parallel = 2.0$

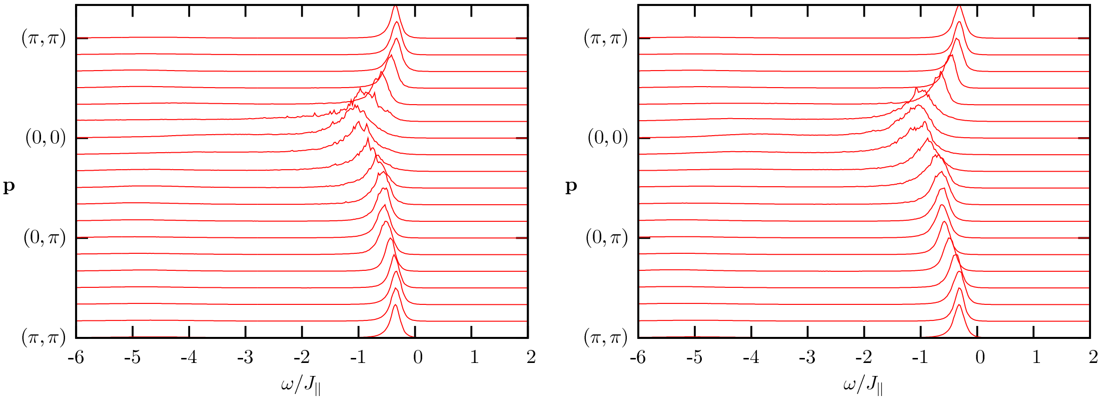

(c) $J_\perp/J_\parallel = 2.3$

(d) $J_\perp/J_\parallel = 2.4$

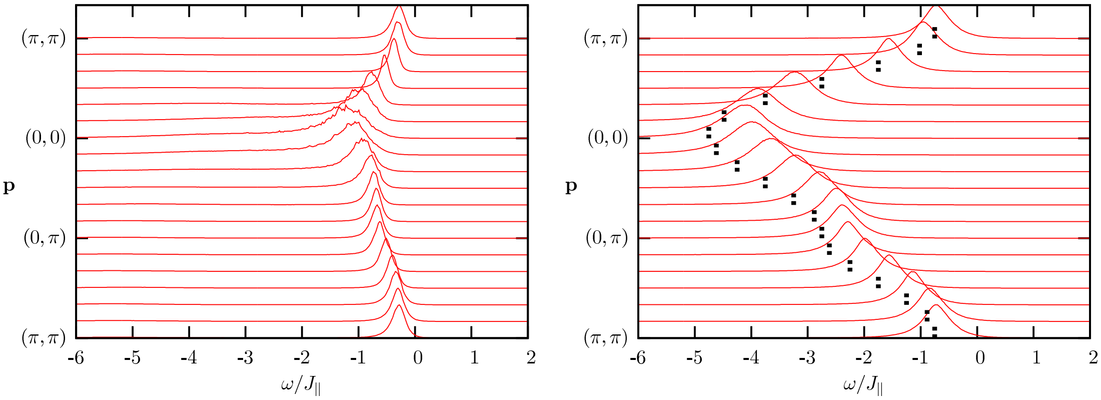

(e) $J_\perp/J_\parallel = 2.5$

(f) $J_\perp/J_\parallel = 10.0$

Figure 5.6: Spectra of a mobile hole for a 12×12 lattice in the isotropic bilayer Heisenberg model ($\beta J_\parallel = 30.0$, $\Delta\tau J_\parallel = 0.02$). The small dashed lines in 5.6(f) tag the dispersion of a free particle, in 5.6(a) they outline a dispersion of the form: $E(\mathbf{p}) = J_\parallel\left(\cos(p_x) + \cos(p_y)\right)^2$.

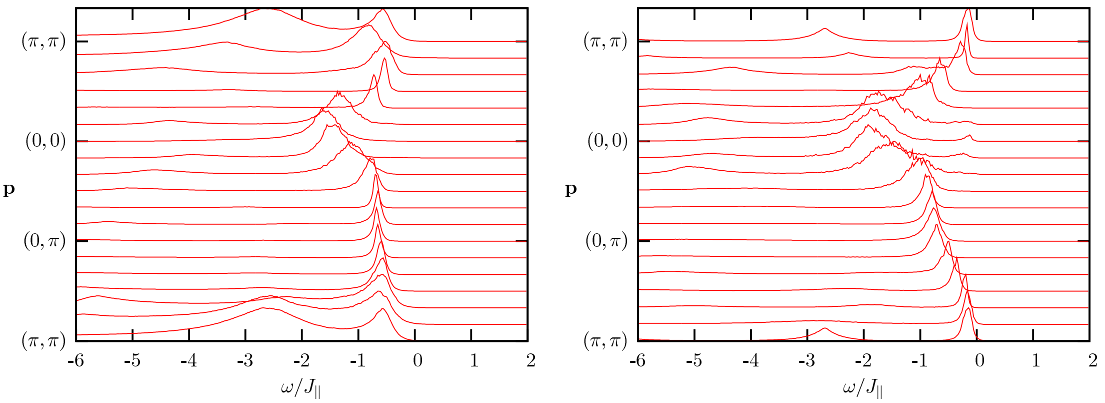

(a) $J_\perp/J_\parallel = 0.5$ (b) $J_\perp/J_\parallel = 1.0$

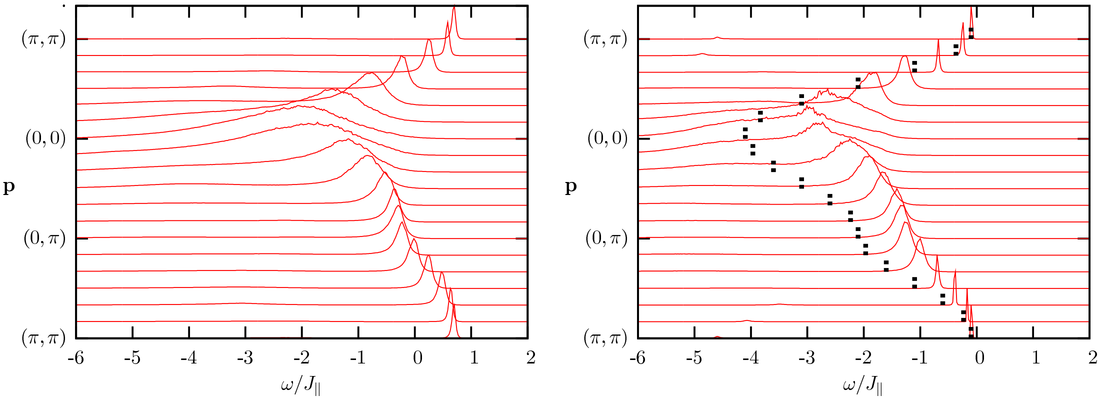

(c) $J_\perp/J_\parallel = 1.5$ (d) $J_\perp/J_\parallel = 2.0$

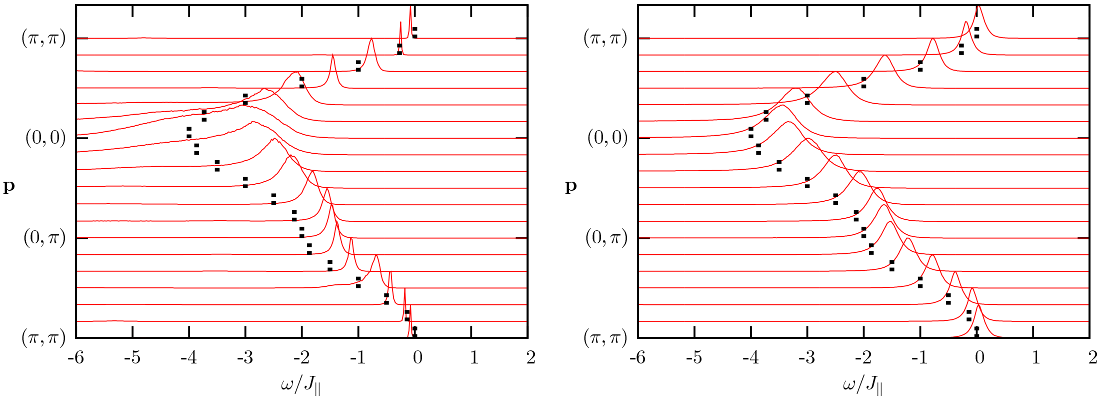

(e) $J_\perp/J_\parallel = 2.5$ (f) $J_\perp/J_\parallel = 4.0$

Figure 5.7: Spectra of a mobile hole for a 12×12 lattice in the 2D Kondo necklace model ($\beta J_\parallel = 30.0$, $\Delta\tau J_\parallel = 0.02$). The small dashed lines in 5.6(d), 5.6(e) and 5.6(f) tag the dispersion of a free particle.

As apparent from Fig. 5.6 and Fig. 5.7 the strong coupling behavior is reproduced by the Monte Carlo simulations where the dispersion exhibits a cosine form with maximum at $\mathbf{p} = (\pi, \pi)$. The form of this dispersion relation directly reflects the singlet formation – in other words Kondo screening – between spin degrees of freedom on different layers. One should note that this strong coupling behavior of the dispersion relation sets in at larger values of $J_\perp/J_\parallel$ for the BHM than for the KNM. This is quite reasonable since in the BHM the single bonds are coupled among each other within both layers. With decreasing coupling ratio the bandwidth of the quasiparticle dispersion relation diminishes but the overall features of the strong coupling remain. In the weak coupling limit considerable differences are observed between the single particle spectrum of the BHM and KNM. The following discussion starts with the BHM. For this model the point $J_\perp/J_\parallel = 0$ is well defined (i.e. the ground state is non-degenerate on any finite lattice) and corresponds to two independent Heisenberg planes with mobile hole in the upper plane. The problem of the single hole in a two dimensional Heisenberg model has been addressed in the framework of the self-consistent Born approximation [85] and yields a dispersion relation given by

$$E(\mathbf{p}) = J_\parallel \left(\cos(p_x) + \cos(p_y)\right)^2 \ . \tag{5.41}$$

Since at $J_\perp/J_\parallel = 0$ a well defined ground state is apparent one can expect that turning on a small value of $J_\perp/J_\parallel$ will not alter the single hole dispersion relation. This point of view is confirmed in Fig. 5.6(a). At $J_\perp/J_\parallel = 1.0$, the single hole dispersion is well reproduced by Eq. (5.41). Hence and as confirmed by Figs. 5.6 the dispersion relation of a single hole in the BHM continuously deforms from the strong coupling form of Eq. (5.40) to that of a doped hole in a planar antiferromagnet [see Eq. (5.41)]. Hence, as a function of $J_\perp/J_\parallel$ there is a point where the effective mass diverges at $\mathbf{p} = (\pi, \pi)$. The effective mass m_{eff} is given by the inverse curvature of the dispersion relation. In general m_{eff} is defined as an *effective mass tensor* [5]:

$$\left[m_{\text{eff}}^{-1}\right]_{\alpha\beta} = \pm \frac{\partial^2 E(\mathbf{p})}{\partial p_\alpha \partial p_\beta} \ , \tag{5.42}$$

where α and β denote directions in momentum space. However, for simplicity and due to symmetry arguments in the following the effective mass is assumed to be

$$m_{\text{eff}}^{-1} = \frac{\partial^2 E(\mathbf{p})}{\partial p_x^2} = \frac{\partial^2 E(\mathbf{p})}{\partial p_y^2} \simeq \frac{E(\mathbf{p} - \Delta\mathbf{p}) - 2E(\mathbf{p}) + E(\mathbf{p} + \Delta\mathbf{p})}{(\Delta\mathbf{p})^2} \tag{5.43}$$

with $\Delta\mathbf{p} = (0, 2\pi/L)$. Upon inspection of the data [see Fig. 5.6], the point of divergence of the effective mass is not related to the magnetic quantum phase transition since it occurs slightly below $\left(J_\perp/J_\parallel\right)_c$. This is explicitly illustrated in Fig. 5.8, which shows the excitation energy for the BHM for the lattice sizes $L = 8$ and $L = 12$. One can see that there is no size scaling within the error bars for all considered values of $J_\perp/J_\parallel$. As Fig. 5.8(d) shows, the graphs for $J_\perp/J_\parallel = 2.5$, which is slightly below the critical

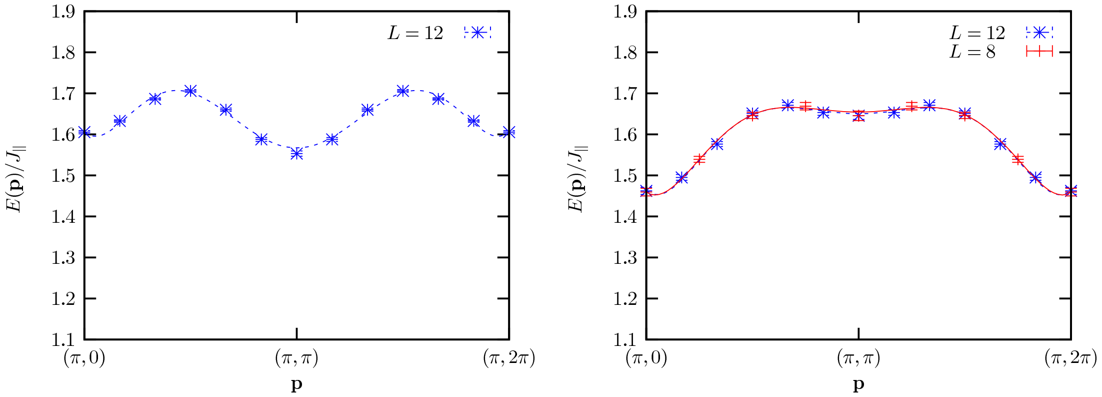

(a) $J_\perp/J_\parallel = 2.0$

(b) $J_\perp/J_\parallel = 2.3$

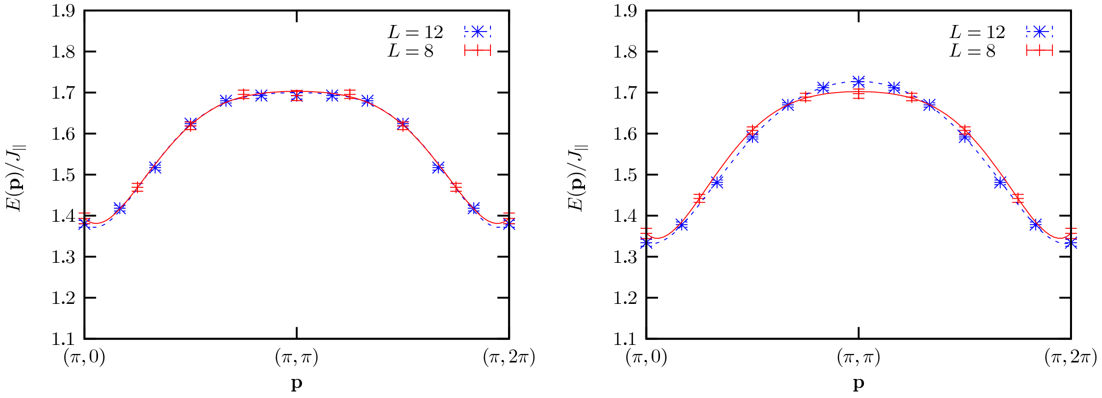

(c) $J_\perp/J_\parallel = 2.4$

(d) $J_\perp/J_\parallel = 2.5$

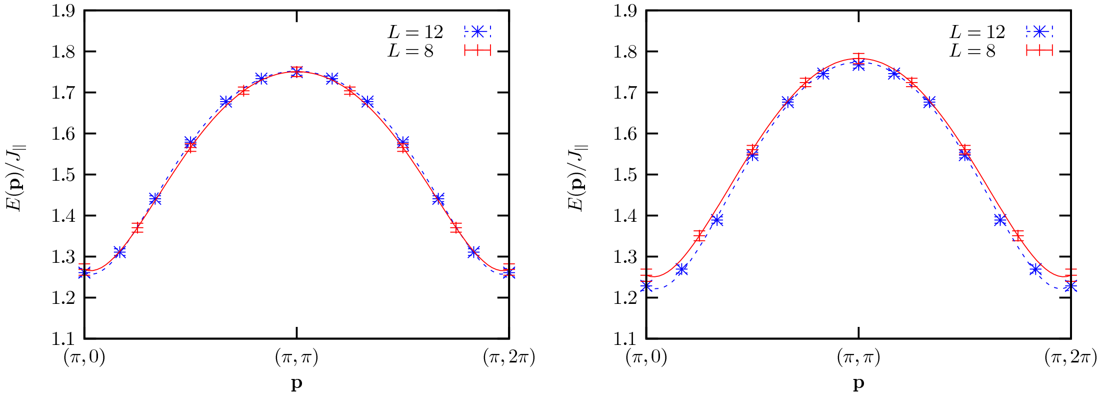

(e) $J_\perp/J_\parallel = 2.6$

(f) $J_\perp/J_\parallel = 2.7$

Figure 5.8: Single hole dispersion $E(\mathbf{p})$ for different values of $J_\perp/J_\parallel$ for $L = 8$ and $L = 12$ in the BHM ($\beta J_\parallel = 30.0$, $\Delta\tau J_\parallel = 0.02$). The curvature of the graphs at $\mathbf{p} = (\pi, \pi)$ changes around $J_\perp/J_\parallel = 2.4$ which indicates the divergence of the effective mass.

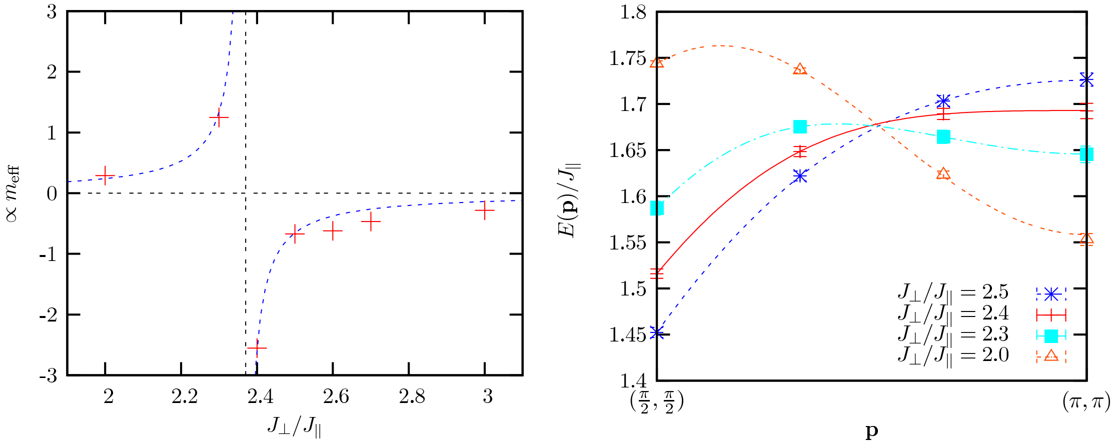

(a) Divergence of effective mass

(b) Drift of dispersion maximum

Figure 5.9: (a) Sketch of the divergence of the effective mass m_{eff} as defined in Eq. (5.43) for the BHM on a 12×12 lattice ($\beta J_\parallel = 30.0$, $\Delta\tau J_\parallel = 0.02$). The Divergence is not related to the quantum critical point. (b) Single hole dispersion $E(\mathbf{p})$ for different values of $J_\perp/J_\parallel$ for $L = 12$ ($\beta J_\parallel = 30.0$, $\Delta\tau J_\parallel = 0.02$). The maximum of the dispersion drifts from $\mathbf{p} = (\pi, \pi)$ for large $J_\perp$ to $\mathbf{p} = (\pi/2, \pi/2)$ for small $J_\perp$.

value, still have a negative curvature at $\mathbf{p} = (\pi, \pi)$. The curvature at $\mathbf{p} = (\pi, \pi)$ changes around $J_\perp/J_\parallel = 2.4$ which indicates the divergence of the effective mass. Furthermore it becomes apparent that the point of divergence is not related to the quantum critical point. Fig 5.9(a) depicts the effective mass explicitly computed by Eq. (5.43) depending on the coupling $J_\perp/J_\perp$. Since Eq. (5.43) is just an approximate formula, the results presented in Fig 5.9(a) represent a sketch of the development of the effective mass as a function of $J_\perp/J_\perp$ without any error bars and without claim to be precise. Nevertheless it gives some insight to the divergence of the effective mass in the BHM. As a result of the change of the curvature the maximum of the dispersion drifts from $\mathbf{p} = (\pi, \pi)$ to $\mathbf{p} = (\pi/2, \pi/2)$ as illustrated in Fig. 5.9(b). This crossover between a dispersion with maximum at $\mathbf{p} = (\pi, \pi)$ and maximum at $\mathbf{p} = (\pi/2, \pi/2)$ with a crossover point lying inside the AF ordered phase is also documented in Ref. [86].

The above argument cannot be applied to the KNM, since the $J_\perp/J_\parallel = 0$ point is macroscopically degenerate and hence it is not a good starting point to understand the weak coupling physics. Clearly the same holds for the KLM and UKLM. Inspection of the spectral data deep in the ordered phase of the KNM [see Fig. 5.7(a)] shows that the maximum of the dispersion relation is still pinned at $\mathbf{p} = (\pi, \pi)$ such that the strong coupling features stemming from Kondo screening are still present at weak couplings. For the KNM, down to the lowest couplings considered in this study, the effective mass at $\mathbf{p} = (\pi, \pi)$ increases as a function of decreasing coupling strength but does not seem to diverge at finite values of $J_\perp/J_\|$. Precisely the same conclusion is reached in the framework of the KLM [22] and UKLM [23].

5.4 Quasiparticle Residue

In this section attention is turned to the delicate issue of the quasiparticle residue in the vicinity of the magnetic quantum phase transition. First this question is addressed within the framework of the mean field model of Eq. (5.34). Here, the single particle Green's function is computed by means of a self-consistent Born approximation. The renormalization coefficient [87] of the one-hole Green's function, the quasiparticle residue [7, 88], is defined for a resonance $\omega = \xi_i$ as

$$\mathcal{Z}(\mathbf{p}) \equiv \left| 1 - \frac{\partial}{\partial \omega} \mathfrak{Re}\, \Sigma(\mathbf{p}, \omega) \right|^{-1}_{\omega = \xi_i} , \tag{5.44}$$

where $\Sigma(\mathbf{p}, \omega)$ denotes the self-energy of the hole. In a second step, the quasiparticle residue is directly determined from the Monte Carlo data.

5.4.1 Analytical Approach

In the following the coupling to critical magnetic fluctuations is considered. Hence, one has to concentrate on $\mathbf{q} = (\pi, \pi) \equiv \mathbf{Q}$ and set the system in the proximity of the quantum phase transition on the disordered side. In this case the magnon dispersion as defined in subsection 5.2.2 vanishes ($\Omega(\mathbf{Q}) \to 0$) and the coherence factors $u_\mathbf{q}$ and $v_\mathbf{q}$ from Eq. (5.20) scales as

$$u_\mathbf{q}, v_\mathbf{q} \propto \Omega(\mathbf{q})^{-\frac{1}{2}} . \tag{5.45}$$

Since furthermore $\gamma(\mathbf{p} + \mathbf{Q}) = -\gamma(\mathbf{p})$ one finds that the coupling of a propagating hole to magnons, characterized by $g_a(\mathbf{p}, \mathbf{Q})$ vanishes at the critical point. In other words process (a) couples only to short range spin fluctuations. On the other hand in the vicinity of the critical point g_b scales as $g_b(\mathbf{p}, \mathbf{q}) \propto \Omega(\mathbf{q})^{-\frac{1}{2}}$ so that retention of this term only is all that is needed to understand the coupling to critical fluctuations. Summarizing one can set

$$g(\mathbf{p}, \mathbf{q}) \to g_b(\mathbf{q}) \propto \frac{1}{\sqrt{\Omega(\mathbf{q})}} \tag{5.46}$$

for the subsequent calculations. It is intriguing to note that in this simple approximation $g_b(\mathbf{q})$ scales as $J_\|^{(2)}$, which is strictly speaking zero in the KNM. However, such a coupling would be dynamically generated via an RKKY-type interaction [16, 17, 18, 19]. With the coupling above the first order self-energy is given by

$$\Sigma^{(1)}(\mathbf{p},\omega) \; = \tag{5.47}$$

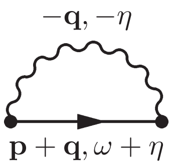

$$= \; \mathrm{i}\int \mathrm{d}^2\mathbf{q}\int \mathrm{d}\eta\; g_b^2(\mathbf{q})\;\mathcal{G}_0(\mathbf{p}+\mathbf{q},\omega+\eta)\;\mathcal{D}_0(-\mathbf{q},-\eta)\;.$$

Here, the free propagators for the hole $\mathcal{G}_0$ and for the magnons $\mathcal{D}_0$ reads

$$\mathcal{G}_0(\mathbf{p},\omega)=\frac{1}{\omega-\varepsilon(\mathbf{p})+\mathrm{i}\,0^+}\quad\text{and}\quad\mathcal{D}_0(\mathbf{q},\omega)=\frac{1}{\omega-\Omega(\mathbf{q})+\mathrm{i}\,0^+}\;, \tag{5.48}$$

where $\varepsilon(\mathbf{p})$ is the dispersion relation of the hole. For the magnon dispersion relation one adopts the form of Eq. (5.21) which is suitable in the vicinity of the phase transition and for $\mathbf{q}\rightarrow\mathbf{Q}$:

$$\Omega(\mathbf{q})=\sqrt{\Delta^2+\mathrm{v}_s^2(\mathbf{q}-\mathbf{Q})^2}\;. \tag{5.49}$$

The calculation presented in appendix A yields the first order self energy

$$\Sigma^{(1)}(\mathbf{p},\omega)=\int \mathrm{d}^2\mathbf{q}\; g_b^2(\mathbf{q})\;\frac{1}{\omega-\varepsilon(\mathbf{p}+\mathbf{q})-\Omega(\mathbf{q})}\;. \tag{5.50}$$

According to Eq. (5.44) the self-energy has to be evaluated at its poles. Bearing in mind that $\Omega(\mathbf{Q})\rightarrow 0$ in the vicinity of the critical couplings a pole is found for $\omega=\varepsilon$. In this case the wave vectors have to satisfy the condition

$$\varepsilon(\mathbf{p})=\varepsilon(\mathbf{p}+\mathbf{Q}) \tag{5.51}$$

and the self-energy takes the form

$$\Sigma^{(1)}(\mathbf{p},\omega)=-\int \mathrm{d}^2\tilde{\mathbf{q}}\;\frac{g_b^2(\tilde{\mathbf{q}}+\mathbf{Q})}{\Omega(\tilde{\mathbf{q}}+\mathbf{Q})}\;, \tag{5.52}$$

where the integration variable is transformed: $\mathbf{q}\rightarrow\tilde{\mathbf{q}}=\mathbf{q}-\mathbf{Q}$. Finally one has to consider that $g_b(\tilde{\mathbf{q}})\propto\Omega^{-\frac{1}{2}}(\tilde{\mathbf{q}})$ [see Eq. (5.46)] for the coupling to critical fluctuations, so that one arrives at

$$\Sigma^{(1)}(\mathbf{p},\omega)\propto\int_{\mathrm{BZ}}\mathrm{d}^2\tilde{\mathbf{q}}\;\frac{1}{\Omega^2(\tilde{\mathbf{q}}+\mathbf{Q})}\propto\int_{\mathrm{BZ}}\mathrm{d}^2\tilde{\mathbf{q}}\;\frac{1}{\tilde{\mathbf{q}}^2}\propto\int_0^{\tilde{q}_{\max}}\frac{\mathrm{d}\tilde{q}}{\tilde{q}} \tag{5.53}$$

with $\tilde{q}\equiv|\tilde{\mathbf{q}}|$. Now it can be seen, that for the condition given in Eq. (5.51) the self-energy diagram shows a logarithmic divergence. Hence one has to sum up all diagrams.

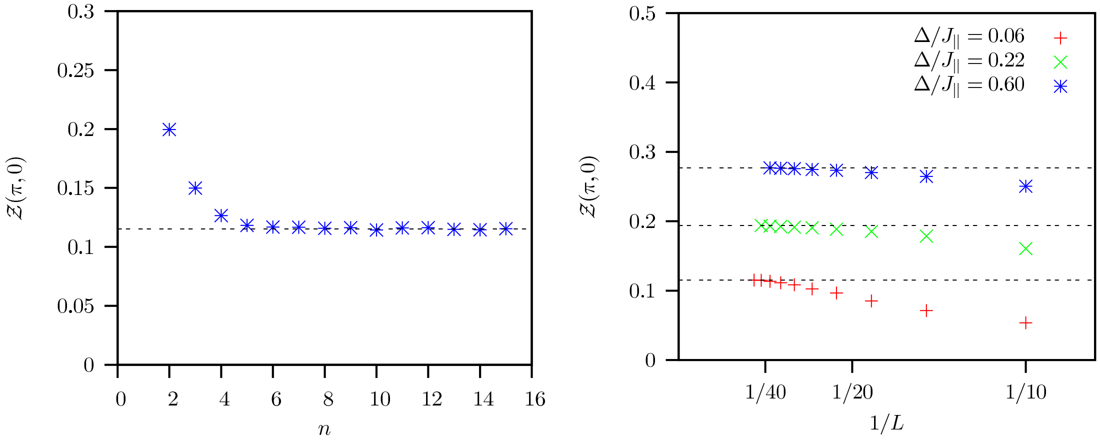

(a) Iterations within SCB

(b) Sizescaling

Figure 5.10: Self-consistent Born approximation in the BHM for $\mathbf{p} = (\pi, 0)$: (a) QPR after n-th iterations for $\Delta/J_{\|} = 0.06$ and $L = 46$. (b) QPR depending on the linear system size L for different spin gaps Δ.

This is done in the non-crossing or self-consistent Born approximation which in the limit $\beta \to \infty$ boils down to the following self-consistent equations:

$$\Sigma(\mathbf{p},\omega) \;=\; \frac{1}{N}\sum_{\mathbf{q}} g^2(\mathbf{q})\,\mathcal{G}(\mathbf{p}-\mathbf{q},\omega-\Omega(\mathbf{q})) \tag{5.54}$$

$$\mathcal{G}(\mathbf{p},\omega) \;=\; \frac{1}{\omega-\varepsilon(\mathbf{p})-\Sigma(\mathbf{p},\omega)}\,. \tag{5.55}$$

For the self-consistent Born approximation one uses the magnon dispersion of the form $\Omega(\mathbf{q}) = \sqrt{\Delta^2 + \mathrm{v}_s^2\,(1+\gamma(\mathbf{q})/4)}$ with $\gamma(\mathbf{q}) = 2\,(\cos(q_x)+\cos(q_y))$, which in the limit $\mathbf{q} \to \mathbf{Q}$ agrees with the form of Eq. (5.49). By iterating the Green's function according to Eq. (5.54) and Eq. (5.55) one obtains for the self-energy in terms of Feynman diagrams

$\Sigma(\mathbf{p},\omega) =$

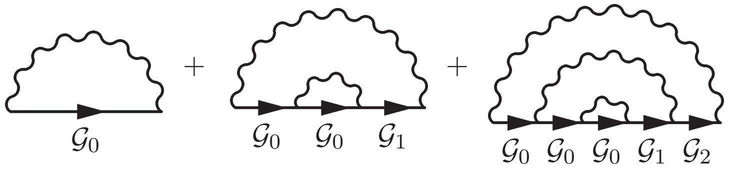
$\mathcal{G}_0$
$\mathcal{G}_0$ $\mathcal{G}_0$ $\mathcal{G}_1$
$\mathcal{G}_0$ $\mathcal{G}_0$ $\mathcal{G}_0$ $\mathcal{G}_1$ $\mathcal{G}_2$

$+ \ldots$ (5.56)

where $\mathcal{G}_i$ stands for the Green's function of the i-th iteration. This sum contains all non-crossing diagrams, which are also called *rainbow* diagrams due to their structure. Motivated by the work of Sushkov [89] only these diagrams should contribute to the hole self-energy. In the presented results the Green's function is iterated by the self-consistent equations in (5.54) and (5.55) up to the 15th order to ensure convergence [see Fig. 5.10(a)]. The spectrum of the hole is calculated via the imaginary part of the Green's function $\rho(\mathbf{p},\omega) = -\frac{1}{\pi}\,\mathfrak{Im}\,\mathcal{G}(\mathbf{p},\omega)$ in order to determine the resonances ξ_i.

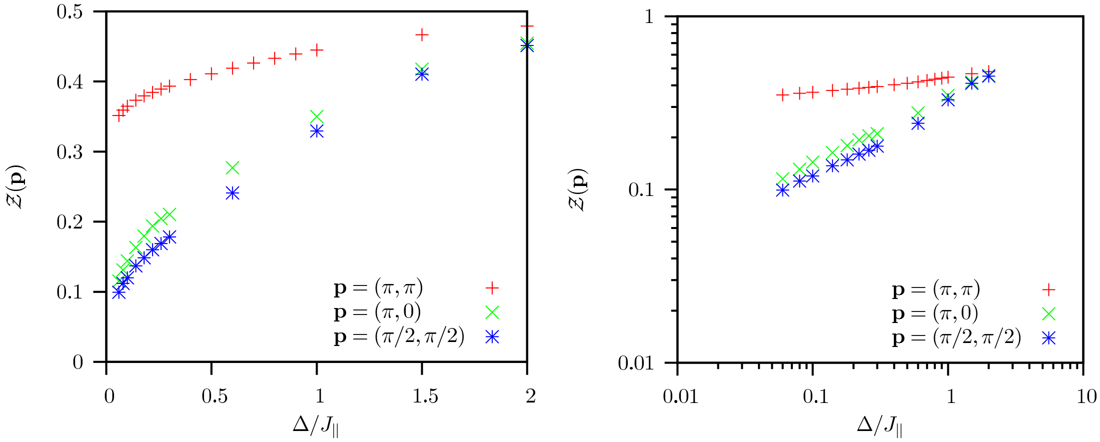

(a) SCB results (b) SCG results on a log-scale

Figure 5.11: Self-consistent Born approximation: QPR in the vicinity of the quantum critical point for selected hole momenta (a) in a linear plot and (b) in a double logarithmic plot. Δ corresponds to the spin gap.

Then the QPR is computed at the first pole of the spectrum by Eq. (5.44). Fig. 5.10(b) shows the QPR for $\mathbf{p} = (\pi, \pi)$ as a function of linear length L of the square lattice for different values of the spin gap Δ. The large-L limit is indicated by a line. Figs. 5.11 plot the quasiparticle weight as a function of the spin gap for hole momenta $\mathbf{p} = (\pi/2, \pi/2)$, $\mathbf{p} = (0, \pi)$ and $\mathbf{p} = (\pi, \pi)$. For hole momenta satisfying the condition given in Eq. (5.51), which for instance are $\mathbf{p} = (\pi/2, \pi/2)$ and $\mathbf{p} = (0, \pi)$, there is no energy denominator prohibiting the logarithmic divergence of the first order self-energy and the QPR shows an obvious decrease right up to a complete vanishing at the critical point. Furthermore, the data is consistent with $\mathcal{Z} \propto \sqrt{\Delta}$. The case $\mathbf{p} = (\pi, \pi)$ is more complicated since $\epsilon(\mathbf{p}) \neq \varepsilon(\mathbf{p}+\mathbf{Q})$. In first order, the self-energy remains bounded. The scattering of the hole on $\mathbf{q} = (\pi, \pi)$ magnons leads to the progressive formation of shadow bands as the critical point is approached such that at the critical point the relation $E^{(1)}(\mathbf{p}) = E^{(1)}(\mathbf{p} + \mathbf{Q})$ holds. This back-folding of the band can lead to the vanishing of the QPR when higher order terms are included. Although the SCB results show a decrease of the QPR in the vicinity of the critical point, they are not accurate enough to answer the question of the vanishing of the QPR at this wave vector.

5.4.2 QMC Approach

As shown in section 3.3 within the path integral QMC simulations for each fixed spin configuration one can compute the Green's function for a single hole. From the Green's function in imaginary time $\mathcal{G}_{\mathbf{p}}(\tau)$, it is easy to extract the quasiparticle residue.

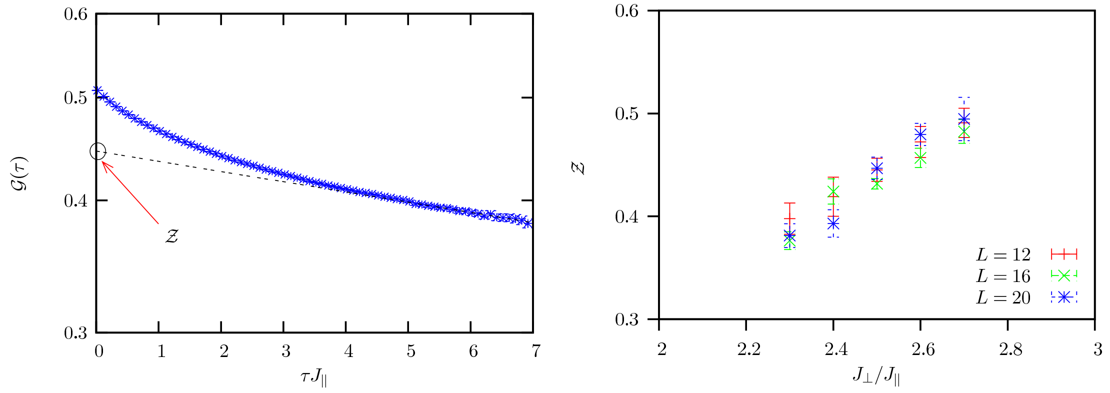

(a) Green's function for a static hole

(b) QPR for a atatic hole

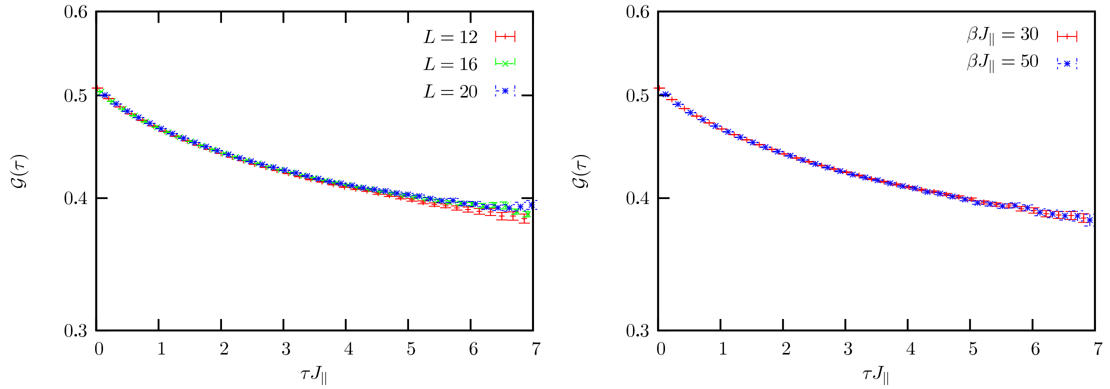

(c) Size scaling

(d) Temperature scaling

Figure 5.12: (a) Example of how to read off the quasiparticle residue from the asymptotic form of the single particle Green's function. In the limit $\tau \to \infty$ the Green's function is of the form given in Eq. (5.59). The presented data corresponds to a static hole at $J_{\perp}/J_{\|} = 2.5$ on a 12×12 lattice in the bilayer Heisenberg model ($\beta J_{\|} = 30.0$, $\Delta\tau J_{\|} = 0.02$). (b) Quasiparticle residue for a static hole in the BHM for different lattice sizes: $L = 12$ ($\beta J_{\|} = 30.0$), $L = 16$ ($\beta J_{\|} = 50.0$) and $L = 20$ ($\beta J_{\|} = 70.0$). (c,d) Green's function $\mathcal{G}(\tau)$ for a static hole at $J_{\perp}/J_{\|} = 2.5$ in the BHM. As apparent within the range $5.0 \leq \tau J_{\|} \leq 6.0$ no considerable size and temperature effects are observable ($\beta J_{\|} = 30.0$, $\Delta\tau J_{\|} = 0.02$).

According to Eq. (3.29) in the limit $T \to 0$ the momentum dependent Green's function $\mathcal{G}_{\mathbf{p}}(\tau)$ in the up-spin sector reads

$$\mathcal{G}_{\mathbf{p}}(\tau) = \langle \Psi_0^N | \hat{c}_{\mathbf{p}}^{\dagger}(\tau) \hat{c}_{\mathbf{p}}(0) | \psi_0^N \rangle \ , \tag{5.57}$$

where the spin indices are neglected. Here, $|\Psi_0^N\rangle$ stands for the ground state of the half-filled system where the upper index N denotes the particle number. $\hat{c}_{\mathbf{p}}^{\dagger}$ and $\hat{c}_{\mathbf{p}}$ create and annihilate an up-spin electron.

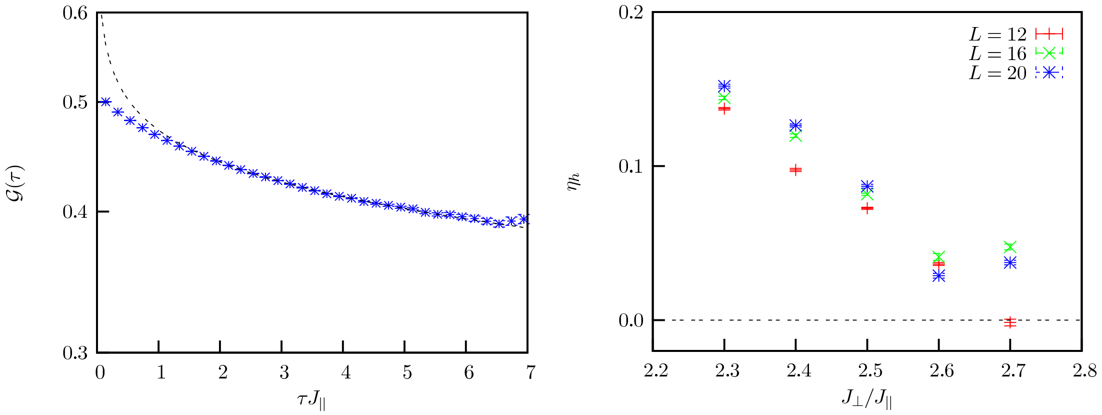

(a) Fit according to Ref. [90]

(b) η_h as a function of $J_\perp/J_\parallel$

Figure 5.13: (a) The Green's function ($J_\perp/J_\parallel = 2.5$, $L = 20$) for a static hole is fitted to the form given in Eq. (5.61). (b) The so-obtained results for η_h are plotted as a function of $J_\perp/J_\parallel$ for different lattice sizes. The error bars are potentially underestimated. The results should only give a qualitative impression. Temperature used: $\beta J_\parallel = 30.0$ for $L = 12$, $\beta J_\parallel = 50.0$ for $L = 16$ and $\beta J_\parallel = 70.0$ for $L = 20$.

The time evolution of the operators is given by $\hat{c}_{\mathbf{p}}(\tau) = e^{\hat{\mathcal{H}}\tau}\hat{c}_{\mathbf{p}}e^{-\hat{\mathcal{H}}\tau}$. From Eq. (5.57) it follows

$$\mathcal{G}_{\mathbf{p}}(\tau) = \sum_m |\langle\Psi_m^{N-1}|\hat{c}_{\mathbf{p}}|\Psi_0^N\rangle|^2 e^{-(E_m^{N-1}(\mathbf{p})-E_0^{N-1})\tau} e^{-E(\mathbf{p})\tau} \ , \tag{5.58}$$

where $E(\mathbf{p}) = E_0^{N-1}(\mathbf{p}) - E_0^N$ corresponds to the single hole dispersion relation. E_m^N is the energy of the eigenstate $|\Psi_m^N\rangle$. Since $E_m^{N-1} - E_0^{N-1} > 0$ for all $m \neq 0$ in the limit $\tau \to \infty$ the Green's function reduces to the asymptotic form

$$\mathcal{G}_{\mathbf{p}}(\tau) = |\langle\Psi_0^{N-1}|\hat{c}_{\mathbf{p}}|\Psi_0^N\rangle|^2 e^{-E(\mathbf{p})\tau} \ . \tag{5.59}$$

As apparent, the prefactor called *renormalization coefficient* [87]

$$\mathcal{Z}_{\mathbf{p}} = |\langle\Psi_0^{N-1}|\hat{c}_{\mathbf{p}}|\Psi_0^N\rangle|^2 \ , \tag{5.60}$$

is nothing but the quasiparticle residue. The analogy between the definitions (5.44) and (5.60) is shown in Refs. [7, 88], for example. Hence from the asymptotic form of the single particle Green's function, one can read off the quasiparticle residue. An example how to determine the QPR from the imaginary time Green's function is shown in Fig. 5.12(a). In the following attention is first given to the static hole in the BHM for which the QMC data is of higher quality than for the dynamic hole. Fig. 5.12 plots the Green's function as a function of lattice size and for different temperatures at $J_\perp/J_\parallel = 2.5$. Within the considered range of imaginary times no size and temperature effects are apparent.

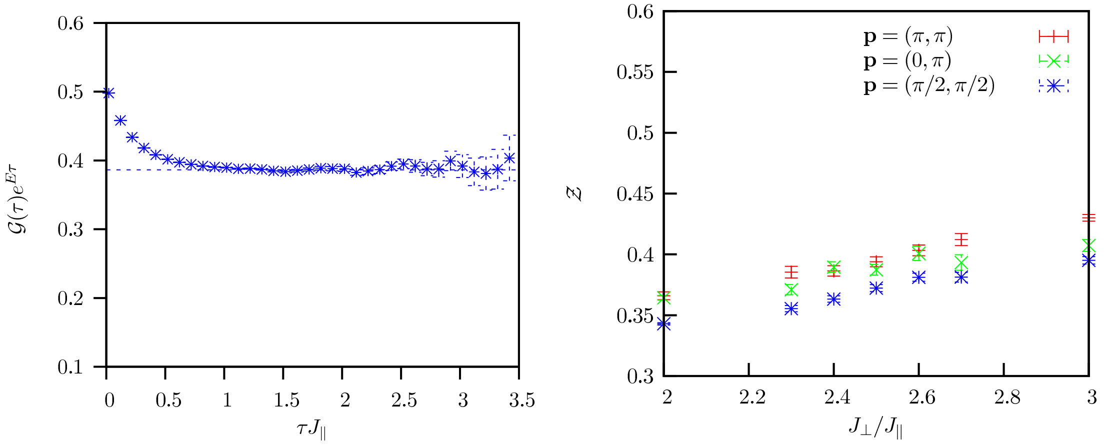

(a) Green's function in BHM

(b) QPR for dynamical hole in the BHM

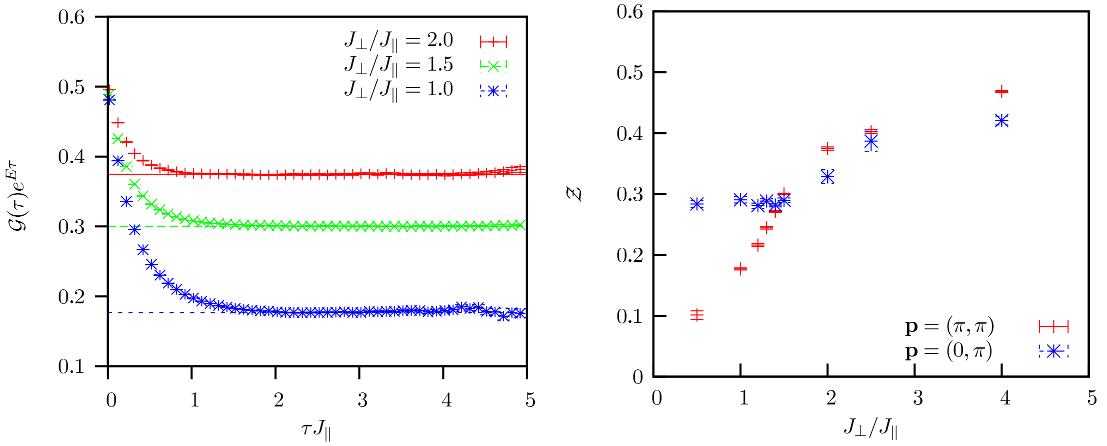

(c) Green's function in KNM

(d) QPR for dynamical hole in the KNM

Figure 5.14: (a) Green's function of a dynamical hole ($\mathbf{p} = (\pi, \pi)$) at $J_\perp/J_\parallel = 2.4$ on a 12×12 lattice in the BHM. (b) Quasiparticle residue in the vicinity of the quantum critical point for various couplings and different momenta. (c) Green's function of a dynamical hole ($\mathbf{p} = (\pi, \pi)$) on a 12×12 lattice in the Kondo necklace model. (d) Quasiparticle residue in the vicinity of the quantum critical point in the KNM. ($L = 12$, $\beta J_\parallel = 30.0$, $\Delta\tau = 0.02$)

The tail ($5.0 \leq \tau J_\parallel \leq 6.0$) of the Green's function is fitted to the form $\mathcal{G}(\tau) = \mathcal{Z}e^{-E\tau}$. The so-obtained value of $\mathcal{Z}$ is plotted for values of $J_\perp/J_\parallel$ across the magnetic quantum phase transition [see Fig. 5.12(b)]. As apparent no sign of the vanishing of the QPR is observable as one crosses the quantum critical point. The QMC data allows a different interpretation. Following the work of Sachdev *et al.* [90] one has to fit the imaginary time Green's function to the form

$$\mathcal{G}(\tau) \propto \tau^{-\eta_h} \exp\left(-\tau E\right) \qquad (5.61)$$

in the range $2.0 < \tau J_\parallel < 6.0$ [see Fig. 5.13(a)]. Clearly, if $\eta_h > 0$ then the QPR vanishes.

The results for η_h are plotted in Fig. 5.13(b). At $J_\perp/J_\parallel = 2.5$ the result $\eta_h = 0.08(7)$ compares very well to that quoted in Ref. [90], $\eta_h = 0.087 \pm 0.040$. The fact that the result of Ref. [90] is obtained on a 64×64 lattice and the result given in this work on 20×20 confirms that for the considered imaginary time range, size effects are nearly absent. Given the above interpretation of the data, Fig. 5.13(b) suggests that the QPR of a static hole vanishes for all $J_\perp/J_\parallel \leq \left(J_\perp/J_\parallel\right)_c \simeq 2.5$. The choice of the fitting function reflects different ordering of the limits $\tau \rightarrow \infty$ and $L \rightarrow \infty$. On any finite size lattice the QPR is finite and hence it is appropriate to fit the tail of the Green's function to the form $\mathcal{Z}(L)e^{-\tau E}$ to obtain a size dependent QPR, and subsequently take the thermodynamic limit. This strategy has been used successfully to show that the QPR of a doped mobile hole in a one dimensional Heisenberg chain vanishes [71]. On the other hand, the choice of Eq. (5.61) for fitting the data implies that one first takes the thermodynamic limit. Only in this limit, can the asymptotic form of the Green's function follow Eq. (5.61) with $\eta_h \neq 0$. The fact that both procedures yield different results sheds doubt on the small imaginary time range used to extract the quasiparticle residue. In particular, using data from $\tau J_\parallel = 2.0$ onwards implies that one is looking at a frequency window around the lowest excitation of the order $\omega/J \simeq 0.5$. Given this, it is hard to resolve the difference between a dense spectrum and a well defined low-lying quasiparticle pole and a branch cut.

Finally, the data for a mobile hole in the BHM and KNM [see Fig. 5.14] are presented. One has to note that in the presented calculations the motion of the hole is restricted to a single plane. The data for the QPR in the above mentioned figures stem from fitting the tail of the Green's function to the form $\mathcal{Z}e^{-E\tau}$. The fit to the form of Eq. (5.61) yields values of η_h which within the error bars are not distinguishable from zero.

The Spiral Staircase Heisenberg Model

6

The Haldane conjecture [24] proposed more than 20 years ago states that the properties of $SU(2)$ symmetric antiferromagnetic (AF) spin-S Heisenberg chains are different for integer and half-integer spins. The excitations of integer spin chains are gapped, whereas for half-integer spin chains there is no gap. In this chapter the spiral staircase Heisenberg (SSH) model is studied. It interpolates between a spin-1/2 Heisenberg chain and an effective spin-1 chain and thus allows to analyze the crossover from a gapped Haldane phase to an ungapped phase. The SSH model is described by the following Heisenberg Hamiltonian:

$$\hat{\mathcal{H}} \;=\; J_{\parallel} \sum_i \left(\hat{\mathbf{S}}_{1,i} \cdot \hat{\mathbf{S}}_{1,i+1} + \cos^2(\theta/2)\, \hat{\mathbf{S}}_{2,i} \cdot \hat{\mathbf{S}}_{2,i+1} \right) + J_{\perp} \sum_i \hat{\mathbf{S}}_{1,i} \cdot \hat{\mathbf{S}}_{2,i} \;. \tag{6.1}$$

$\hat{\mathbf{S}}_{\alpha,i}$ is a spin operator acting on the spin degree of freedom on leg α at site i. The spin along the leg are coupled antiferromagnetically, $J_{\parallel} > 0$, whereas the coupling on a rung is assumed to be ferromagnetic (FM) in order to form effective spin-1 degrees of freedom in the large coupling region $|J_{\perp}| \gg J_{\parallel}$. The SSH model also allows to study the coupling of two inequivalent spin-1/2 chains, since the AF coupling on the second leg can be tuned by the angle θ. Thus, the SSH model can be understood as a continuous twist deformation of an isotropic 2-leg ladder by an angle θ. A sketch of the model is given in Fig. 6.1.

It is convenient to reformulate the model in Eq. (6.1) in terms of new variables,

$$\hat{\mathbf{S}}_i = \hat{\mathbf{S}}_{1,i} + \hat{\mathbf{S}}_{2,i} \quad \text{and} \quad \hat{\mathbf{R}}_i = \hat{\mathbf{S}}_{1,i} - \hat{\mathbf{S}}_{2,i} \;, \tag{6.2}$$

which satisfy the following parity properties:

$$\hat{\mathcal{P}} \hat{\mathbf{S}}_i \hat{\mathcal{P}} = \hat{\mathbf{S}}_i \quad \text{and} \quad \hat{\mathcal{P}} \hat{\mathbf{R}}_i \hat{\mathcal{P}} = -\hat{\mathbf{R}}_i \;. \tag{6.3}$$

Here, $\hat{\mathcal{P}}$ is the parity operator which interchanges the leg labeling 1 ↔ 2. These symmetries become relevant later in subsection 6.3.1 when discussing the spin excitation spectra. The

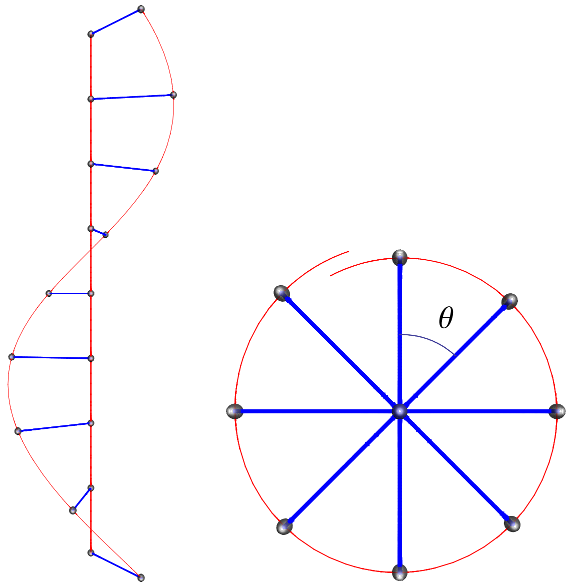

(a) Side view (b) View from the top

Figure 6.1: Sketch of spiral staircase Heisenberg model. For $\theta = 0$ the model corresponds to the common antiferromagnetically coupled (red) spin-1/2 Heisenberg ladder with FM rung coupling (blue). The case $\theta = \pi$ represents the 1D $SU(2)$ symmetric Kondo necklace model.

Hamiltonian of Eq. (6.1) now writes

$$\begin{aligned}\hat{\mathcal{H}} &= \frac{J_\parallel}{4}\sum_i \left(1+\cos^2(\theta/2)\right)\left(\hat{\mathbf{S}}_i\cdot\hat{\mathbf{S}}_{i+1}+\hat{\mathbf{R}}_i\cdot\hat{\mathbf{R}}_{i+1}\right)\\ &+ \frac{J_\perp}{4}\sum_i \sin^2(\theta/2)\left(\hat{\mathbf{S}}_i\cdot\hat{\mathbf{R}}_{i+1}+\hat{\mathbf{R}}_i\cdot\hat{\mathbf{S}}_{i+1}\right)\\ &+ \frac{J_\perp}{4}\sum_i \left(\hat{\mathbf{S}}_i^2-\hat{\mathbf{R}}_i^2\right) \ . \end{aligned} \tag{6.4}$$

For $\theta = 0$ parity symmetry holds, whereas in the twisted model ($\theta \neq 0$) the parity symmetry is broken: $\left[\hat{\mathcal{P}}, \hat{\mathcal{H}}\right] \neq 0$. However, the set of operators $\hat{\mathbf{S}}_i$ and $\hat{\mathbf{R}}_i$ fully defines the o_4 algebra through the following commutation rules:

$$\left[\hat{S}_i^\alpha, \hat{S}_j^\beta\right] = \mathrm{i}\,\delta_{ij}\epsilon_{\alpha\beta\gamma}\hat{S}_i^\gamma \ , \ \left[\hat{R}_i^\alpha, \hat{R}_j^\beta\right] = \mathrm{i}\,\delta_{ij}\epsilon_{\alpha\beta\gamma}\hat{S}_i^\gamma \text{ and } \left[\hat{R}_i^\alpha, \hat{S}_j^\beta\right] = \mathrm{i}\,\delta_{ij}\epsilon_{\alpha\beta\gamma}\hat{R}_i^\gamma \ . \tag{6.5}$$

where $\epsilon_{\alpha\beta\gamma}$ is the totally antisymmetric Levi-Civita tensor and the Casimir operators are given by $\hat{\mathbf{S}}_i^2 + \hat{\mathbf{R}}_i^2$ and $(\hat{\mathbf{S}}_i \cdot \hat{\mathbf{R}}_i) = 0$. This work does not go into the details of the symmetry properties of this model for which the reader is referred to Refs. [30, 31]. However, it is obvious that in the large coupling region the formation of singlets on a rung becomes rare, $\langle \hat{\mathbf{R}}_i \rangle \simeq 0$, and the model maps to the following effective Hamiltonian:

$$\hat{\mathcal{H}}_{\text{eff}} = J_{\text{eff}} \sum_i \hat{\mathbf{S}}_i \cdot \hat{\mathbf{S}}_{i+1} \ , \tag{6.6}$$

where the effective coupling is given by $J_{\text{eff}} = \frac{J_\parallel}{4}\left(1+\cos^2(\theta/2)\right)$. The analysis of the SSH model starts with a Jordan-Wigner mean field calculation of the two extreme cases [91],

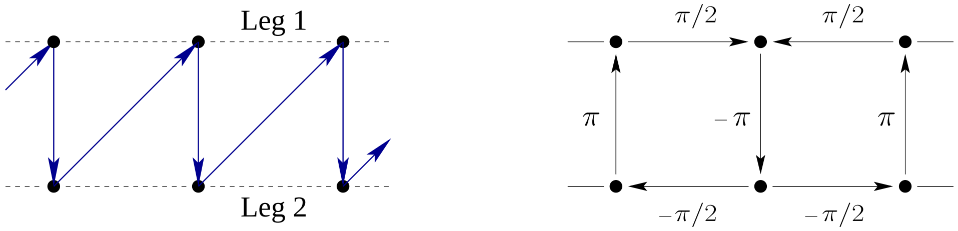

(a) Jordan-Wigner transformation

(b) Gauge transformation

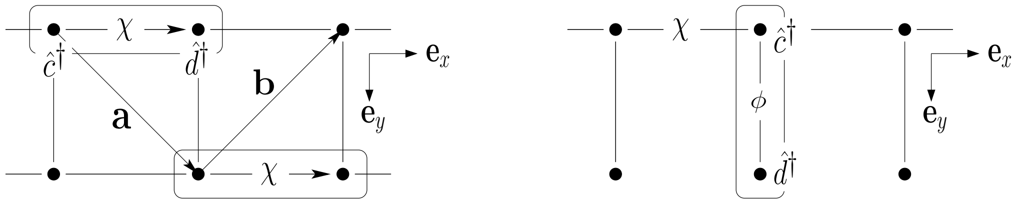

(c) Ladder system

(d) Kondo necklace

Figure 6.2: (a) Zigzag path used for the Jordan-Wigner transformation given in Eq. (6.7). (b) Gauge transformation applied in the ladder system ($\theta = \pi$). (c) Unit cell (box), basis vectors **a** and **b** and flux χ in the mean field ansatz for the ladder system. (d) Unit cell (box) in mean field ansatz for the $SU(2)$ symmetric Kondo necklace model.

the one dimensional (1D) Kondo necklace ($\theta = \pi$), where the coupling along the second leg is missing, and the common 2-leg ladder system ($\theta = 0$).

6.1 Jordan-Wigner Mean Field Approach

The definition of the Jordan-Wigner transformation for the ladder topology relies on the choice of a path labeling the different sites. With the choice shown in Fig. 6.2(a) it reads:

$$\begin{aligned}
\hat{S}^z_{1,i} &= \hat{n}_{1,i} - \tfrac{1}{2} \qquad \hat{S}^+_{1,i} = \hat{c}^\dagger_{1,i} \exp\Big(-\mathrm{i}\,\pi \sum_{l=1}^{i-1} (\hat{n}_{1,l} + \hat{n}_{2,l}) \Big) \\
\hat{S}^z_{2,i} &= \hat{n}_{2,i} - \tfrac{1}{2} \qquad \hat{S}^+_{2,i} = \hat{c}^\dagger_{2,i} \exp\Big(-\mathrm{i}\,\pi \Big(\sum_{l=1}^{i} \hat{n}_{1,l} + \sum_{l=1}^{i-1} \hat{n}_{2,l} \Big) \Big)
\end{aligned} \tag{6.7}$$

where $\hat{n}_{\alpha,i} = \hat{c}^\dagger_{\alpha,i}\hat{c}_{\alpha,i}$ is the occupation number operator at site i with leg index $\alpha = 1, 2$. $\hat{c}^\dagger_{\alpha,i}$ and $\hat{c}_{\alpha,i}$ are spinless fermionic creation and annihilation operators which satisfy the anticommutation rule

$$\left\{ \hat{c}_{\alpha,i}, \hat{c}^\dagger_{\beta,j} \right\} = \delta_{ij}\delta_{\alpha\beta} \ . \tag{6.8}$$

In the ladder topology ($\theta = 0$) a spinless fermion can circulate around a plaquette thereby allowing for a π-flux phase as solution of the mean field equations. This leads, as demonstrated below, to a spin gap $\Delta \propto |J_\perp|$. Such a solution is not possible in the Kondo necklace system since at $\theta = \pi$ one leg of the ladder is removed. In this case, the mean field solution yields a band structure stemming from the hybridization of a flat band, accounting for the dangling spins, and a cosine band of width set by $J_\parallel$ accounting for the spin dynamics in the chain. Since the hybridization matrix element is set by $J_\perp$, one obtains an (indirect) spin gap $\Delta \propto |J_\perp|^2$. The mean field calculations are presented in detail in the following two subsections.

6.1.1 Ladder System

The calculations presented here follow Ref. [92]. After application of the Jordan-Wigner transformation the Heisenberg Hamiltonian of Eq. (6.4) can be rewritten as

$$
\begin{aligned}
\hat{\mathcal{H}} \;=\; & -\frac{J_\perp}{2}\sum_{i=1}^{L}\left\{\hat{D}_i^{\dagger(\perp)}\hat{D}_i^{(\perp)} + \hat{D}_i^{(\perp)}\hat{D}_i^{\dagger(\perp)}\right\} + \frac{J_\perp}{2}\sum_{i=1}^{L}\left\{\hat{D}_i^{\dagger(\perp)} + \hat{D}_i^{(\perp)}\right\} \\
& -\frac{J_\parallel}{2}\sum_{i=1}^{L}\sum_{\alpha=1}^{2}\left\{\hat{D}_{i,i+1}^{\dagger(\alpha)}\hat{D}_{i,i+1}^{(\alpha)} + \hat{D}_{i,i+1}^{(\alpha)}\hat{D}_{i,i+1}^{\dagger(\alpha)}\right\} \\
& +\frac{J_\parallel}{2}\sum_{i=1}^{L}\left\{\hat{D}_{i,i+1}^{\dagger(1)}e^{\mathrm{i}\,\pi\hat{n}_{2,i}} + \hat{D}_{i,i+1}^{\dagger(2)}e^{\mathrm{i}\,\pi\hat{n}_{1,i+1}} + \mathrm{H.\,c.}\right\}.
\end{aligned}
\tag{6.9}
$$

Here, for the sake of clarity the following abbreviated notations are used: $\hat{D}_i^{\dagger(\perp)} = \hat{c}_{1,i}^{\dagger}\hat{c}_{2,i}$ and $\hat{D}_{i,j}^{\dagger(\alpha)} = \hat{c}_{\alpha,i}^{\dagger}\hat{c}_{\alpha,j}$. In the calculation below, the mean field solution is restricted to a phase with zero magnetization, $\langle S_{\alpha,i}^{z}\rangle = 0$, such that $\langle \hat{n}_{\alpha,i}\rangle = \frac{1}{2}$. To proceed further $\hat{n}_{i,\alpha}$ is replaced by its mean value. Although this simplification cannot be rigorously justified [93] and more elaborate treatments are possible in a Jordan-Wigner approach [94], it is shown below that it qualitatively reproduces the results available by more sophisticated methods. For the further calculation a gauge transformation as sketched in Fig. 6.2(b) and given by

$$
\begin{array}{lclclcl}
\hat{D}_{2n-1,2n}^{\dagger(1)} & \rightarrow & \hat{D}_{2n-1,2n}^{\dagger(1)}e^{-\mathrm{i}\,\pi/2} & \quad & \hat{D}_{2n,2n+1}^{\dagger(1)} & \rightarrow & \hat{D}_{2n,2n+1}^{\dagger(1)}e^{\mathrm{i}\,\pi/2} \\
\hat{D}_{2n-1,2n}^{\dagger(2)} & \rightarrow & \hat{D}_{2n-1,2n}^{\dagger(2)}e^{\mathrm{i}\,\pi/2} & & \hat{D}_{2n,2n+1}^{\dagger(2)} & \rightarrow & \hat{D}_{2n,2n+1}^{\dagger(2)}e^{-\mathrm{i}\,\pi/2} \\
\hat{D}_{2n}^{\dagger(\perp)} & \rightarrow & \hat{D}_{2n}^{\dagger(\perp)}e^{\mathrm{i}\,\pi} & & \hat{D}_{2n+1}^{\dagger(\perp)} & \rightarrow & \hat{D}_{2n+1}^{\dagger(\perp)}e^{\mathrm{i}\,\pi}
\end{array}
\tag{6.10}
$$

is applied. The Hamiltonian then reads

$$\begin{aligned}
\hat{\mathcal{H}} &= -\frac{J_\perp}{2}\sum_{n=1}^{L/2}\left\{\hat{D}^{\dagger(\perp)}_{2n-1}\hat{D}^{(\perp)}_{2n-1}+\hat{D}^{\dagger(\perp)}_{2n}\hat{D}^{(\perp)}_{2n}+\mathrm{H.\,c.}\right\}\\
&\quad -\frac{J_\perp}{2}\sum_{n=1}^{L/2}\left\{\hat{D}^{\dagger(\perp)}_{2n-1}+\hat{D}^{\dagger(\perp)}_{2n}+\mathrm{H.\,c.}\right\}\\
&\quad -\frac{J_\parallel}{2}\sum_{\alpha=1}^{2}\sum_{n=1}^{L/2}\left\{\hat{D}^{\dagger(\alpha)}_{2n-1,2n}\hat{D}^{(\alpha)}_{2n-1,2n}+\hat{D}^{\dagger(\alpha)}_{2n,2n+1}\hat{D}^{(\alpha)}_{2n,2n+1}+\mathrm{H.\,c.}\right\}\\
&\quad -\frac{J_\parallel}{2}\sum_{n=1}^{L/2}\left\{-\hat{D}^{\dagger(1)}_{2n-1,2n}+\hat{D}^{\dagger(1)}_{2n,2n+1}+\hat{D}^{\dagger(2)}_{2n-1,2n}-\hat{D}^{\dagger(2)}_{2n,2n+1}+\mathrm{H.\,c.}\right\}.
\end{aligned}\tag{6.11}$$

As a mean field ansatz one may set

$$\begin{aligned}
\langle\hat{D}^{\dagger(1)}_{2n-1,2n}\rangle &= \langle\hat{D}^{\dagger(2)}_{2n,2n+1}\rangle = Qe^{i\chi}\\
\langle\hat{D}^{\dagger(2)}_{2n-1,2n}\rangle &= \langle\hat{D}^{\dagger(1)}_{2n,2n+1}\rangle = Q\\
\langle\hat{D}^{\dagger(\perp)}_{2n-1}\rangle &= \langle\hat{D}^{\dagger(\perp)}_{2n}\rangle = P\,.
\end{aligned}\tag{6.12}$$

where the choice of the phase is depicted in Fig. 6.2(c). Here, P and Q are positive real numbers. To further exploit translation invariance, a unit cell $\mathbf{x}$ containing two orbitals with corresponding fermion operators, $\hat{c}^\dagger_{\mathbf{x}}$ and $\hat{d}^\dagger_{\mathbf{x}}$, and lattice vectors $\mathbf{a}$ and $\mathbf{b}$ [see Fig. 6.2(c)] is defined:

$$\begin{array}{lll}
\hat{D}^{\dagger(\perp)}_{2n-1}=\hat{c}^\dagger_{\mathbf{x}}\hat{d}_{\mathbf{x}-\mathbf{b}} & \hat{D}^{\dagger(1)}_{2n-1,2n}=\hat{c}^\dagger_{\mathbf{x}}\hat{d}_{\mathbf{x}} & \hat{D}^{\dagger(2)}_{2n-1,2n}=\hat{d}^\dagger_{\mathbf{x}}\hat{c}_{\mathbf{x}+\mathbf{a}+\mathbf{b}}\\
\hat{D}^{\dagger(\perp)}_{2n}=\hat{d}^\dagger_{\mathbf{x}}\hat{c}_{\mathbf{x}+\mathbf{a}} & \hat{D}^{\dagger(1)}_{2n,2n+1}=\hat{d}^\dagger_{\mathbf{x}}\hat{c}_{\mathbf{x}+\mathbf{a}+\mathbf{b}} & \hat{D}^{\dagger(2)}_{2n,2n+1}=\hat{c}^\dagger_{\mathbf{x}}\hat{d}_{\mathbf{x}}\,.
\end{array}\tag{6.13}$$

Assuming periodic boundary conditions in the y-direction (amounting to a double counting of $J_\perp$), the mean field Hamiltonian can conveniently be written as

$$\begin{aligned}
\hat{\mathcal{H}} &= -\frac{J_\perp}{2}\sum_{\mathbf{x}}A\left\{\hat{c}^\dagger_{\mathbf{x}}\hat{d}_{\mathbf{x}-\mathbf{b}}+\hat{c}^\dagger_{\mathbf{x}+\mathbf{a}}\hat{d}_{\mathbf{x}}+\mathrm{H.\,c.}\right\}\\
&\quad +J_\parallel\sum_{\mathbf{x}}\left\{B_1\hat{c}^\dagger_{\mathbf{x}}\hat{d}_{\mathbf{x}}+B_2\hat{c}^\dagger_{\mathbf{x}+\mathbf{a}+\mathbf{b}}\hat{d}_{\mathbf{x}}+\mathrm{H.\,c.}\right\}+2J_\perp LP^2+4J_\parallel LQ^2
\end{aligned}\tag{6.14}$$

with $A=(1/2+P)$, $B_1=(-1/2-Q)$, $B_2=(1/2-Qe^{-\mathrm{i}\chi})$. After application of a Fourier transformation one arrives at the non-diagonal Hamiltonian of the following form:

$$\hat{\mathcal{H}}=\sum_{\mathbf{k}}\left(\,\hat{c}^\dagger_{\mathbf{k}}\,,\,\hat{d}^\dagger_{\mathbf{k}}\,\right)\begin{pmatrix}0 & \varepsilon(\mathbf{k})\\ \overline{\varepsilon(\mathbf{k})} & 0\end{pmatrix}\begin{pmatrix}\hat{c}_{\mathbf{k}}\\ \hat{d}_{\mathbf{k}}\end{pmatrix}+K\tag{6.15}$$

with $K=2J_\perp LP^2+4J_\parallel LQ^2$. $\mathbf{k}=(k_x,k_y)^\mathsf{T}$ is the wave vector and k_y is restricted to the values 0 and π. The Hamilton matrix elements are given by

$$\varepsilon(\mathbf{k})=-\frac{J_\perp}{2}A\left(e^{\mathrm{i}\,\mathbf{k}\cdot\mathbf{a}}+e^{\mathrm{i}\,\mathbf{k}\cdot\mathbf{b}}\right)+J_\parallel B_1+J_\parallel B_2e^{\mathrm{i}\,\mathbf{k}\cdot(\mathbf{a}+\mathbf{b})}\,.\tag{6.16}$$

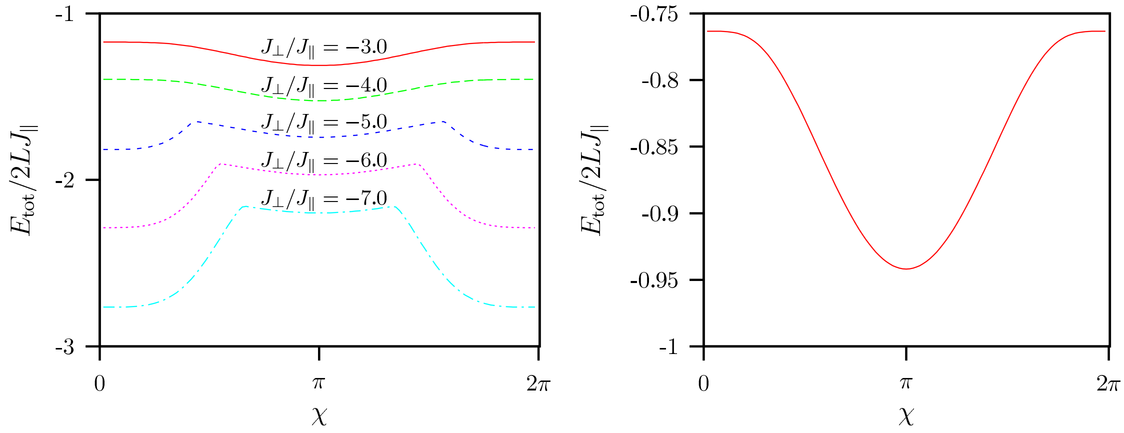

(a) Energy for different values of χ

(b) $J_\perp/J_\| = -1.0$

Figure 6.3: (a) Energy per site in respect to the mean field parameter χ for different couplings $J_\perp/J_\|$. The minimum of the energy changes from $\chi = \pi$ to $\chi = 0$ around $J_\perp/J_\| \sim 5$. (b) In the weak coupling region ($J_\perp/J_\| = -1.0$) the minimum for the energy is found at $\chi = \pi$.

The Hamiltonian is diagonalized by the transformation $\hat{\alpha}^\dagger_{\mathbf{k},\pm} = (\hat{c}^\dagger_{\mathbf{k}} \pm \hat{d}^\dagger_{\mathbf{k}})/\sqrt{2}$:

$$\hat{\mathcal{H}} = \sum_{\mathbf{k}} \sum_{\xi=\pm} E_\xi(\mathbf{k}) \hat{\alpha}^\dagger_{\mathbf{k},\xi} \hat{\alpha}_{\mathbf{k},\xi} + K \tag{6.17}$$

with $E_\pm(\mathbf{k}) = \pm\sqrt{|\varepsilon(\mathbf{k})|^2}$. For $|\varepsilon(\mathbf{k})|^2$ one finds

$$\begin{aligned} |\varepsilon(\boldsymbol{k})|^2 \;=\; & \frac{J_\perp^2}{2} A^2 \left(1+\cos(2k_y)\right) + 2J_\|^2 B^2 \left(1-\cos(2k_x)\right) - J_\|^2 \left(1+\cos(\chi)\right) \\ & + J_\perp J_\| AQ \left(1+\cos(\chi)\right) \left(\cos(k_x+k_y)+\cos(k_x-k_y)\right) \\ & - J_\perp J_\| AQ \sin(\chi) \left(\sin(k_x+k_y)+\sin(k_x-k_y)\right) \\ & + 2J_\|^2 BQ \left(1+\cos(\chi)\right)\cos(2k_x) - 2J_\|^2 BQ \sin(\chi)\sin(2k_x) \end{aligned} \tag{6.18}$$

with $A = (1/2 + P)$, $B = (1/2 + Q)$. One has to note that $\mathbf{k}\cdot(\mathbf{a}+\mathbf{b}) = 2k_x$ and $\mathbf{k}\cdot(\mathbf{a}-\mathbf{b}) = 2k_y$. The mean field parameters P, Q and χ are determined self-consistently by solving the following saddle point equations:

$$\left\langle \frac{\partial \hat{\mathcal{H}}}{\partial P} \right\rangle = 0 \quad , \quad \left\langle \frac{\partial \hat{\mathcal{H}}}{\partial Q} \right\rangle = 0 \quad \text{and} \quad \left\langle \frac{\partial \hat{\mathcal{H}}}{\partial \chi} \right\rangle = 0 \; . \tag{6.19}$$

In the range of couplings considered, one finds that the total energy E_{tot} is minimized for $\chi = \pi$, thereby favoring a π-flux phase. The total energy per site depending on the mean field parameter χ is explicitly shown in Fig. 6.3(a). For the π-flux, the dispersion relation now takes the simple form

$$E_\pm(\mathbf{k}) = \pm\sqrt{J_\perp^2 A^2 + 4J_\|^2 B^2 \sin^2(k_x)} \tag{6.20}$$

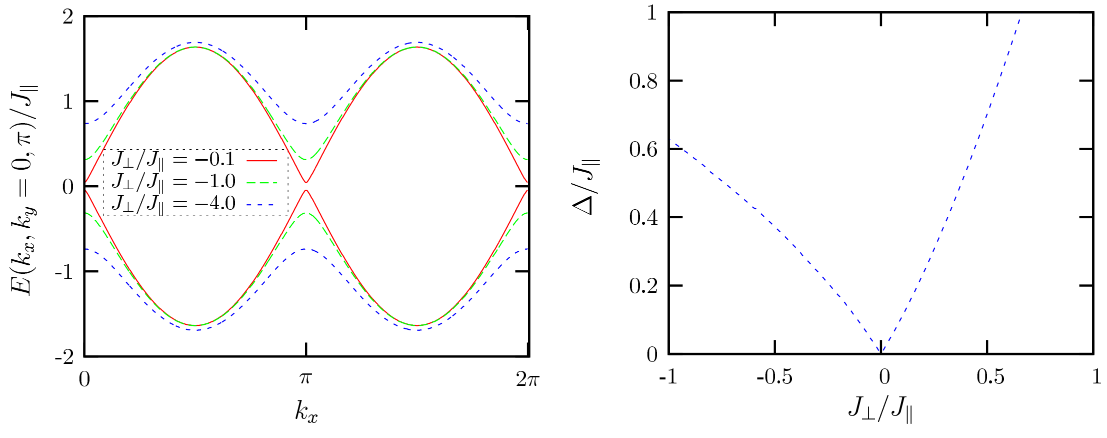

(a) Dispersion relation

(b) Spin gap

Figure 6.4: (a) Results of the ladder system for the spectra of the spinless fermions for different couplings within the Jordan-Wigner mean field approach for flux phase $\chi = \pi$. (b) Results for the spin gap Δ as a function of coupling $J_\perp/J_\parallel$. In the ladder system the gap opens linearly.

and the self-consistent equations obtained from Eq. (6.19) reduce to

$$Q = \frac{1}{2L}\sum_{\mathbf{k}} \frac{J_\parallel(2Q+1)\sin^2(k_x)}{2E_+(\mathbf{k})} \tag{6.21}$$

$$P = \frac{1}{2L}\sum_{\mathbf{k}} \frac{J_\perp(2P+1)}{4E_+(\mathbf{k})} \ . \tag{6.22}$$

Solving these equations numerically, one obtains the dispersion relation for various values of $J_\perp/J_\parallel$ as depicted in Fig. 6.4(a). In the spinless fermion language, one is considering the half-filled case or equivalently the zero magnetization case in terms of spins. As apparent, a particle-hole gap emerges at finite values of $|J_\perp|/J_\parallel \neq 0$. Within the mean field approximation developed here, the spin gap is given by

$$\Delta = |J_\perp\,(1+2P)| \ . \tag{6.23}$$

The spin gap is plotted in Fig. 6.3(b) for both, FM ($J_\perp > 0$) and AF ($J_\perp < 0$) rungs couplings. To extract the asymptotic behavior at small $J_\perp$, the data is fitted to a polynomial form: $\alpha J_\perp + \beta J_\perp^2 + \cdots$. The numerical results are consistent with $\alpha \neq 0$ irrespective of the sign of $J_\perp$ thereby suggesting a gap

$$\Delta \propto |J_\perp| \tag{6.24}$$

at low $|J_\perp|$. Hence, the simple mean field approach is consistent (up to logarithmic corrections) with bosonization [35] and quantum Monte Carlo simulations [95].

6.1.2 1D Kondo Necklace

Starting from the ladder system in Eq. (6.9), the mean field calculations for the Kondo necklace system follow by replacing $D^{\dagger(2)}$ with zero:

$$\begin{aligned}
\hat{\mathcal{H}} &= -\frac{J_\perp}{2}\sum_{i=1}^{L}\left\{\hat{D}_i^{\dagger(\perp)}\hat{D}_i^{(\perp)}+\hat{D}_i^{(\perp)}\hat{D}_i^{\dagger(\perp)}\right\}+\frac{J_\perp}{2}\sum_{i=1}^{L}\left\{\hat{D}_i^{\dagger(\perp)}+\hat{D}_i^{(\perp)}\right\}\\
&\quad -\frac{J_\parallel}{2}\sum_{i=1}^{L}\left\{\hat{D}_{i,i+1}^{\dagger(1)}\hat{D}_{i,i+1}^{(1)}+\hat{D}_{i,i+1}^{(1)}\hat{D}_{i,i+1}^{\dagger(1)}\right\}\\
&\quad +\frac{J_\parallel}{2}\sum_{i=1}^{L}\left\{\hat{D}_{i,i+1}^{\dagger(1)}\exp(\mathrm{i}\,\pi\hat{n}_{2,i})+\hat{D}_{i,i+1}^{(1)}\exp(-\mathrm{i}\,\pi\hat{n}_{2,i})\right\}\ . \qquad (6.25)
\end{aligned}$$

To proceed the following mean field ansatz is taken:

$$\langle D_i^{\dagger(\perp)}\rangle = Pe^{\mathrm{i}\,\phi}\ ,\quad \langle D_{i,j}^{\dagger(1)}\rangle = Qe^{\mathrm{i}\,\chi}\quad \text{and}\quad \langle\hat{n}_{\alpha,i}\rangle=\frac{1}{2}\ , \qquad (6.26)$$

where again P and Q are real and positive. With the unit cell defined in Fig. 6.2(d) and the corresponding spinless fermion operators, $c_i^\dagger$ and $d_i^\dagger$, for the two orbitals within the unit cell, the mean field Hamiltonian reads

$$\hat{\mathcal{H}} = J_\perp\sum_{i=1}^{L}\left\{\tilde{A}\hat{c}_i^\dagger\hat{d}_i+\mathrm{H.\,c.}\right\}+J_\parallel\sum_{i=1}^{L}\left\{\tilde{B}\hat{c}_i^\dagger\hat{c}_{i+1}+\mathrm{H.\,c.}\right\}+J_\perp LP^2+J_\parallel LQ^2\ .$$

Here, $\tilde{A}=\left(\frac{1}{2}-Pe^{-\mathrm{i}\,\phi}\right)$ and $\tilde{B}=\left(\frac{\mathrm{i}}{2}-Qe^{-\mathrm{i}\,\chi}\right)$. After applying a Fourier transformation the Hamiltonian takes the following non-diagonal form:

$$\hat{\mathcal{H}}=\sum_k\left(\ \hat{c}_k^\dagger\,,\,\hat{d}_k^\dagger\ \right)\begin{pmatrix}\omega(k) & \varepsilon\\ \overline{\varepsilon} & 0\end{pmatrix}\begin{pmatrix}\hat{c}_k\\ \hat{d}_k\end{pmatrix}+K \qquad (6.27)$$

with $K=J_\perp LP^2+J_\parallel LQ^2$. The Hamilton matrix elements are determined by

$$\begin{aligned}
\omega(k) &= J_\parallel\left(\sin(k)-2Q\cos(k+\chi)\right)\quad \text{and}\\
\varepsilon &= J_\perp\left(\tfrac{1}{2}-Pe^{-\mathrm{i}\,\phi}\right)\ . \qquad (6.28)
\end{aligned}$$

Diagonalization of the Hamiltonian finally results in a hybridized band structure:

$$E_\pm(k)=\frac{\omega(k)}{2}\pm\sqrt{\left(\frac{\omega(k)}{2}\right)^2+|\varepsilon|^2}\ . \qquad (6.29)$$

The mean field parameters P, Q, ϕ and χ are determined by the following four saddle point equations:

$$\left\langle\frac{\partial\hat{\mathcal{H}}}{\partial P}\right\rangle=0\ ,\quad \left\langle\frac{\partial\hat{\mathcal{H}}}{\partial Q}\right\rangle=0\ ,\quad \left\langle\frac{\partial\hat{\mathcal{H}}}{\partial \phi}\right\rangle=0\quad\text{and}\quad \left\langle\frac{\partial\hat{\mathcal{H}}}{\partial \chi}\right\rangle=0\ . \qquad (6.30)$$

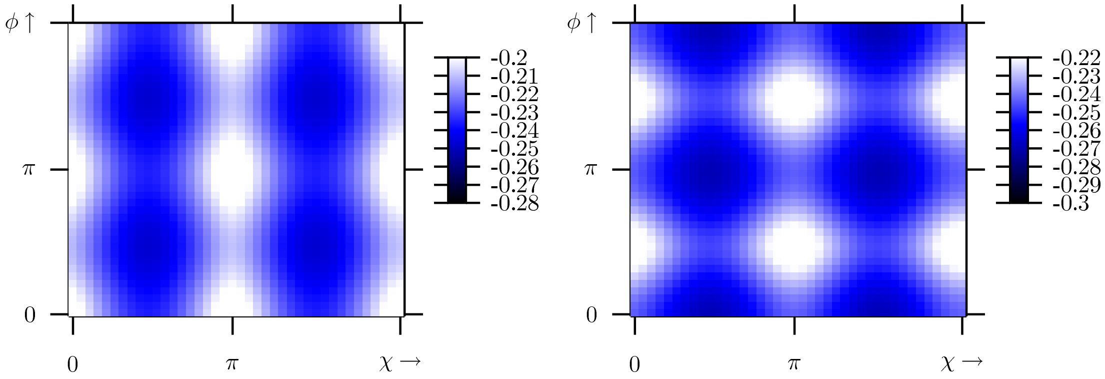

(a) $J_\perp/J_\parallel = -0.5$

(b) $J_\perp/J_\parallel = 0.5$

Figure 6.5: Energy per site with respect to the mean field parameters χ and θ (a) for FM rung coupling ($J_\perp/J_\parallel = -0.5$) and (b) for AF rung coupling ($J_\perp/J_\parallel = 0.5$).

The first two saddle point equations lead to the self-consistent equation:

$$\begin{aligned} Q &= \frac{1}{2L}\sum_k \frac{J_\parallel \cos(k+\chi)\left(2Q\cos(k+\chi)-\sin(k)\right)}{2\sqrt{X}} \\ P &= \frac{1}{2L}\sum_k \frac{J_\perp\left(2P-\cos(\phi)\right)}{2\sqrt{X}} \;, \end{aligned} \tag{6.31}$$

where X is given by

$$X = J_\perp^2\left(\tfrac{1}{4}+P^2-P\cos(\phi)\right)+\tfrac{1}{4}J_\parallel^2\left(\sin(k)-2Q\cos(k+\chi)\right)^2 \;. \tag{6.32}$$

For each fixed set of parameters ϕ and χ the Eqs. (6.31) are solved self-consistently. Fig. 6.5 shows the energy per site depending on ϕ and χ. For $J_\perp < 0$ the total energy is minimal at $\chi = \pi/2$ and $\phi = \pi/2$. However, for $J_\perp > 0$ the total energy is minimal at $\chi = \pi/2$ and $\phi = \pi$.
The hybridized bands are displayed in Fig. 6.6(a) as a function of the FM rung coupling $J_\perp$. Several comments are in order:

(i) For small $J_\perp$, a flat band is apparent reflecting the macroscopic degeneracy of the model at $\theta = \pi$ and $J_\perp = 0$. This leads to a dense spectrum of particle-hole excitations at low energies. This narrow feature indicates a very slow magnon velocity. The slow spin dynamics again set a new low energy scale in the problem, which becomes dominant in the low coupling region where it affects the low energy physics significantly. In the next section this point of view is confirmed by exact diagonalization techniques.

(ii) The minimal particle-hole excitation, corresponding to the spin gap in the spin language, lies at wave vector $k = \pi$ and yields an indirect gap with momentum

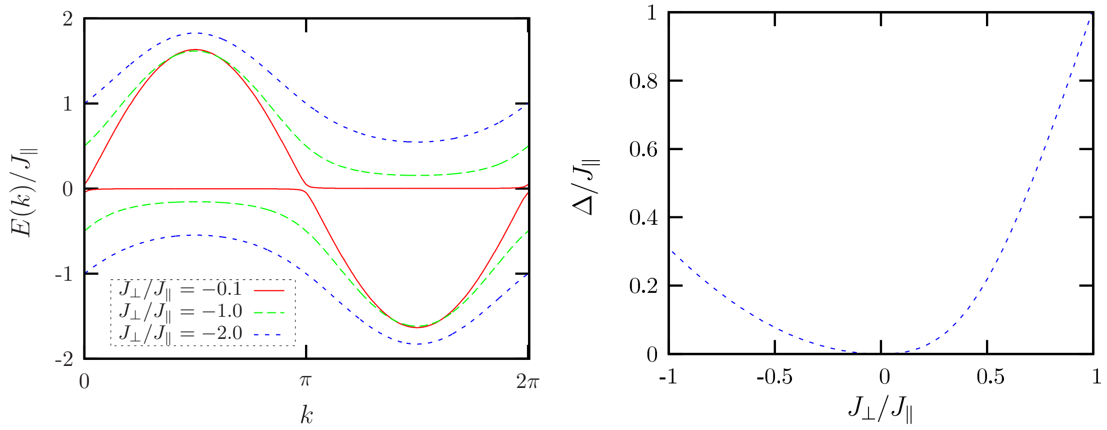

(a) Dispersion relation

(b) Spin gap

Figure 6.6: (a) Results of the Kondo necklace system for the spectra of the spinless fermions for different couplings within the Jordan-Wigner mean field approach for flux phase $\phi = \pi/2$ and $\chi = \pi/2$. (b) Results for the spin gap Δ as a function of coupling $J_\perp/J_\parallel$. In the Kondo necklace system the gap opens as $\Delta \propto J_\perp^2$ for FM and AF rung couplings.

transfer. It is given by

$$\Delta = E_+(3\pi/2) - E_-(\pi/2) \ . \tag{6.33}$$

and represented as a function of $J_\perp$ in Fig. 6.6(b). Fitting the data to a polynomial form, one finds

$$\Delta \propto |J_\perp|^2 \ . \tag{6.34}$$

Hence, the mean field theory for the ladder and Kondo necklace systems show radically different behaviors for the spin gap at low $|J_\perp|$.

6.2 Exact Diagonalization Analysis

In this section the SSH model is analyzed by means of exact diagonalization (ED) techniques using the Lanczos algorithm [1, 96] as introduced in chapter 4. Even though the ED method only enables computation of small systems, it allows to analyze the very weak coupling region of the model and, as demonstrated below, it yields quite reasonable and conclusive results. The analysis starts with the determination of the excitation spectra of the magnons. Therefor one computes the dynamical spin structure factor $S(\mathrm{q},\omega)$ which reads [see Eq. 4.13]

$$S(\mathbf{q},\omega) = \sum_i |\langle\varphi_i|\hat{S}^+_{\mathbf{q}}|\varphi_0\rangle|^2 \delta\left(\omega - (E_i - E_0)\right) \ , \tag{6.35}$$

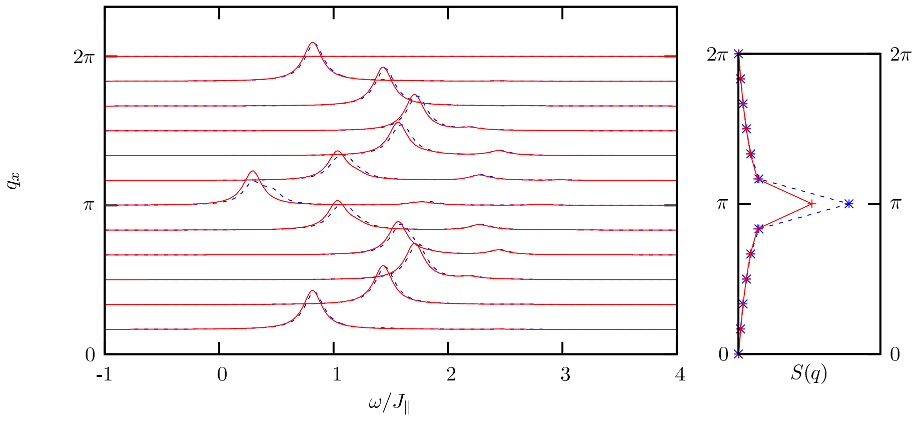

(a) Isotropic Ladder system ($\theta = 0$)

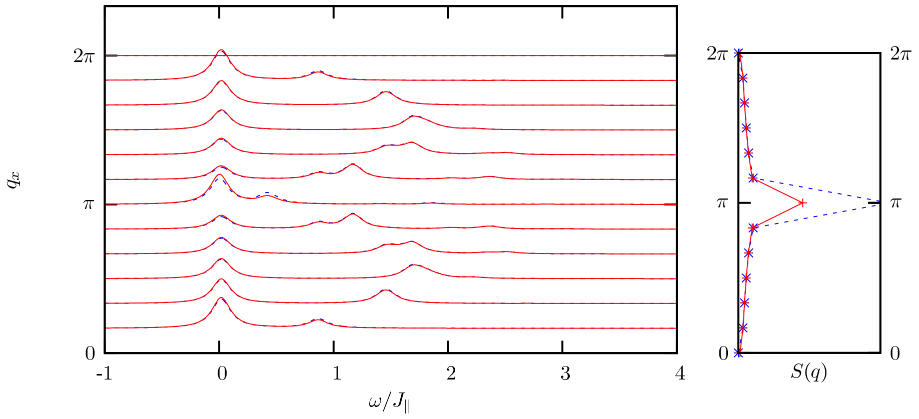

(b) Kondo necklace system ($\theta = \pi$)

Figure 6.7: Dynamical spin susceptibility in the weak coupling limit obtained with ED techniques on a 2×12 lattice: (a) isotropic ladder system ($\theta = 0$) and (b) Kondo necklace system ($\theta = \pi$). In both cases a broadening of $s = 0.1 J_{\|}$ is chosen. The red lines and blue lines correspond to the bonding ($p_y = 0$) and anti-bonding configuration ($p_y = \pi$), respectively.

where the sum runs over all eigenstates $|\phi_i\rangle$ of the Hamiltonian with eigenenergies E_i. $\hat{S}^+_{\mathbf{q}}$ denotes the spin-flip operator in momentum space. Since within the ED methods one deals with a discrete Hilbert space, in the following figures the δ-peaks of Eq. (6.35) are displayed by a Lorentz curve

$$\delta\left(\omega - (E_i - E_0)\right) \quad \rightarrow \quad f(\omega) = \frac{1}{\pi} \frac{1}{s^2 + \left(\omega - (E_i - E_0)\right)^2} \tag{6.36}$$

with a broadening of $s = 0.1 J_{\|}$. Fig. 6.7 presents the spin excitation spectrum for the isotropic ladder ($\theta = 0$) and the Kondo necklace model ($\theta = \pi$) in the weak coupling region. More precisely, it shows the dynamical spin structure factor depending on the momentum q_x along the ladder for both the bonding ($q_y = 0$) and anti-bonding ($q_y = \pi$)

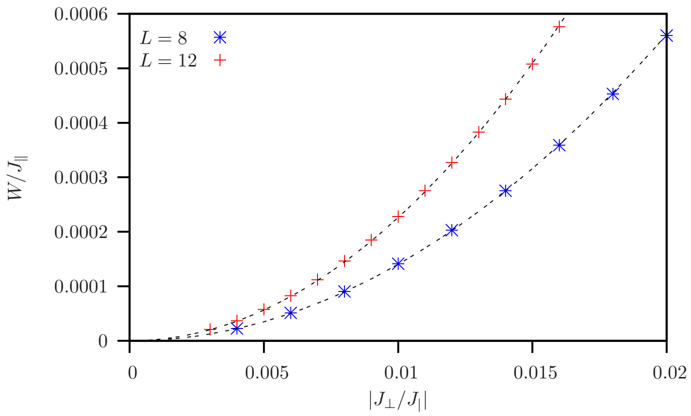

Figure 6.8: ED results for the bandwidth W of the low energy feature in the Kondo necklace model ($\theta = \pi$). The effective SN interaction yields a bandwidth proportional to $J_\perp^2$. The data are fitted to the form $W \propto J_\perp^2$.

configuration. For the ladder case, the dynamical spin structure factor shows features of the two spinon continuum of a single spin-1/2 chain [56] for both the bonding as well as the anti-bonding case. Such a continuum is well reproduced by the mean field theory, and corresponds to the particle-hole continuum stemming from the Hamiltonian of Eq. (6.17) with band structure of Fig. 6.4(a). One should note that the bonding combination, $S(q,\omega)$, has slightly lower energy due to the weak ferromagnetic coupling between the chains.

As apparent in Fig 6.7(b) and as already seen within the Jordan-Wigner mean field approach a narrow band emerges for the Kondo necklace model. One [97] interprets this new low energy scale as a consequence of a Suhl-Nakamura (SN) interaction [36, 37, 38]. The SN interaction describes an effective coupling between the *dangling* spins along the second leg via the AF coupled spins on the first leg. Comparable with an RKKY [16, 17, 18, 19] interaction, where itinerant electrons mediate a long-range spin-spin interaction, the SN coupling causes spin-spin correlation with very slow decay. This long range interaction will be confirmed later in subsection 6.3.1. Due to the mediation of the SN interaction by the coupling on the rungs, in second order perturbation theory the effective SN coupling J_{SN} takes the form

$$J_{\mathrm{SN}} \propto J_\perp^2 \chi(\mathbf{q}, \omega = 0) \ , \tag{6.37}$$

where $\chi(\mathbf{q}, \omega = 0)$ is the spin susceptibility of the spin-1/2 chain. Thus, in the weak coupling region the width W of the low energy feature defined as the differences in energy between the low energy maxima at $q_x = \pi$ and $q_x = \pi/2$ for $\theta = \pi$ should scale as $J_\perp^2/J_\parallel$, too. This scaling behavior in the weak coupling region can be seen in Fig. 6.8 for small lattice sizes. By means of ED techniques the spin gap depending on the interleg coupling $J_\perp$ for small system sizes is also calculated. Unfortunately, for the ladder system ($\theta = 0$) and systems with $\theta < \pi$ size scaling becomes worse with decreasing coupling [see Fig. 6.9(a)] and an interpolation to the thermodynamic limit is not feasible.

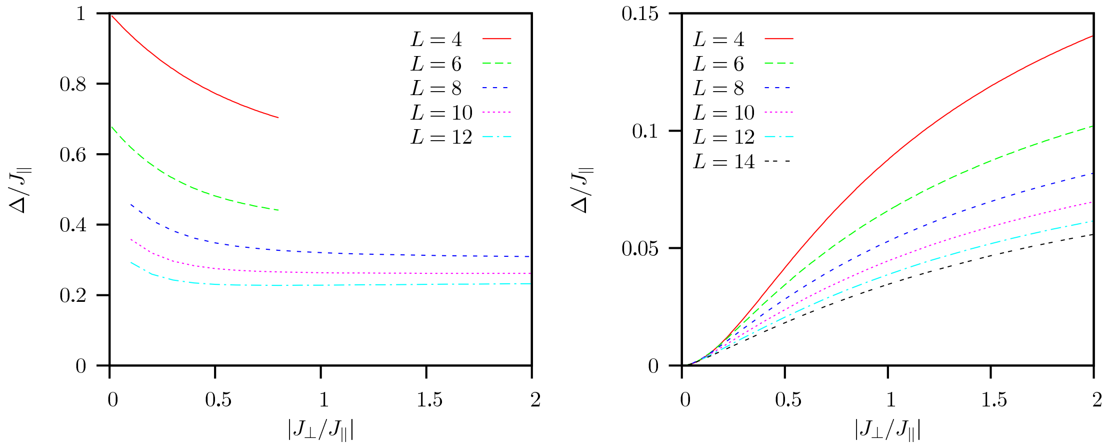

(a) Spin gap for ladder system ($\theta = 0$) (b) Spin gap for Kondo necklace ($\theta = \pi$)

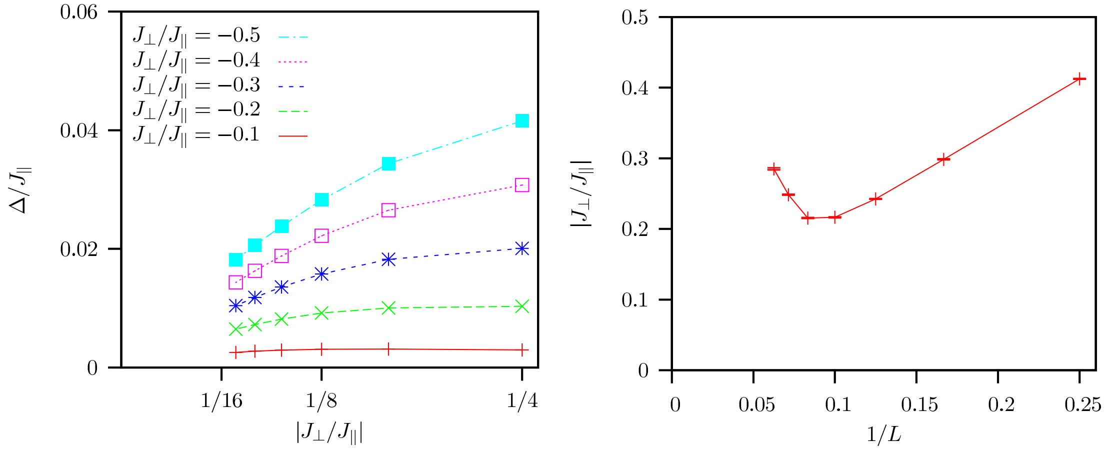

(c) Size scaling (d) Point of inflection

Figure 6.9: Opening of the spin gap for (a) the ladder system ($\theta = 0$) and (b) the Kondo necklace ($\theta = \pi$) obtained by exact diagonalization techniques for different system sizes $2 \times L$. (c) Size scaling for the Kondo necklace system. An extrapolation to the thermodynamic limit is not feasible. (d) Point of inflection as a function of inverse system size in the Kondo necklace model.

However, for $\theta = \pi$ the data for different system sizes seem to collapse in the very weak coupling limit. Even though a systematic size scaling is delicate as demonstrated in Fig. 6.9(c), the overall behavior of the spin gap as a function of interleg coupling $J_\perp$ seems to be similar for all considered lattice sizes. Fig. 6.9(b) depicts the spin gap Δ depending on the coupling $J_\perp/J_\parallel$ for different system sizes $2 \times L$. As apparent, in the weak coupling region and for all shown system sizes the spin gap as a function of $J_\perp$ evolves with a positive curvature. Since in the further development of the spin gap a point of inflection is present, the spin gap converges asymptotically towards a constant value for $|J_\perp| \to \infty$. The point of inflection depending on the system size is depicted in

Fig. 6.9(d). Although the point of inflection initially decreases for small system sizes, it increases again for larger system sizes. Therefore one may suggest that indeed the point of inflection is still present in the thermodynamic limit. A rough estimate locates the point of inflection around $|J_\perp/J_\parallel| \sim 0.5$. Consequently, below this value the spin gap evolves as $\Delta \propto (J_\perp)^\alpha$ with $\alpha > 1$. The data of Fig. 6.9(b) in the weak coupling region is fitted to this form. For all considered lattice sizes one obtains a critical exponent of $\alpha \simeq 2$. This result confirms the differences to the scaling behavior of the spin gap in the ladder system, where it is widely accepted that the gap opens linearly with increasing coupling [35, 95]. Equally to the mean field approach in the Kondo necklace model the spin gap seems to open quadratically depending on $J_\perp$.

Due to the huge density of energy levels in the low coupling region of the Kondo necklace model [see Fig. C.3(a)], difficulties in the convergence of the eigenenergies arise. Therefore, an elaboration of the analysis of the convergence behavior within the ED method by Lanczos iterations is given in appendix C.

6.3 Quantum Monte Carlo Analysis

Since the energy scales for the Kondo necklace model are very small, ED methods proved to be very useful in the weak coupling region $|J_\perp| \gg J_\parallel$. However, to extend the analysis to large system sizes quantum Monte Carlo (QMC) methods are also used with simulations performed at finite inverse temperature $\beta = 1/T$ [97]. In the calculations two variants of the loop algorithm are applied. For the spin-spin correlation function and for the string order parameter discussed later a discrete time algorithm [39] is used. From the spin-spin correlation function one can then extract the spectral function via stochastic analytical continuation schemes [81, 98]. For the spin gap calculation the continuous time loop algorithm of ALPS [99, 100] is applied. Here, the spin gap is calculated via a second moment estimator of the correlation length in imaginary time. For a detailed description the reader is referred to Refs. [29, 101].

6.3.1 Spin-Spin Correlations

The QMC analysis starts with a discussion of the spin-spin correlation function. In section 6.2 the occurrence of the narrow band in the weak coupling spectrum of the Kondo necklace model is interpreted by a long-range SN interaction with a characteristic length scale ξ. On length scales $|i-j| > \xi$ one expects that the static spin-spin correlations decay exponentially:

$$\langle \hat{S}^z_{\alpha,i} \hat{S}^z_{\alpha,j} \rangle \propto (-1)^{|i-j|} |i-j|^{-\gamma} \exp(-|i-j|/\xi) \ . \tag{6.38}$$

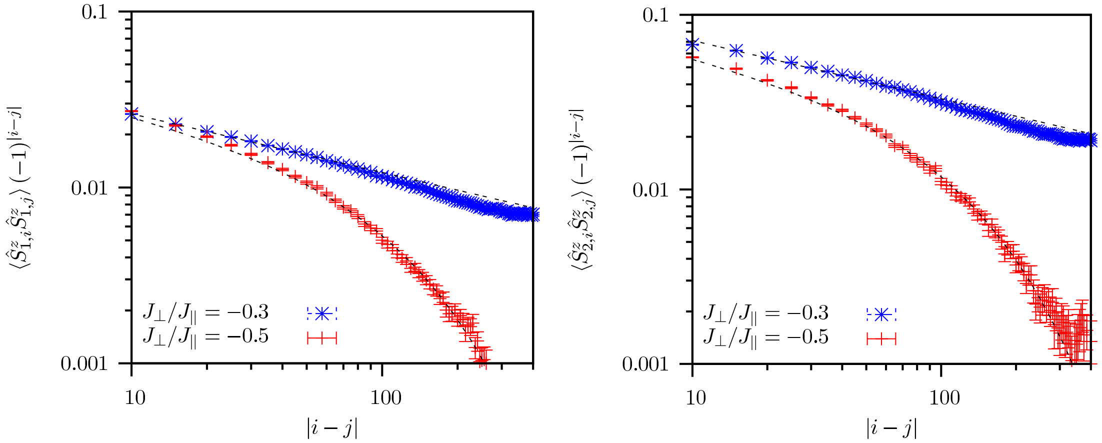

(a) Correlations on leg 1

(b) Correlations on leg 2

Figure 6.10: Static spin-spin correlation function (a) on the first leg and (b) on the second leg for different couplings $J_\perp/J_\parallel$. For $J_\perp/J_\parallel = -0.5$ an exponential decay [fit according Eq. (6.38)] with correlation length $\xi \simeq 115$ is found, whereas for $J_\perp/J_\parallel = -0.3$ the correlation length is larger than the system size. Thus, for very weak couplings the correlation function decays due to the SN interaction as $\langle \hat{S}^z_{\alpha,i}\hat{S}^z_{\alpha,j}\rangle \propto (-1)^{|i-j|}|i-j|^{-\gamma}$ with $\gamma \simeq 1/3$.

For $|i-j| < \xi$ the static spin-spin correlation function follows a slow power law due to the dominating SN interaction, precisely

$$\langle \hat{S}^z_{\alpha,i}\hat{S}^z_{\alpha,j}\rangle \propto (-1)^{|i-j|}|i-j|^{-\gamma} \quad \text{for} \quad |i-j| \ll \xi \ . \tag{6.39}$$

with $\gamma \simeq 1/3$ stemming from the fit [see Fig. 6.10(b)]. This different scaling behavior of the static spin-spin correlation function can be seen in Fig. 6.10. For $J_\perp/J_\parallel = -0.5$ a correlation length of $\xi \simeq 115$ is found. Already on this length scale the correlation function decays exponentially. For decreasing couplings the correlation length ξ rapidly grows and exceeds the order of the considered system sizes. At $J_\perp/J_\parallel = -0.3$ the correlation length is above the system size and only the power law decay caused by the SN interaction is observable. Since there is profound evidence for the domination of the SN interaction in the weak coupling region of the Kondo necklace model, the low energy scale linked to this interaction should also be visible in the magnon excitation spectrum. This can be obtained from the dynamical spin-spin correlation function in imaginary time τ by stochastic analytical continuation schemes.

$$\begin{aligned}
\langle \hat{S}^z_q(\tau)\hat{S}^z_{-q}(0)\rangle &= \frac{1}{\pi}\int d\omega\, \frac{e^{-\tau\omega}}{1-e^{-\beta\omega}} S(q,\omega) \\
\langle \hat{R}^z_q(\tau)\hat{R}^z_{-q}(0)\rangle &= \frac{1}{\pi}\int d\omega\, \frac{e^{-\tau\omega}}{1-e^{-\beta\omega}} R(q,\omega) \qquad (6.40)
\end{aligned}$$

Here, $q \equiv q_x$ stands for the momentum in x-direction along the ladder. $S(q,\omega)$ denotes the dynamical spin structure factor for the bonding ($q_y = 0$), $R(q,\omega)$ is for the anti-

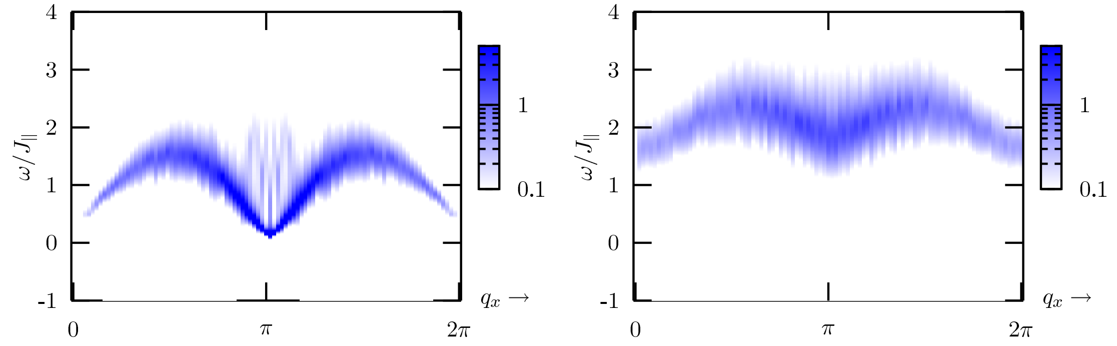

(a) $S(q,\omega)$ for $\theta = 0$

(b) $R(q,\omega)$ for $\theta = 0$

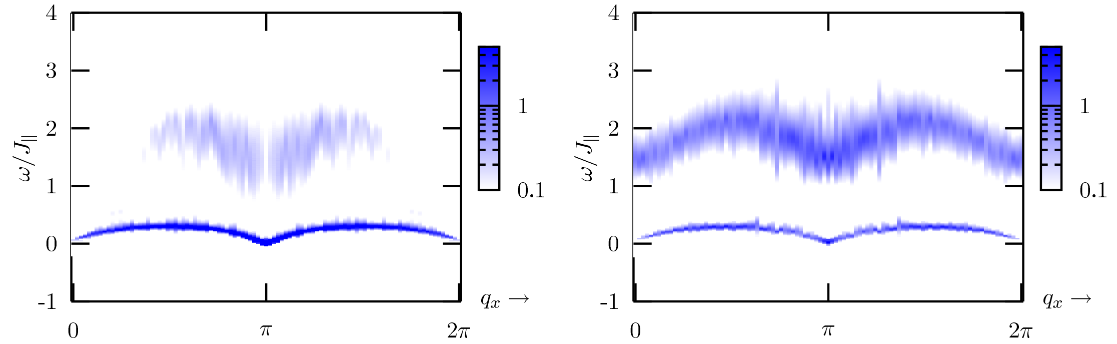

(c) $S(q,\omega)$ for $\theta = \pi$

(d) $R(q,\omega)$ for $\theta = \pi$

Figure 6.11: QMC results of the bonding ($q_y = 0$) and anti-bonding ($q_y = \pi$) dynamical spin susceptibility for the ladder system ($\theta = 0$) (two top panels) and the Kondo necklace system ($\theta = \pi$) (two bottom panels) at $J_\perp/J_\parallel = -1.0$. $\beta J_\parallel = 200.0$ is taken for the simulations.

bonding ($q_y = \pi$) combination of the spin operators across the rungs. $\hat{S}^z_q$ and $\hat{R}^z_q$ are the z-components of the spin operators defined before in Eq. (6.2), but in momentum space. Fig. 6.11 shows the QMC results of the dynamical spin susceptibility for $\theta = 0$ (ladder) and $\theta = \pi$ (Kondo necklace) with 2×100 sites at $J_\perp/J_\parallel = -1.0$ ($\beta J_\parallel = 200$). At $\theta = 0$, inversion symmetry $\hat{\mathbf{S}}_{i,1} \leftrightarrow \hat{\mathbf{S}}_{i,2}$ holds as already mentioned at the beginning of this chapter: $\left[\hat{\mathcal{P}}, \hat{\mathcal{H}}\right] \neq 0$, where $\hat{\mathcal{P}}$ is the parity operator which interchanges the leg labeling. Therefore the ground state and the excited states are symmetric or anti-symmetric. According to Eq. (6.3) $\hat{\mathbf{R}}_i$ changes parity whereas $\hat{\mathbf{S}}_i$ does not. Since the ground state clearly has even parity $S(q,\omega)$ picks up the dynamics of the triplet excitations across the rungs. For FM rung couplings $J_\perp < 0$, one expects low energy spin dynamics represented by $S(q,\omega)$. In the strong coupling limit, $S(q,\omega)$ maps onto the spin structure factor of the Haldane chain. In contrast, $\hat{\mathbf{R}}_i$ is odd under inversion symmetry and $R(q,\omega)$ picks up the singlet excitations across the rungs. As apparent from Fig. 6.11(b) those excitations are located at high energy which is set by $J_\perp$ in the strong coupling limit. At $\theta = \pi$ (Kondo necklace), due to the symmetry breaking mixing of the singlet and triplet formation occurs in the excitation spectra. As apparent in Fig. 6.11(d), $R(q,\omega)$ shows both high and low energy features. The low energy features again are set by the SN interaction $J_{\rm SN} \propto J_\perp^2/J_\parallel$ as shown within the ED calculations of section 6.2.

6.3.2 Spin Gap

Attention is now turned to the analysis of the opening of the spin gap as a function of the coupling $J_\perp$ for different twist angles θ. Since in the low coupling region of the Kondo necklace systems very low energy scales and long length scales occur it poses a great challenge to the numerics. For the presented data simulations are carried out up to $\beta J_\parallel = 2500.0$ and 2×512 spins using the continuous time loop algorithm of ALPS [99, 100]. Fig. 6.12(a) displays the spin gap Δ over a large range of FM rung couplings $J_\perp/J_\parallel$ for various twist angles θ. In the strong coupling limit $J_\perp/J_\parallel \to \infty$ the model maps onto the AF spin-1 Heisenberg chain with effective coupling

$$J_{\rm eff} = \frac{J_\parallel}{4}\left(1+\cos^2(\theta/2)\right) \ . \tag{6.41}$$

The spin gap of the SSH model in units of $J_{\rm eff}$ should then scale to the Haldane gap $\Delta_H/J_{\rm eff} = 0.41048(6)$ [29], irrespective of the angle θ. This behavior is clearly apparent in Fig. 6.12(a). However, as θ grows from $\theta = 0$ to $\theta = \pi$ the approach to the Haldane limit becomes slower.

In the weak coupling region the scaling behavior differs depending on the twist angle. For the ladder system ($\theta = 0$) the data stands in agreement with the independent QMC calculations of Ref. [95], namely the spin gap opens linearly with respect to the coupling $J_\perp$ up to logarithmic corrections. Nevertheless, it is beyond the scope of this work to pin down the exact form of the logarithmic corrections, and the reader is referred to Ref. [95] for further discussion. Enhancing the twist angle from $\theta = 0$ to $\theta = \pi$ leaves the spin gap, measured in units of $J_{\rm eff}$, next to invariant thereby showing that a *small* twist is an irrelevant perturbation. It is noticeable that when increasing the twist angle for $\theta = 0$ to $\theta = \pi/2$ at values of $|J_\perp| < J_\parallel$ the spin gap grows [see Fig. 6.12(b)]. This could be consistent with a logarithmic correction to the gap which depends on the twist. Here and in what follows the logarithmic corrections are neglected. For $\theta < \theta_c$ with $5\pi/6 \lesssim \theta_c \lesssim 8\pi/9$ the spin gap still opens linearly. However, as apparent in Fig. 6.12(c) and Fig. 6.12(d) a linear extrapolation of the data for $\theta = 8\pi/9$ and $\theta = \pi$ would lead to a vanishing of the spin gap at a finite critical value $J_{\perp,c}$. Even though the QMC data evidently do not imply a quadratic dependence of the spin gap on the coupling $J_\perp$, such a scenario should be preferred, since both the mean field approach in section 6.1 and the results obtained by ED methods in section 6.2 suggest an opening of the spin gap given by $\Delta \propto J_\perp^2$. This scenario is also consistent with a point of inflection which, according to the ED results, is located around $J_\perp/J_\parallel \simeq 0.5$ for the Kondo necklace. If one excludes the

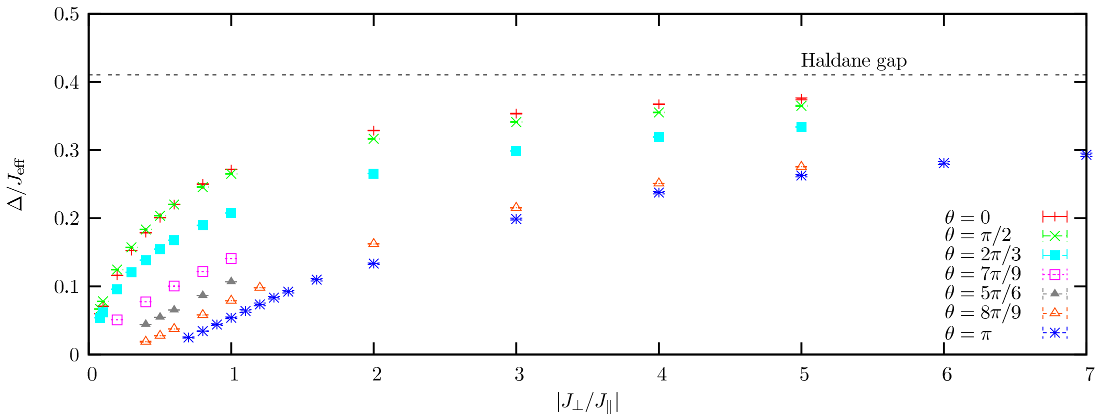

(a) Spin gap Δ depending on $J_\perp/J_\parallel$

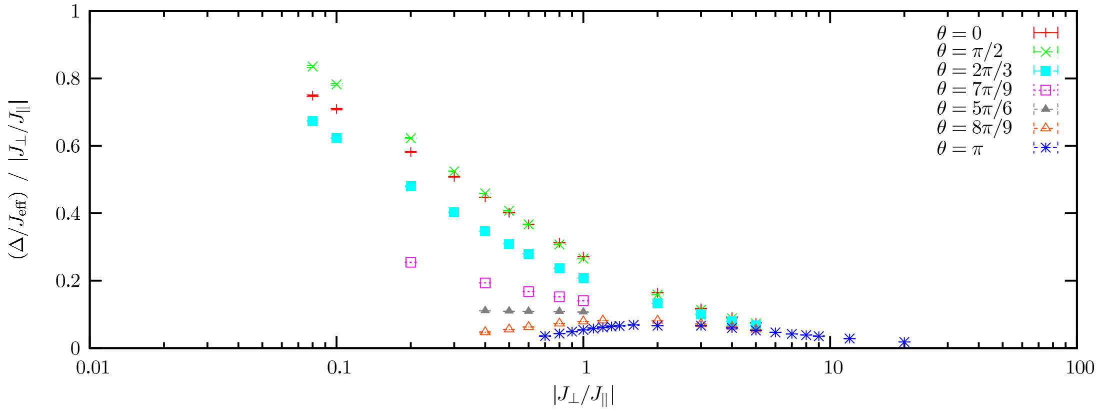

(b) Spin gap Δ depending on $J_\perp/J_\parallel$ (logarithmic scale)

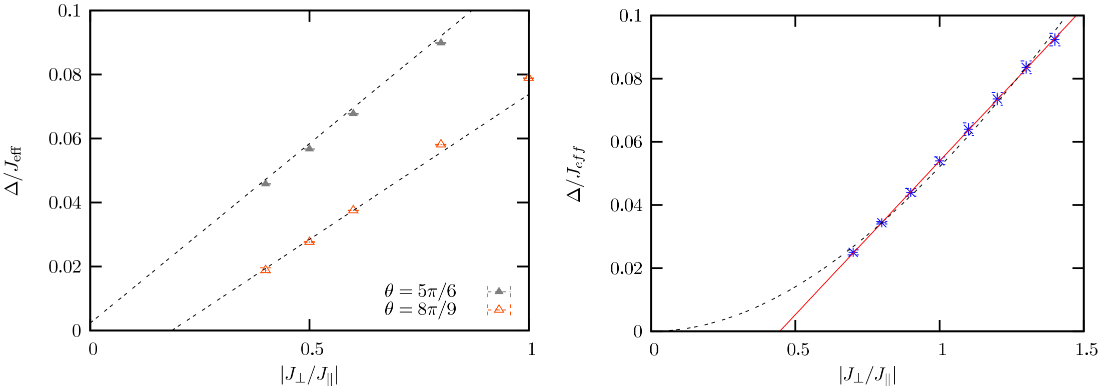

(c) Critical twist angle

(d) Spin gap for $\theta = \pi$

Figure 6.12: (a,b) QMC results for the spin gap. The gap is rescaled by $J_{\text{eff}} = \frac{J_\parallel}{4}\left(1 + \cos^2(\theta/2)\right)$ such that in the large-$J_\perp$ limit it converges asymptotically towards the Haldane gap of an AF spin-1 chain $\Delta_H/J_{\text{eff}} = 0.41048(6)$ [29]. (c) A different scaling behavior of the spin gap is found for $\theta_c \sim 5\pi/6 \dots 8\pi/9$. (d) The dashed line represents a fit of the data to the form $\Delta \propto J_\perp^2$. The red solid line is a linear extrapolation of the data. The simulations are carried out up to $\beta J_\parallel = 2500.0$ and 2×512 spins.

possibility of a finite critical coupling $J_{\perp,c}$, a point of inflection should also be apparent for the case $\theta = 8\pi/9$ and in accordance with the Kondo necklace the spin gap presumably opens quadratically. However, due to the limited amount of data in the weak coupling region the possibility of an exponential decay cannot be excluded. Anyway, there seems to be a small region around $\theta = \pi$ where the scaling behavior of the spin gap in the weak coupling region differs essentially from all other values of θ. In agreement with the data of Fig. 6.12(c) this crossover seems to be located around $5\pi/6 \lesssim \theta_c \lesssim 8\pi/9$. To verify the existence of a spin gap for all $J_\perp \neq 0$, in the following subsection the analysis of the sting order parameters introduced in section 2.4 is presented.

6.3.3 String Order Parameters

In the strong coupling region the system maps onto an effective spin-1 chain, irrespective of the twist angle θ. Thus, the ground state can be understood as a valence-bond solid (VBS) [59, 60]. In the VBS state the spins on a rung form triplets in such a way that if one goes along the ladder and neglects all triplets with magnetic quantum number $m = 0$ one finds a kind of Néel order with an alternating z-component of the total spin. Therefore this state is characterized by a *hidden* AF order, that indicates the Haldane phase of an effective spin-1 chain. To show that the system remains in the Haldane phase for all couplings $J_\perp \neq 0$ and all angles θ the string order parameters as introduced in section 2.4 are determined. For finite systems the string order parameters read

$$\begin{aligned}
\mathcal{O}_s &= \left\langle \hat{S}^z_{n_0} \exp\left[\mathrm{i}\,\pi \sum_{i=n_0}^{n_0+L/2} \hat{S}^z_i\right] \hat{S}^z_{n_0+L/2} \right\rangle \\
\mathcal{O}_H &= \left\langle \exp\left[\mathrm{i}\,\pi \sum_{i=n_0}^{n_0+L/2} \hat{S}^z_i\right] \right\rangle
\end{aligned} \tag{6.42}$$

with $\hat{S}^z_i = \hat{S}^z_{1,i} + \hat{S}^z_{2,i}$. n_0 stands for an arbitrary rung and L denotes the system length. Whereas both order parameter are finite for true Néel order, the order parameter $\mathcal{O}_H$ is zero for hidden magnetic order.

Figs. 6.13(a) to 6.13(c) depict both order parameters, $\mathcal{O}_s$ and $\mathcal{O}_H$, depending on the coupling $J_\perp/J_\parallel$. In the strong coupling region the system is certainly in the Haldane phase irrespective of the twist angle θ indicated by $\mathcal{O}_s > 0$ and $\mathcal{O}_H = 0$. Even if the order parameter $\mathcal{O}_s$ decreases with decreasing coupling $J_\perp$ for the isotropic ladder system ($\theta = 0$) and also apparently for the case $\theta = 8\pi/9$ it remains finite within the whole coupling region. In addition the order parameter $\mathcal{O}_H$ is zero in the weak coupling region, thus indicating that the system is well described by the Haldane physics. However, the situation for the Kondo necklace is more delicate. Here the bare data in Fig. 6.13(c) suggest that the string order parameter $\mathcal{O}_H$ becomes finite for small couplings.

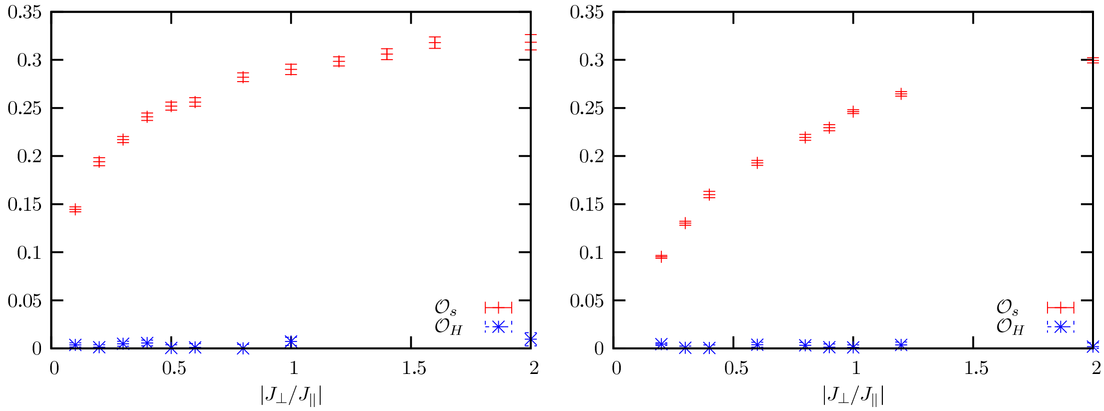

(a) SOPs for $\theta = 0$ (b) SOPs for $\theta = 8\pi/9$

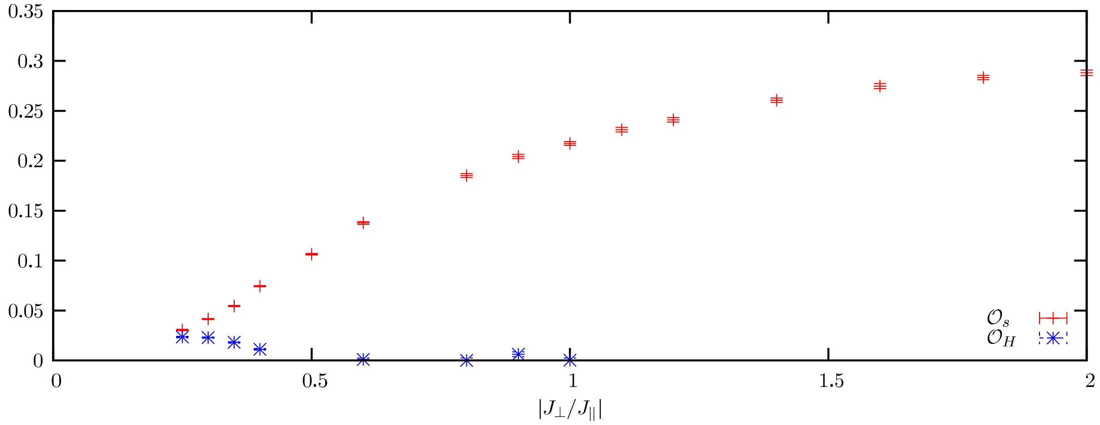

(c) SOPs for $\theta = \pi$

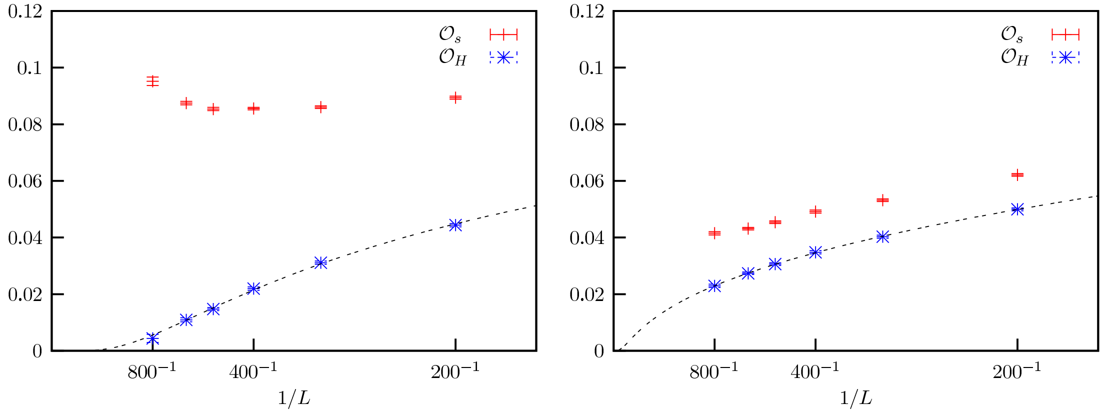

(d) Size scaling for $\theta = 8\pi/9$ and $J_\perp/J_\parallel = -0.2$ (e) Size scaling for $\theta = \pi$ and $J_\perp/J_\parallel = -0.3$

Figure 6.13: (a), (b), (c) String order parameters (SOPs) $\mathcal{O}_s$ and $\mathcal{O}_H$ depending on the coupling $J_\perp$ for different twist angle θ. Simulations are carried out up to $\beta J_\parallel = 7000$ ($\Delta\tau J_\parallel = 0.02$). (d), (e) Finite size scaling of the order parameters. The data for $\mathcal{O}_H$ are fitted to the form $\mathcal{O}_H \propto L^{-\alpha} \exp(-J/\xi)$.

Admittedly as demonstrated in subsection 6.3.1 the correlation length ξ exceeds the lattice length for weak couplings and thus finite size effects are still present. In particular when the lattice size is smaller than the correlation length, both $\mathcal{O}_H$ and $\mathcal{O}_s$ take non-zero values, since the very slow decay of the spin correlations mimics Ising type order. As the system size grows beyond the correlation length, $\mathcal{O}_H$ decreases exponentially whereas $\mathcal{O}_s$ in enhanced. Those size effects are explicitly shown in Fig. 6.13(d) for the parameter set $J_\perp/J_\parallel = -0.2$ and $\theta = 8\pi/9$ where $L \gg \xi$ and in Fig. 6.13(e) for the parameter set $J_\perp/J_\parallel = -0.3$ and $\theta = \pi$ where the maximal system size barely exceeds the estimated correlation length. Taking those size effects into account, one concludes that in the thermodynamic limit, only the string order parameter $\mathcal{O}_s$ is finite in the whole $(\theta, J_\perp)$ plane.

A detailed elaboration of finite size scaling of the string order parameters is given in appendix B. There, one also finds an analysis of temperature effects on the string order parameters.

Summary

In this work one (1D) and two dimensional (2D) quantum spin systems as described by the Heisenberg model were studied. Depending on dimensionality, coupling ratios and lattice topology those systems show various states or phases.

In a first part the bilayer Heisenberg model (BHM) and the 2D Kondo necklace model (KNM) were investigated. Whereas in the BHM the spins on both layer interact directly via an antiferromagnetic (AF) exchange coupling $J_{\|}$, the spins in the second layer of the KNM just couple via an RKKY interaction mediated by the AF coupled spins on the first layer. It was shown that both models exhibit a quantum phase transition between an antiferromagnetically ordered phase and a disordered phase triggered by the interlayer coupling $J_{\perp}$. However, the missing AF coupling within the second layer of the KNM displaces the quantum critical point towards smaller values of $J_{\perp}$. In this work this was shown by measuring the spin stiffness within large scale quantum Monte Carlo (QMC) simulations.

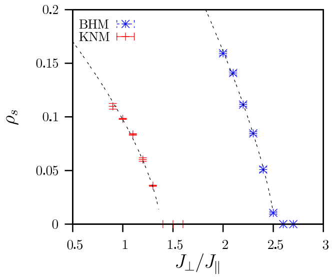

Quantum phase transition

Deep in the disordered phase the excitations are well described by magnons with a cosine like dispersion relation and a minimum gap at the AF wave vector $\mathbf{q} = (\pi, \pi)$. Decreasing the coupling $J_{\perp}$ the spin gap progressively closes and at the critical point the magnons condense at the AF wave vector to form the order of the ordered phase.

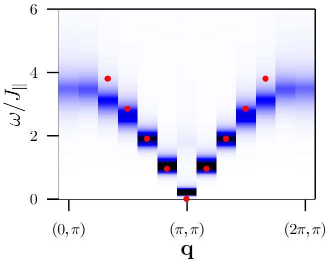

Condensation of triplets

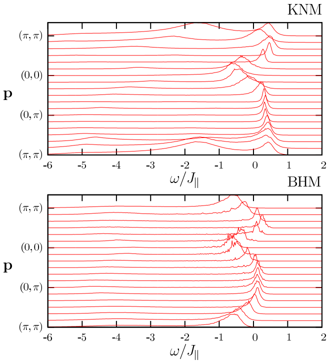

Spectra of doped hole

In a second step the systems were doped with a single hole. It was shown that in the weak coupling region ($J_\perp < J_{\|}$) the single hole dispersion relation differs essentially between both models. For large interlayer coupling the dispersion has a cosine structure with maximum at $\mathbf{p} = (\pi, \pi)$ where $\mathbf{p}$ stands for the hole momentum. However, in the BHM for decreasing coupling the maximum of the dispersion drifts towards $\mathbf{p} = (\pi/2, \pi/2)$, whereas in the KNM the dispersion relation preserves its maximum at $\mathbf{p} = (\pi, \pi)$. The behavior within the KNM is very similar to that of the Kondo lattice model. Here, the localized spins remain partially screened and the strong coupling physics in the single hole dispersion relation is present down to arbitrary low interlayer couplings.

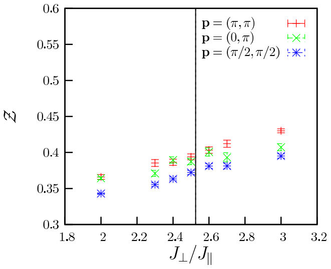

Quasiparticle residue for BHM

The analysis also focused on the coupling of this single doped hole to the magnons across the quantum phase transition. Within a bond mean field approach it was shown that only the hole at rest couples to critical fluctuations. Within a self-consistent Born approximation for the BHM it was shown that this coupling leads to a vanishing quasiparticle residue at the critical coupling $J_{\perp,c}$ of the phase transition. An attempt was made to confirm this point with QMC simulations. In the presented results the accuracy of the single particle Green's function at large imaginary time was limited. With these limitations no convincing evidence was found for a vanishing of the quasiparticle residue at the critical point for a static and mobile hole in the BHM as well as for a mobile hole in the KNM.

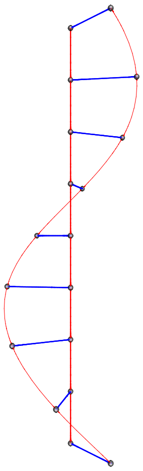

SSH model

In the second part of this work attention was turned to the 1D spiral staircase Heisenberg (SSH) model. Here, two antiferromagnetically coupled ($J_{\|}$) spin-1/2 chains with ferromagnetic interchain coupling $J_\perp$ form a spin ladder. A continuous twist deformation along the first leg, denoted by the twist angle θ, rescales the AF coupling along the second leg to the form $J_{\|} \cos^2(\theta/2)$.

This model is of particular interest since it mediates between a spin-1/2 chain and an effective spin-1 chain. Motivated by the Haldane conjecture, which states that antiferromagnetically coupled half-integer spin chains are gapless whereas integer spin chains have a gap, the crossover between the ungapped and gapped phase can be studied using the SSH model. Hence, the primary question was the opening of the spin gap as a function of the interchain coupling $J_\perp$.

First, the model was tackled by a Jordan-Wigner mean field calculation. Already at this simple level the scaling behavior of the spin gap differs essentially between the two extreme cases, the isotropic ladder ($\theta = 0$) and the 1D Kondo necklace ($\theta = \pi$). Whereas in the isotropic ladder the gap opens linearly with respect to $J_\perp$, in the Kondo necklace it was found to have a quadratic dependency in the weak coupling region. The results are essentially affected by the topology of the systems. The ladder topology consists of closed paths where – in terms of the Jordan-Wigner approach – spinless fermions can circulate allowing for a π-flux phase. Such a solution is not possible in the 1D Kondo necklace model. Here a hybridized band structure occurs, composed of a flat band, accounting for the *dangling* spins, and a cosine band, which leads to an indirect spin gap.

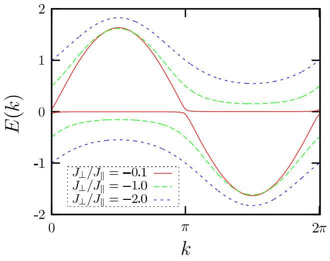

Hybridized bands

The different scaling behavior was confirmed with exact diagonalization techniques, which also reveal a narrow feature in the spin excitation spectrum of the Kondo necklace for small couplings. This feature indicates a very slow spin velocity and introduces a new low energy scale into the problem. This new energy scale can be explained by a Suhl-Nakamura (SN) interaction, which – comparable to the RKKY interaction – causes long-range spin correlations which decay according to a power law. This long-range order was confirmed within large scale QMC simulations, thus supporting the view of the occurrence of the SN interaction.

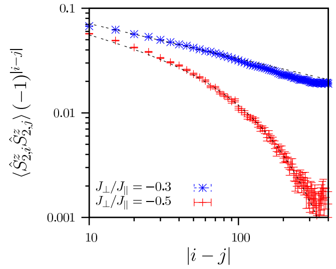

Long ranged SN interaction

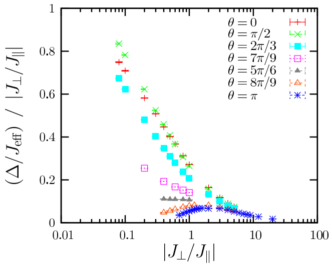

Opening of the spin gap

By means of QMC simulations the opening of the spin gap depending on the twist angle θ was investigated. Although the QMC data did not explicitly show a quadratic opening of the spin gap for $\theta = \pi$, it implies that the spin gap scales as $\Delta \propto (J_\perp)^\alpha$ with at least $\alpha > 1$ in order to exclude a finite critical coupling where the spin gap vanishes. In addition such scaling behavior is also observable in the close vicinity around $\theta = \pi$. The crossover to a linear opening was located between $\theta = 5\pi/6$ and $\theta = 8\pi/9$.

To complete this view the string order parameters, which indicate the order of the system, were also calculated within the QMC approach. It was found that, independent of the choice of the parameter set, the system remains in the so-called Haldane phase which is gapped and characterized by a hidden AF order. Thus, the occurrence of a finite critical coupling where the spin gap closes can be excluded and a different scaling behavior depending on θ is obvious.

Calculation of First Order Self-Energy

A

In the following the calculation of the first order self-energy at zero temperature ($\beta \to \infty$) given in Eq. (5.47)

$$\Sigma^{(1)}(\mathbf{p},\omega) = \mathrm{i} \int \mathrm{d}^2\mathbf{q} \int \mathrm{d}\eta \; g_b^2(\mathbf{q}) \; \mathcal{G}_0(\mathbf{p}+\mathbf{q},\omega+\eta) \; \mathcal{D}_0(-\mathbf{q},-\eta) \tag{A.1}$$

is shown explicitly. The free propagators for the hole $\mathcal{G}_0$ and for the magnons $\mathcal{D}_0$ are taken from Eq. (5.48) and transformed via analytic continuation from the real axis to the imaginary axis by setting $\omega + \mathrm{i}\,0^+ \to \mathrm{i}\,\omega_n$, where the bosonic Matsubara frequencies are defined as $\omega_n = 2\pi n/\beta$ with $n \in \mathbb{Z}$:

$$\begin{aligned} \mathcal{G}_0(\mathbf{p}+\mathbf{q},\mathrm{i}\,\omega_n+\mathrm{i}\,\eta_n) &= \frac{1}{\mathrm{i}\,\omega_n+\mathrm{i}\,\eta_n-\varepsilon(\mathbf{p}+\mathbf{q})} \\ \mathcal{D}_0(-\mathbf{q},-\mathrm{i}\,\eta_n) &= \frac{1}{-\mathrm{i}\,\eta_n-\Omega(\mathbf{q})} \; . \end{aligned} \tag{A.2}$$

Here, the symmetry in the magnon dispersion is used: $\Omega(\mathbf{q}) = \Omega(-\mathbf{q})$. Due to the Wick rotation onto the imaginary time axis the energy integration in Eq. (A.1) has to be replaced by a sum over the Matsubara frequencies:

$$\mathrm{i} \int \mathrm{d}\eta \to -\frac{1}{\beta} \sum_{\mathrm{i}\,\eta_n} \; . \tag{A.3}$$

The first order self energy then reads

$$\Sigma^{(1)}(\mathbf{p},\mathrm{i}\,\omega_n) = \int \mathrm{d}^2\mathbf{q} \; g_b^2(\mathbf{q}) \; \frac{1}{\beta} \sum_{\mathrm{i}\,\eta_n} \frac{1}{\mathrm{i}\,\omega_n+\mathrm{i}\,\eta_n-\varepsilon(\mathbf{p}+\mathbf{q})} \; \frac{1}{\mathrm{i}\,\eta_n+\Omega(\mathbf{q})} \; . \tag{A.4}$$

The evaluation of the bosonic Matsubara sum, given by

$$\mathrm{MS} = \frac{1}{\beta} \sum_{\mathrm{i}\,\eta_n} f(\mathrm{i}\,\eta_n) \quad \text{with} \quad f(\mathrm{i}\,\eta) = \frac{1}{\mathrm{i}\,\omega_n+\mathrm{i}\,\eta_n-\varepsilon(\mathbf{p}+\mathbf{q})} \; \frac{1}{\mathrm{i}\,\eta_n+\Omega(\mathbf{q})} \tag{A.5}$$

follows the standard calculation pointed out, for example, in Ref. [102]. By using the Cauchy integral formula the Matsubara sum can be rewritten as

$$\mathrm{MS} = \frac{1}{2\pi\beta} \sum_n \oint_{C_n} \mathrm{d}z \, \frac{f(z)}{e^{\beta z}-1} \tag{A.6}$$

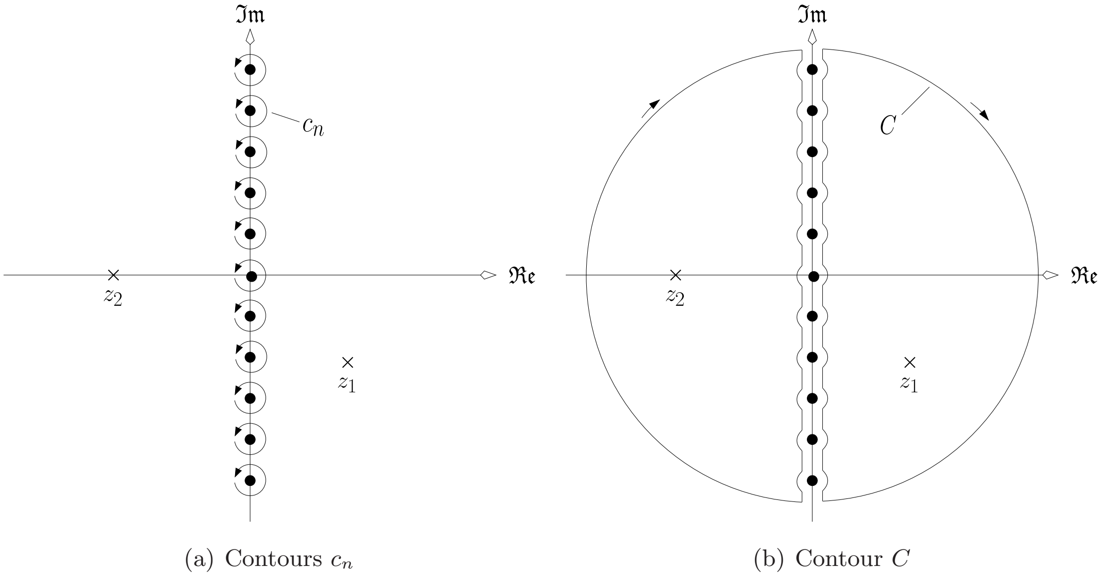

(a) Contours c_n (b) Contour C

Figure A.1: Integration paths. The black solid dots mark the singularities of the Bose-Einstein distribution, which correspond to the Matsubara frequencies $\mathrm{i}\,\eta_n$. The crosses indicates the singularities of $f(z)$.

where the c_n's denote infinitely small circles around the singularities of the function

$$g(z) = \frac{f(z)}{e^{\beta z} - 1} \tag{A.7}$$

As apparent, the singularities lie on the imaginary time axis [see Fig. A.1(a)] exactly at the Matsubara frequencies $\mathrm{i}\,\eta_n$. Since $|g(z)| \to 0$ faster than $|z|^{-1}$ as $|z| \to \infty$ Jordan's lemma states that the circles c_n of Eq. (A.6) can be substituted by the contour shown in Fig. A.1(b). Thus,

$$\mathrm{MS} = \frac{1}{2\pi\beta} \int_C \mathrm{d}z \, \frac{f(z)}{e^{\beta z} - 1} \ . \tag{A.8}$$

Now, only singularities of the function $f(z)$ lie within the contour C. By using the residue theorem the integral of Eq. (A.8) can be evaluated:

$$\mathrm{MS} = -\sum_i \mathrm{Res}\left[g(z), z_i\right] \ . \tag{A.9}$$

The minus sign occurs since the contour C is orientated clockwise. z_i denotes the singularities of $f(z)$ which are

$$z_1 = \varepsilon(\mathbf{p}+\mathbf{q}) - \mathrm{i}\,\omega_n \quad \text{and} \quad z_2 = -\Omega(\mathbf{q}) \ . \tag{A.10}$$

The corresponding residue are given by

$$\mathrm{Res}\left[g(z), z_1\right] = \frac{1}{e^{-\mathrm{i}\,\beta\omega_n} e^{\beta\varepsilon(\mathbf{p}+\mathbf{q})} - 1} \, \frac{1}{\varepsilon(\mathbf{p}+\mathbf{q}) - \mathrm{i}\,\omega_n + \Omega(\mathbf{q})} \quad \text{and} \tag{A.11}$$

$$\mathrm{Res}\left[g(z), z_2\right] = \frac{1}{e^{-\Omega(\mathbf{q})} - 1} \, \frac{1}{\mathrm{i}\,\omega_n - \Omega(\mathbf{q}) - \varepsilon(\mathbf{p}+\mathbf{q})} \ . \tag{A.12}$$

The self-energy is to be calculated at *zero* temperature, therefore the limit $\beta \to \infty$ should now be taken. Since $\varepsilon(\mathbf{p}+\mathbf{q}) > 0$ and $\Omega(\mathbf{q}) > 0$ the residue (A.11) vanishes in this limit: $\mathrm{Res}\,[g(z), z_1] \to 0$ for $\beta \to \infty$, and the Matsubara sum reduces to

$$\mathrm{MS} = \frac{1}{\mathrm{i}\,\omega_n - \Omega(\mathbf{q}) - \varepsilon(\mathbf{p}+\mathbf{q})} \; . \tag{A.13}$$

Finally one obtains the first order self-energy

$$\Sigma^{(1)}(\mathbf{p}, \mathrm{i}\,\omega_n) = \int \mathrm{d}^2\mathbf{q}\; g_b^2(\mathbf{q}) \, \frac{1}{\mathrm{i}\,\omega_n - \Omega(\mathbf{q}) - \varepsilon(\mathbf{p}+\mathbf{q})} \tag{A.14}$$

which corresponds to the form given in Eq. (5.50):

$$\Sigma^{(1)}(\mathbf{p}, \omega) = \int \mathrm{d}^2\mathbf{q}\; g_b^2(\mathbf{q}) \, \frac{1}{\omega - \Omega(\mathbf{q}) - \varepsilon(\mathbf{p}+\mathbf{q}) + \mathrm{i}\,0^+} \; . \tag{A.15}$$

Scaling Behavior of the String Order Parameters

B

The size and temperature scaling of the string order parameters is very delicate, epecially in the weak coupling limit $|J_\perp| \ll J_\parallel$ of the one dimensional Kondo necklace model discussed in chapter 6. Here, additional data is presented which shows the difficulty in the calculation of the string order parameters $\mathcal{O}_s$ and $\mathcal{O}_H$.

B.1 Temperature Scaling

For weak ferromagnetic interleg couplings $J_\perp$ one is confronted with very low energy scales, especially at $\theta = \pi$. In order to resolve them one has to carry out simulations on very large system sizes and at very low temperatures. The following figures demonstrate the huge effort that is needed to resolve such low energy scales. Fig. B.1(a) depicts the function defined as

$$G_s(n) = \left\langle \hat{S}^z_{n_0} \exp\left(\mathrm{i}\,\pi \sum_{i=n_0}^{n_0+n} \hat{S}^z_i \right) \hat{S}^z_{n_0+n} \right\rangle \tag{B.1}$$

for the Kondo necklace model at $J_\perp/J_\parallel = -0.4$. Here, $\hat{S}^z_i = \hat{S}^z_{1,i} + \hat{S}^z_{2,i}$ where $\hat{S}^z_{\alpha,i}$ is the z-component of the spin operator acting on rung i and leg α. n_0 denotes an arbitrary rung. The string order parameter $\mathcal{O}_s$ is then given by $\mathcal{O}_s = \lim_{n\to\infty} G_s(n)$. Since within the quantum Monte Carlo simulations one deals with finite system sizes the string order parameter is determined by $\mathcal{O}_s = G_s(n)|_{n=L/2}$ where L is the linear system size. Fig. B.1(b) shows the string order parameter extracted from the data given in Fig. B.1(a). As apparent for $J_\perp/J_\parallel = -0.4$ in the Kondo necklace system temperatures below $T/J_\parallel = 1/5000$ are needed to ensure convergence of the string order parameter $\mathcal{O}_s$. For comparison Fig. B.1(c) shows the temperature scaling in the isotropic ladder system. Here, the string order parameter for $J_\perp/J_\parallel = -0.4$ seems to be converged in temperature already at $\beta J_\parallel \simeq 1400$. However, it is noticeable that the statistics in the ladder system are worse than in the Kondo necklace system and lead to much larger error bars.
Fig. B.2 presents more data for the temperature scaling of the Kondo necklace model.

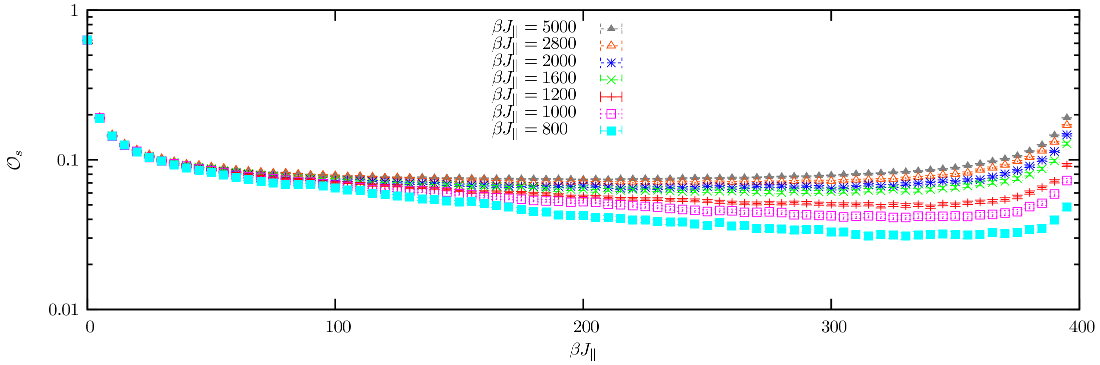

(a) $G_s(n)$ for various temperatures at $J_{\perp}/J_{\parallel} = -0.4$

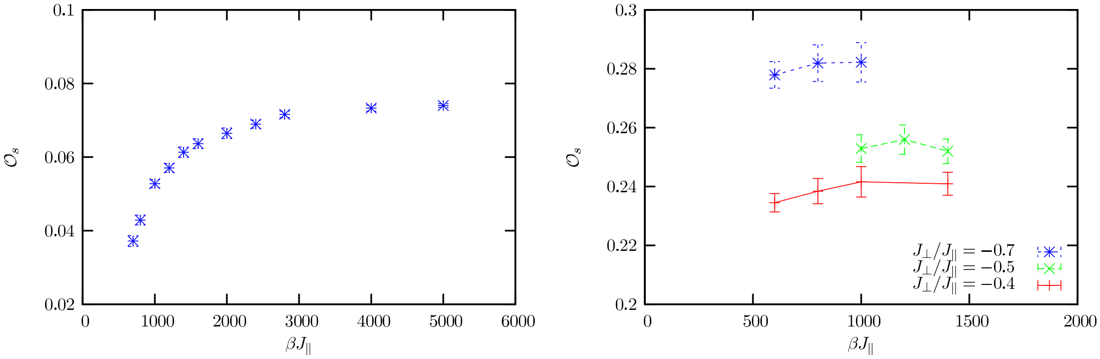

(b) Kondo necklace at $J_{\perp}/J_{\parallel} = -0.4$

(c) Ladder system

Figure B.1: Temperature scaling of the string order parameter $\mathcal{O}_s$: (a) Function $G_s(n)$ as defined in Eq. (B.1) for various inverse temperatures β in the Kondo necklace at $J_{\perp}/J_{\parallel} = -0.4$. The string order parameter is extracted at $n = 200$: $\mathcal{O}_s = G_s(n)|_{n=200}$, and plotted in Fig. B.1(b). (c) For comparison, $\mathcal{O}_s$ for the isotropic ladder system. All simulations are carried out with a 2×400 system.

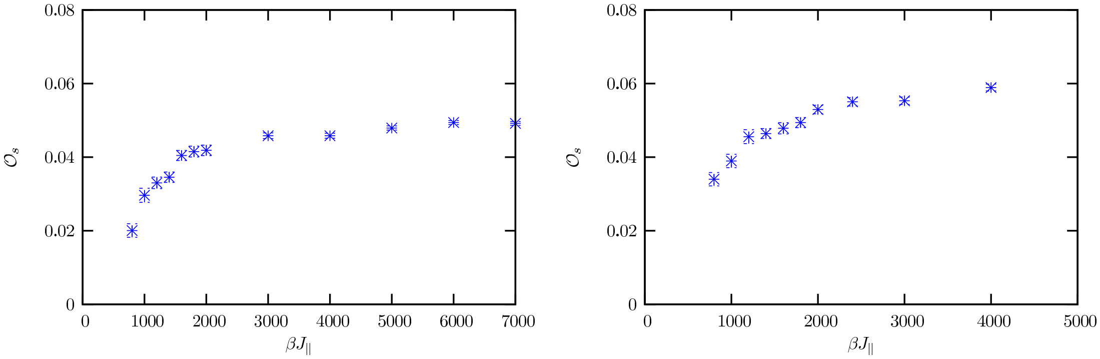

(a) Kondo necklace at $J_{\perp}/J_{\parallel} = -0.3$

(b) Kondo necklace at $J_{\perp}/J_{\parallel} = -0.35$

Figure B.2: Temperature scaling of the string order parameter $\mathcal{O}_s$ in the Kondo necklace system. All simulations are carried out with a 2×400 system. ($\Delta\tau J_{\parallel} = 0.02$)

B.2 Size Scaling

The following figures show the size scaling of the string order parameters $\mathcal{O}_s$ and $\mathcal{O}_H$. The order parameter $\mathcal{O}_H$ is defined according to $\mathcal{O}_s$:

$$\mathcal{O}_H = G_H(n)\big|_{n=L/2} \quad \text{with} \quad G_H(n) = \left\langle \exp\left(\mathrm{i}\,\pi \sum_{j=n_0}^{n_0+n} , \hat{S}_j^z \right) \right\rangle \tag{B.2}$$

where n_0 is an arbitrary rung. The results suggest that $\mathcal{O}_s$ remains finite for all couplings, whereas $\mathcal{O}_H$ is zero in the thermodynamic limit. The data for the string order parameter $\mathcal{O}_H$ is fitted to the form

$$\mathcal{O}_H \propto L^{-\alpha} \exp(-L/\xi) \tag{B.3}$$

where ξ denotes the correlation length.

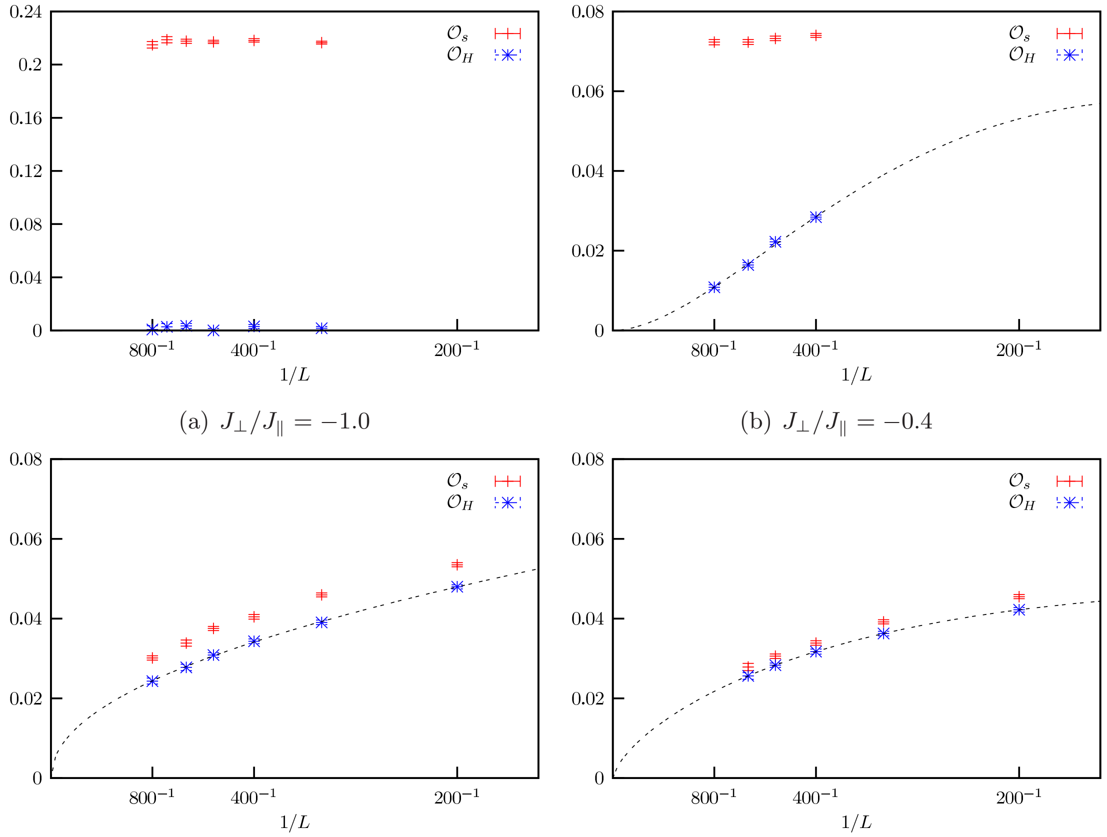

(a) $J_\perp/J_\parallel = -1.0$

(b) $J_\perp/J_\parallel = -0.4$

(c) $J_\perp/J_\parallel = -0.25$

(d) $J_\perp/J_\parallel = -0.2$

Figure B.3: Size scaling in the Kondo necklace model ($\theta = \pi$). The data for the string order parameter $\mathcal{O}_H$ is fitted to the form given in Eq. (B.3). ($\Delta\tau J_\parallel = 0.02$)

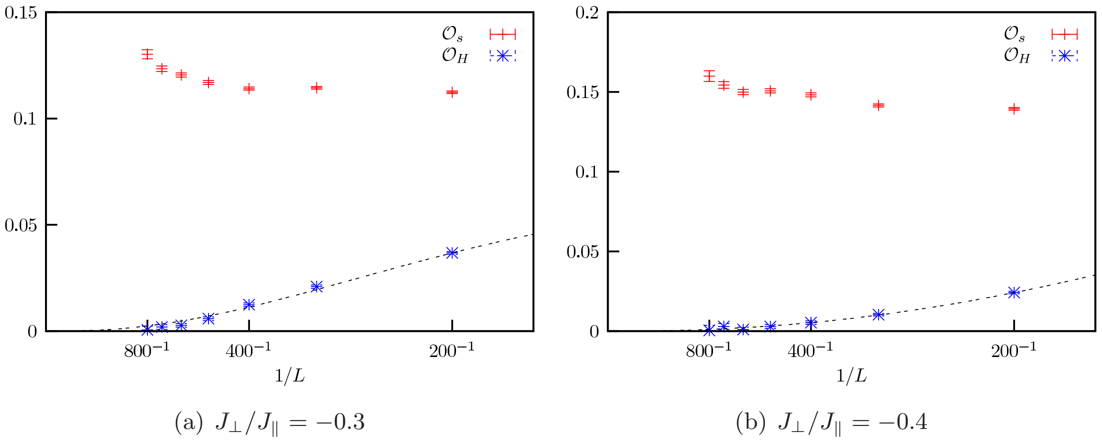

(a) $J_\perp/J_\parallel = -0.3$

(b) $J_\perp/J_\parallel = -0.4$

Figure B.4: Size scaling for the case $\theta = 8\pi/9$. The data for the string order parameter $\mathcal{O}_H$ is fitted to the form given in Eq. (B.3). ($\Delta\tau J_\parallel = 0.02$)

Convergence of the Lanczos Method

C

Usually, $n \simeq 100$ iterations within the Lanczos method are sufficient in order to obtain convergence to the lowest eigenvalue. Fig. C.1 demonstrates the convergence behavior for a typical parameter set in the spiral staircase Heisenberg model.

As apparent in Fig. C.1, the error in the ground state energy ϵ_0 for $J_\perp/J_\parallel = -1.0$ in the Kondo necklace on a 2×12 lattice after 100 iterations is less than $\Delta\epsilon/(2LJ_\parallel) = 10^{-11}$. However, with decreasing interleg coupling $J_\perp$ the resolution in energy becomes more difficult due to the low energy scales. This is also reflected by the slow convergence to the ground state energy for weak couplings as shown in Fig. C.2(c) and Fig. C.2(d). In particular, the convergence of the energy within the Kondo necklace model is very slow. The convergence is affected by the energy level separations. By increasing twist angle θ the energy levels collapse [see Fig. C.3(a)]. Thus the convergence to the ground state level is more difficult in the Kondo necklace model ($\theta = \pi$) than for the isotropic ladder ($\theta = 0$). This is shown in Fig. C.3(b).

Besides the ground state energy the energy of the second lowest energy level also has to be known in order to determine the spin gap. In the case of the spiral staircase Heisenberg model the second lowest energy level corresponds to triplet excitations. Thus, due to symmetry arguments it can be obtained from the ground state energy of the $m = \pm 1$ block in the Hamilton matrix since the actual ground state is a $m = 0$ singlet state. Here, m denotes the magnetic quantum number of the z-component of the total spin.

The second lowest energy can also be calculated within the Lanczos iterations, but converges more slowly than the ground state energy. This can be seen in Fig. C.4. Furthermore, after the second lowest energy is converged it drops down to the ground state energy and causes an *artificial degeneracy*. This may induce confusion in the allocation of the energy levels.

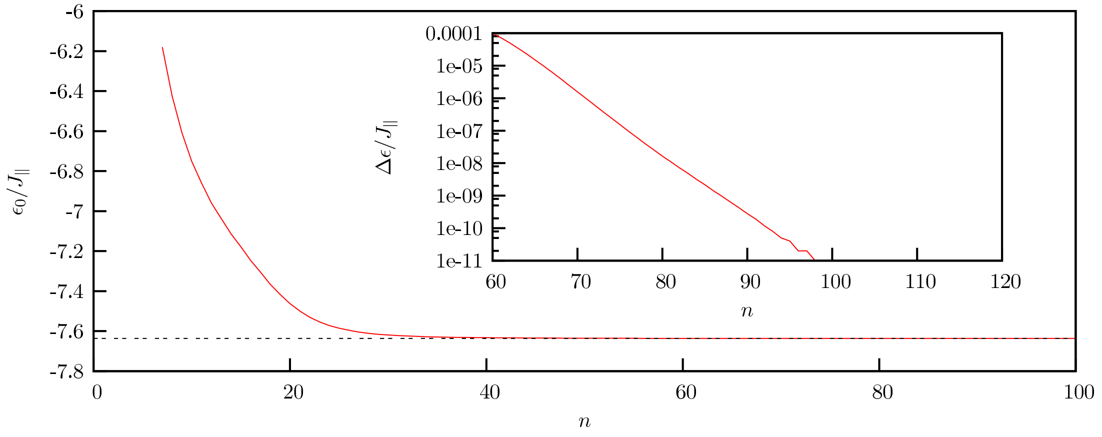

Figure C.1: Ground state energy ϵ_0 as a function of Lanczos iterations n for the Kondo necklace model at $J_\perp/J_\parallel = -1.0$ on a 2×12 lattice. The inset depicts the difference $\Delta\epsilon$ between the ground state energy after n iterations and the exact ground state energy for $n \to \infty$.

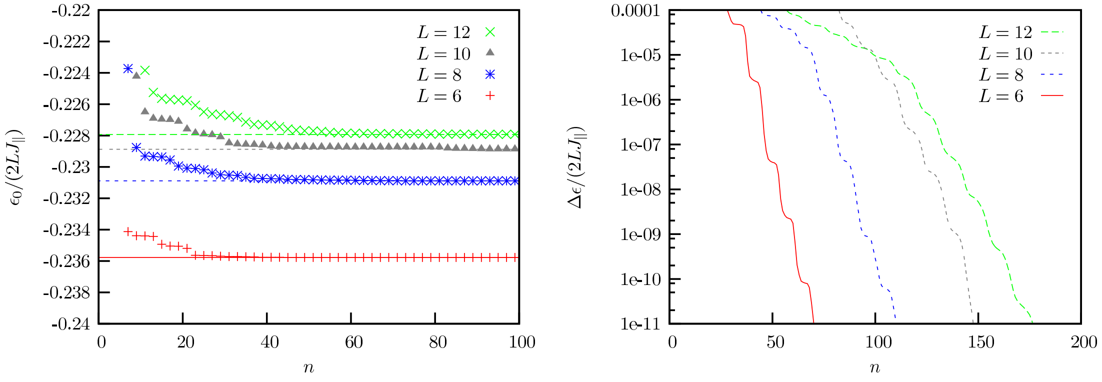

(a) Size dependent convergence (b) Size dependent convergence (logscale)

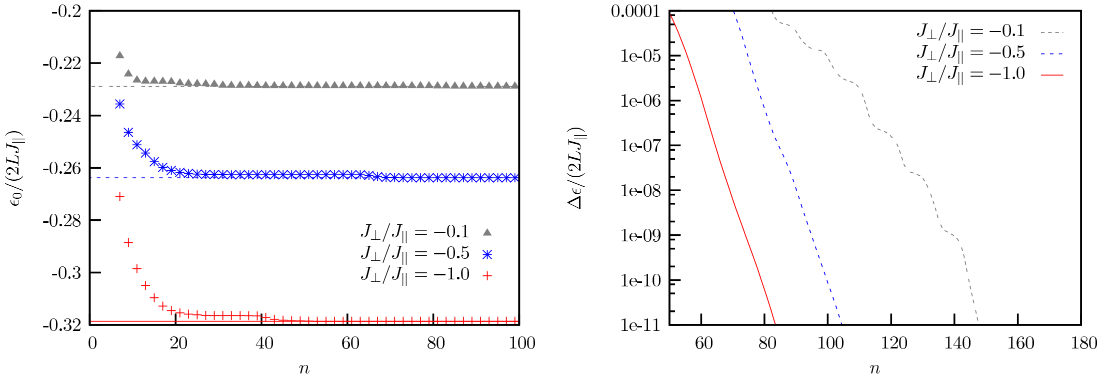

(c) Coupling dependent convergence (d) Coupling dependent convergence (logscale)

Figure C.2: (a,c) Convergence to the ground state energy per site $\epsilon_0/(LJ_\parallel)$ for different lattice sizes ($J_\perp/J_\parallel = -0.1$) and different couplings ($L = 10$), respectively. (b,d) Error $\Delta\epsilon/(2LJ_\parallel)$ after n iterations.

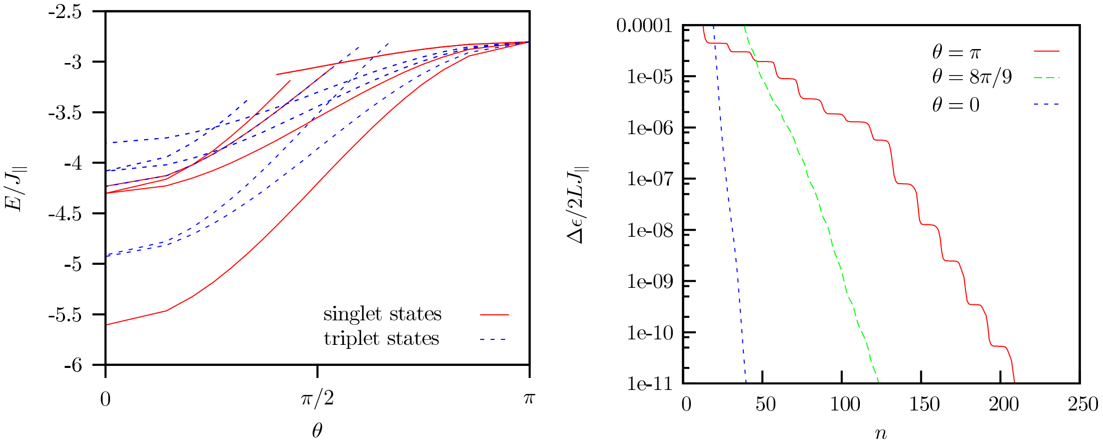

(a) Collapse of energy levels

(b) Convergence for different twist angles θ

Figure C.3: (a) In the Kondo necklace model the energy levels collapse which causes difficulties in the determination of the ground state energy. ($L = 6$, $J_\perp/J_\parallel = -0.01$) (b) Error $\Delta\epsilon/J_\parallel$ in the ground state energy after n iterations for different twist angles θ. ($L = 10$, $J_\perp/J_\parallel = -0.01$)

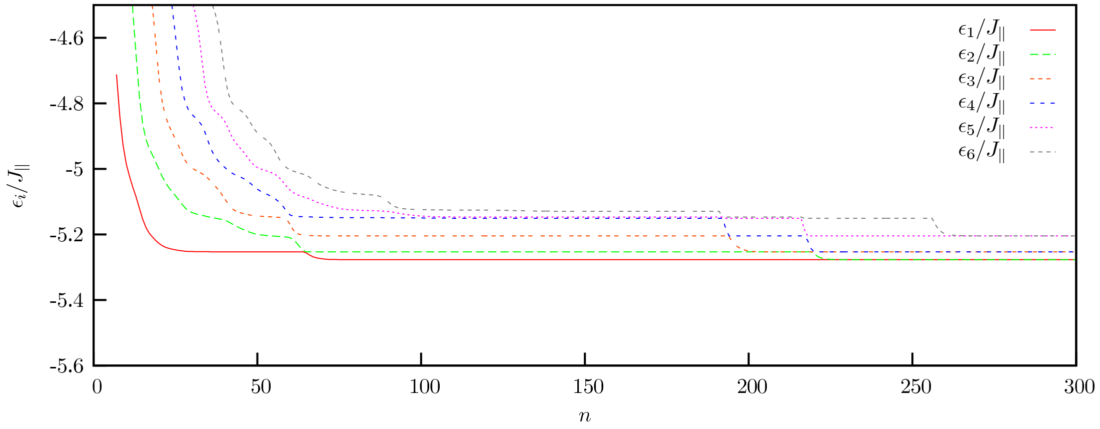

Figure C.4: Artificial degeneracy of the ground state. For large n (number of iterations) higher energies drop down to the ground state energy. ($J_\perp/J_\parallel = -0.5$, $L = 10$, $\theta = \pi$)

Loop Length and Correlation Time

D

Within the path integral quantum Monte Carlo simulations the loop algorithm is a very efficient updating scheme, which leads to small autocorrelation times τ_c. The autocorrelation function is defined as

$$C_0(t) = \frac{\frac{1}{N}\sum_{s=1}^{N} \mathcal{O}(x_s)\mathcal{O}(x_{s+t}) - \left(\frac{1}{N}\sum_{s=1}^{N} \mathcal{O}(x_s)\right)^2}{\frac{1}{N}\sum_{s=1}^{N} \mathcal{O}(x_s)^2 - \left(\frac{1}{N}\sum_{s=1}^{N} \mathcal{O}(x_s)\right)^2} \ , \tag{D.1}$$

where $\mathcal{O}$ is an observable for configuration x_s at the s-th step within the Markov process. Note, every step corresponds to a loop update. N denotes the number of considered data points. One expects that the autocorrelation function decays as [40]

$$C_0(t) \propto \exp\left(-t/\tau_0\right) \ . \tag{D.2}$$

The efficiency of the updating scheme is determined by the length of the loops. The loop length is defined as the number of vertices involved in the loop.

D.1 Correlation Time for BHM

Fig. D.1(a) presents a distribution of the length of the loops for various couplings in the bilayer Heisenberg model. As apparent the length of the loops on average increases for decreasing coupling. Furthermore, the quantum critical point located at $J_\perp/J_\parallel = -2.525$ [78] is visible by an abrupt increase of the mean loop length as shown in Fig. D.1(b). For $J_\perp \to 0$ the average length of the loops extends almost to the maximal length corresponding to the number of plaquettes [see Fig. D.1(b)]:

$$2 \times 16 \times 16 \times 50 \times \frac{1}{0.05} = 0.512 \times 10^6 \ . \tag{D.3}$$

Since the loops are much longer in the low coupling region than for large couplings the configurations should change faster such that the autocorrelation time decreases. The correlation time obtained via the spin stiffness can be see in Fig. D.2. Even in the vicinity of the critical coupling the correlation time is below $\tau_0 \sim 10$.

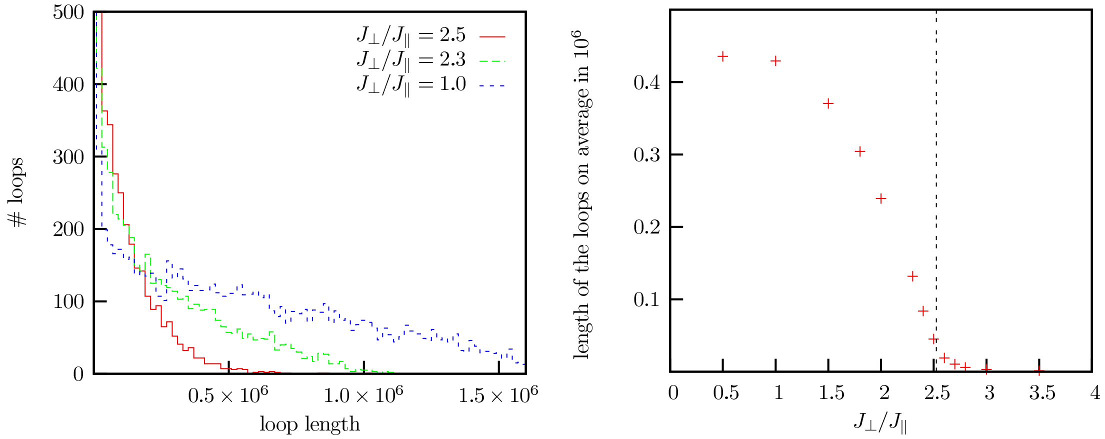

(a) Distribution of loop length

(b) Loop length on average

Figure D.1: (a) Distribution of the loop length for various couplings in the bilayer Heisenberg model. The length of the loop is defined as the number of vertices involved in the loop. Each data sample includes 10 000 loops. (b) Length of the loop on average. The black dashed line indicates the quantum critical point. Simulations are carried out on a 16×16 lattice at $\beta J_\parallel = 50.0$ ($\Delta\tau J_\parallel = 0.05$).

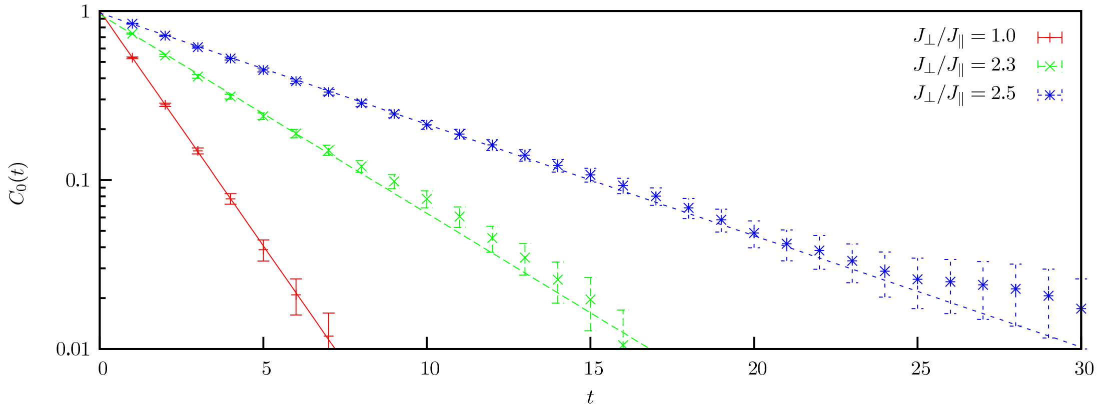

Figure D.2: Autocorrelation function as defined in Eq. (D.1) for various couplings on a 16×16 lattice at $\beta J_\parallel = 50.0$ ($\Delta\tau J_\parallel = 0.05$). The data are fitted according to Eq. (D.2). The fits yield the following autocorrelation times: $\tau_0 \simeq 1.6$ for $J_\perp/J_\parallel = 1.0$, $\tau_0 \simeq 3.7$ for $J_\perp/J_\parallel = 2.3$ and $\tau_0 \simeq 6.6$ for $J_\perp/J_\parallel = 2.5$.

D.2 Correlation Time for the 1D Kondo Necklace

In Fig. D.3(a) the distribution of the loop length depending on the interchain coupling $J_\perp$ for the 1D Kondo Necklace model is shown. As apparent, the distribution does not change noticeably as a function of $J_\perp$. The loop length on average is roughly constant over the considered coupling range ($0.2 \leq |J_\perp|/J_\parallel \leq 1.0$) [see Fig. D.3(b)]. This is also reflected in the correlation length. In Fig. D.4 the correlation length determined via the total energy is depicted. It does not change greatly with $J_\perp$ and is approximately given by $\tau_0 \sim 10$.

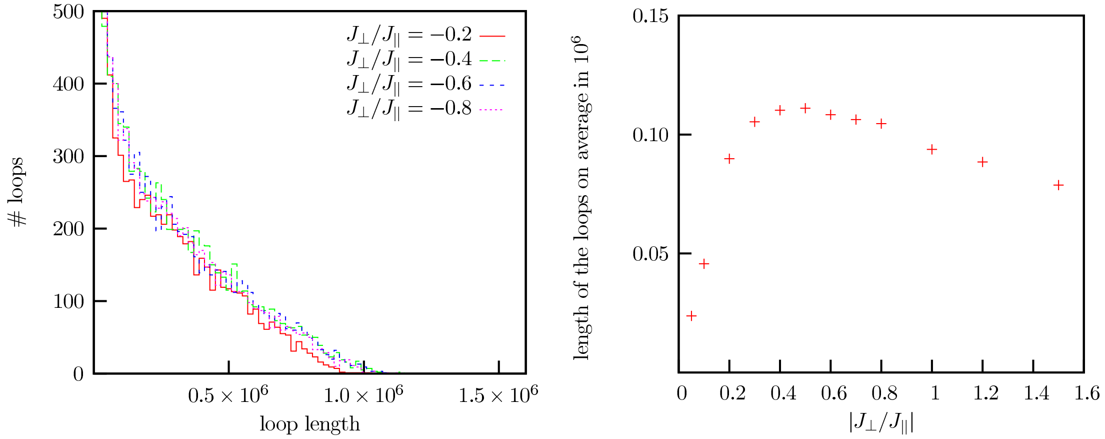

(a) Distribution of loop length

(b) Loop length on average

Figure D.3: (a) Distribution of the loop length for various couplings in the 1D Kondo necklace. The length of the loop is defined as the number of vertices which are passed through within one loop. Each data sample includes 10 000 loops. (b) Length of the loop on average. Simulations are carried out on a 2×50 lattice at $\beta J_\parallel = 50.0$ ($\Delta\tau J_\parallel = 0.02$).

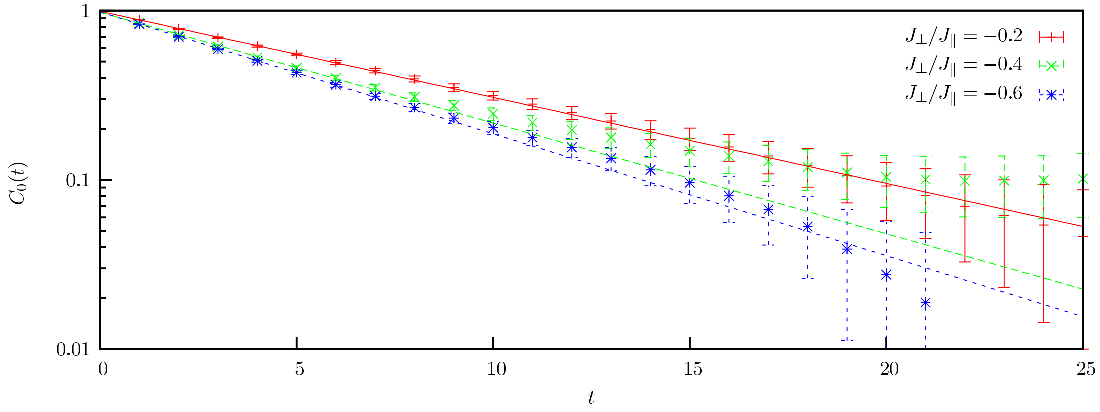

Figure D.4: Autocorrelation function as defined in Eq. (D.1) for various couplings on a 2×50 lattice at $\beta J_\parallel = 50.0$ ($\Delta\tau J_\parallel = 0.02$). The data are fitted according to Eq. (D.2). The fits yield the following autocorrelation times: $\tau_0 \simeq 8.5$ for $J_\perp/J_\parallel = -0.2$, $\tau_0 \simeq 6.6$ for $J_\perp/J_\parallel = -0.4$ and $\tau_0 \simeq 6.0$ for $J_\perp/J_\parallel = -0.6$.

Acknowledgments

I wish to thank Fakher F. Assaad for giving me the opportunity to take part in interesting and exciting research, for his friendly support in carrying out this work and the generous time he spent answering all my questions.

I have greatly profited from discussions with my PhD colleagues Lee C. Martin and Thomas C. Lang.

I also thank Sylvain Capponi, Fabien Alet, Dmitry N. Aristov and Mikhail N. Kiselev for their contribution to the work on the spiral staircase Heisenberg model.

I thank the DFG for financial support under grant numbers AS120/4-1 and AS120/4-2 and the LRZ Munich for allocation of supercomputer facilities.

I am also grateful to my parents and Katharina who gave all support outside of physics.

Bibliography

[1] E. Dagotto, *Correlated electrons in high-temperature superconductors*, Rev. Mod. Phys. **66**, 763 (1994). 1, 1, 4.3, 6.2

[2] C. R. Stewart, *Heavy-fermion systems*, Rev. Mod. Phys. **56**, 755 (1984). 1

[3] A. C. Hewson, *The Kondo Problem to Heavy Fermions*, Vol. 2 of *Cambridge Studies in Magnetism* (Cambridge University Press, Cambridge, UK, 1993). 1

[4] J. Hubbard, *Electron Correlations in Narrow Energy Bands*, Proc. Roy. Soc. **A276**, 238 (1963). 1

[5] N. W. Ashcroft and N. D. Mermin, *Solid State Physics* (Thomson Learning, London, 1976). 1, 5.3.2

[6] W. Pauli, *Exclusion principle and quantum mechanics*, Nobel Lecture, 1946. 1, 1

[7] W. Nolting, *Viel-Teilchen-Theorie*, Vol. 7 of *Grundkurs Theoretische Physik*, 5 ed. (Springer-Verlag, Berlin Heidelberg, 2002). 1, 5.4, 5.4.2

[8] E. H. Lieb and F. Y. Wu, *Absence of Mott Transition in an Exact Solution of the Short-Range, One-Band Model in One Dimension*, Phys. Rev. Lett. **20**, 1445 (1968). 1

[9] E. H. Lieb and F. Y. Wu, *The one-dimensional Hubbard model: a reminiscence*, Physica A **321**, 1 (2003). 1

[10] K. A. Chao, J. Spałek, and A. M. Oleś, *Canonical pertubation expansion of the Hubbard model*, Phys. Rev. B **18**, 3453 (1978). 1

[11] A. Auerbach, *Interacting Electrons and Quantum Magnetism*, 1 ed. (Springer-Verlag, Berlin Heidelberg New York, 1994). 1, 1, 3.3

[12] J. Jaklič and P. Prelovšek, *Finite-temperature properties of doped antiferromagnets*, Adv. in Physics **49**, 1 (2000). 1

[13] F. C. Zhang and T. M. Rice, *Effective Hamiltonian for the superconducting Cu oxides*, Phys. Rev. B **37**, 3759 (1988). 1

[14] W. Heisenberg, *Über den anschaulichen Inhalt der quantentheoretischen Kinematik und Mechanik*, Zeitschrift für Physik **43**, 172 (1927). 1

[15] F. Hund, *Atomtheoretische Deutung des Magnetismus der seltenen Erden*, Zeitschrift für Physik **33**, 855 (1925). 1

[16] M. A. Ruderman and C. Kittel, *Indirect Exchange Coupling of Nuclear Magnetic Moments by Conduction Electrons*, Phys. Rev. **96**, 99 (1954). 1, 5.4.1, 6.2

[17] C. Kittel, *Quantum Theory of Solids* (John Wiley & Sons, Inc., New York London Sydney, 1963). 1, 5.2.2, 5.4.1, 6.2

[18] T. Kasuya, *A Theory of Metallic Ferro- and Antiferromagnetism on Zener's Model*, Progress of theoretical physics **16"**, 45 (1956). 1, 5.4.1, 6.2

[19] K. Yosida, *Magnetic Properties of Cu-Mn Alloys*, Phys. Rev. **106**, 893 (1957). 1, 5.4.1, 6.2

[20] J. R. Schrieffer and P. A. Wolff, *Relation between the Anderson and Kondo Hamiltonians*, Phys. Rev. **149**, 491 (1966). 1

[21] H. Tsunetsugu, M. Sigrist, and K. Ueda, *The ground-state phase diagram of the one-dimensional Kondo lattice model*, Rev. Mod. Phys. **69**, 809 (1997). 1, 5.3.2

[22] S. Capponi and F. F. Assaad, *Spin and charge dynamics of the ferromagnetic and antiferromagnetic two-dimensional half-filled Kondo lattice model*, Phys. Rev. B **63**, 155114 (2001). 1, 5.3.2

[23] M. Feldbacher, C. Jurecka, F. F. Assaad, and W. Brenig, *Single-hole dynamics in the half-filled two-dimensional Kondo-Hubbard model*, Phys. Rev. B **66**, 45103 (2002). 1, 5.3.2

[24] F. D. M. Haldane, *Nonlinear Field Theory of Large-Spin Heisenberg Antiferromagnets: Semiclassically Quantized Solitons of the One-Dimensional Easy-Axis Néel State*, Phys. Rev. Lett. **50**, 1153 (1983). 1, 2.4, 6

[25] I. Affleck and E. H. Lieb, *A proof of part of Haldane's conjecture on spin chains*, Lett. Math. Phys. **12**, 57 (1986). 1

[26] M. P. Nightingale and H. W. J. Blöte, *Gap of the linear spin-1 Heisenberg antiferromagnet: A Monte Carlo calculation*, Phys. Rev. B **33**, 659 (1986). 1, 2.4

[27] M. Takahashi, *Monte Carlo calculation of elementary excitation of spin chains*, Phys. Rev. Lett. **62**, 2313 (1989). 1, 2.4

[28] J. Deisz, M. Jarrell, and D. L. Cox, *Dynamical properties of one-dimensional antiferromagnets: A Monte Carlo study*, Phys. Rev. B **48**, 10227 (1993). 1, 2.4

[29] S. Todo and K. Kato, *Cluster Algorithms for General-S Quantum Spin Systems*, Phys. Rev. Lett. **87**, 47203 (2001). 1, 2.4, 6.3, 6.3.2, 6.12

[30] M. N. Kiselev, D. N. Aristov, and K. Kikoin, *Spin gap in a spiral staircase model*, Physica B **359-361**, 1406 (2005). 1, 6

[31] M. N. Kiselev, D. N. Aristov, and K. Kikoin, *Spin gap in chains with hidden symmetries*, Phys. Rev. B **71**, 92404 (2005). 1, 6

[32] D. N. Aristov, M. N. Kiselev, and K. Kikoin, *Single-pole ladder at quater filling*, Phys. Rev. B **75**, 224405 (2007). 1

[33] F. H. L. Essler, T. Kuzmenko, and I. A. Zaliznyak, *Luttinger liquid coupled to quantum spins: Flow equation approach to the Kondo necklace model*, Phys. Rev. B **76**, 115108 (2007). 1

[34] Y. Hosokoshi, Y. Nakazawa, K. Inoue, K. Takizawa, H. Nakano, M. Takahashi, and T. Goto, *Magnetic properties of low-dimensional quantum spin systems made of stable organic biradicals PNNNO, F_2PNNNO and PIMNO*, Phys. Rev. B **60**, 12924 (1999). 1.1, 1

[35] D. G. Shelton, A. A. Nersesyan, and A. M. Tsvelik, *Antiferromagnetic spin ladders: Crossover between spin S=1/2 and S=1 chains*, Phys. Rev. B **53**, 8521 (1996). 1, 6.1.1, 6.2

[36] H. Suhl, *Effective Nuclear Spin Interactions in Ferromagnets*, Phys. Rev. **109**, 606 (1957). 1, 6.2

[37] T. Nakamura, *Indirect Coupling of Nuclear Spins in Antiferromagnet with Particular Reference to MnF_2 at Very Low Temperature*, Progr. Theor. Phys. **20**, 542 (1958). 1, 6.2

[38] D. N. Aristov, S. V. Maleyev, M. Guillaume, A. Furrer, and C. J. Carlile, *Additional raising of the degeneracy of CEF-split Ho^{3+} ions by antiferromagnetic spin-waves in $Ho_{0.1}Y_{0.9}Ba_2Cu_3O_{6.3}$*, Z. Phys. B **95**, 291 (1994). 1, 6.2

[39] H. G. Evertz, *The loop algorithm*, Adv. in Phys. **52**, 1 (2003). 1, 3.1, 3.2, 6.3

[40] F. Assaad, in *Quantum Simulations of Complex Many-Body Systems: From Theory to Algorithms*, edited by J. Grotendorst, D. Marx, and A. Muramatsu (NIC-Directors, Jülich, Germany, 2002), pp. 99–155. 1, 3.1, D

[41] E. W. Kolb and M. S. Turner, *The Early Universe* (Addison-Wesley, Redwood City, CA, 1990). 2

[42] J. J. Binney, N. J. Dowrick, A. J. Fisher, and M. E. J. Newman, *The Theory of Critical Phenomena* (Oxford University Press, Oxford, 2002). 2

[43] F. Schwabl, *Statistical Mechanics* (Springer-Verlag, Berlin Heidelberg, 2002). 2.1

[44] J. M. Yeomans, *Statistical Mechanics of Phase Transitions* (Clarendon Press, Oxford, U.K., 1992). 2.1

[45] L. P. Kadanoff, in *Proceedings of the Enrico Fermi Summer School of Physics*, edited by M. S. Green (Academic Press, London and New York, 1971), p. 100. 2.1

[46] K. G. Wilson, *Renormalization Group and Critical Phenomena. I. Renormalization Group and the Kadanoff Scaling Picture*, Phys. Rev. B **4**, 3174 (1971). 2.1

[47] K. G. Wilson, The Renormalization Group and Critical Phenomena, Nobel lecture, 1982. 2.1

[48] S. L. Sondhi, S. M. Girvin, J. P. Carini, and D. Shahar, *Continuous quantum phase transitions*, Rev. Mod. Phys. **69**, 315 (1997). 2.2

[49] M. Vojta, *Quantenphasenübergänge - "Schmelzen" am Temperaturnullpunkt*, Physik Journal **1**, 55 (2002). 2.2, 2.2

[50] M. Vojta, *Quantum phase transitions*, Rep. Prog. Phys. **66**, 2069 (2003). 2.2, 2.2

[51] D. Belitz and T. R. Kirkpatrick, in *Dynamics: Models and Kinetic Methods for Non-Equilibrium Many Body Systems*, edited by J. Karkheck (Kluwer, Dordrecht, 2000), p. 399, cond-mat/9811058 (1998). 2.2

[52] T. R. Kirkpatrick and D. Belitz, in *Electron Correlation in the Solid State*, edited by H. March (Imperial College Press, London, 1999), pp. 297–370, cond-mat/9707001 (1997). 2.2

[53] H. Bethe, *Eigenwerte und Eigenfunktionen der linearen Atomkette*, Zeitschrift für Physik **71**, 205 (1931). 2.3, 2.4

[54] N. D. Mermin and H. Wagner, *Absence of Ferromagnetism or Antiferromagnetism in One- or Two-Dimensional Isotropic Heisenberg Models*, Phys. Rev. Lett. **17**, 1133 (1966). 2.3

[55] E. Lieb, T. Schultz, and D. Mattis, *Two soluble models of an antiferromagnetic chain*, Ann. of Phys. **16**, 407 (1961). 2.4

[56] J. des Cloizeaux and J. J. Pearson, *Spin-Wave Spectrum of the Antiferromagnetic Linear Chain*, Phys. Rev. **128**, 2131 (1962). 2.4, 6.2

[57] E. Lieb and D. Mattis, *Ordering Energy Levels of Interacting Spin Systems*, J. Math. Phys. **3**, 749 (1962). 2.4

[58] D. C. Mattis, *The Theory of Magnetism*, Vol. 17 of *Solid-State Sciences* (Springer Verlag, Berlin and Heidelberg, 1981). 2.4

[59] I. Affleck, T. Kennedy, E. H. Lieb, and H. Tasaki, *Rigorous results on valence-bond ground states in antiferromagnets*, Phys. Rev. Lett. **59**, 799 (1987). 2.4, 2.4, 6.3.3

[60] I. Affleck, T. Kennedy, E. H. Lieb, and H. Tasaki, *Valence bond ground states in isotropic quantum antiferromagnets*, Commun. Math. Phys. **115**, 477 (1988). 2.4, 6.3.3

[61] M. den Nijs and K. Rommelse, *Preroughening transitions in crystal surfaces and valence-bond phases in quantum spin chains*, Phys. Rev. B. **40**, 4709 (1989). 2.4, 2.4

[62] K. Rommelse and M. P. M. den Nijs, *Preroughening Transitions in Surfaces*, Phys. Rev. Lett. **59**, 2578 (1987). 2.3, 2.4

[63] D. Reiter, in *The Monte Carlo Method, an Introduction*, edited by H. Fehske, R. Schneider, and A. Weiße (Springer Verlag, Greifswald, Germany, 2007), pp. 99–155, in press. 3

[64] M. Troyer and U.-J. Wiese, *Computational Complexity and Fundamental Limitations to Fermionic Quantum Monte Carlo Simulations*, Phys. Rev. Lett. **94**, 170201 (2005). 3

[65] R. Blankenbecler, D. J. Scalapino, and R. L. Sugar, *Monte Carlo calculations of coupled boson-fermion systems. I*, Phys. Rev. D **24**, 2278 (1981). 3

[66] J. E. Hirsch and R. M. Fye, *Monte Carlo Method for Magnetic Impurities in Metals*, Phys. Rev. Lett. **56**, 2521 (1986). 3

[67] J. F. Corney and P. D. Drummond, *Gaussian Qunatum Monte Carlo Methods for Fermions and Bosons*, Phys. Rev. Lett. **93**, 260401 (2004). 3

[68] F. F. Assaad, P. Werner, P. Corboz, E. Gull, and M. Troyer, *Symmetry projection schemes for Gaussian Monte Carlo methods*, Phys. Rev. B **72**, 224518 (2005). 3

[69] R. M. Fye, *New results on Trotter-like approximations*, Phys. Rev. B **33**, 6271 (1986). 3.1

[70] A. Angelucci, *Effective lattice actions for correlated electrons*, Phys. Rev. B **51**, 11580 (1995). 3.3

[71] M. Brunner, F. F. Assaad, and A. Muramatsu, *Single hole dynamics in the one-dimensional t-J model*, Eur. Phys. J. B **16**, 209 (2000). 3.3, 5.3.2, 5.4.2

[72] M. Brunner, F. F. Assaad, and A. Muramatsu, *Single hole dynamics in the t-J model on a square lattice*, Phys. Rev. B **62**, 15480 (2000). 3.3

[73] E. R. Gagliano and C. A. Balseiro, *Dynamical Properties of Quantum Many-Body Systems at Zero Temperature*, Phys. Rev. Lett. **59**, 2999 (1987). 4.3

[74] M. Aichhorn, PhD thesis: *Ordering Phenomena in Strongly-Correlated Systems: Cluster Pertubation Theory Approaches*, Technische Universität Graz, 2004. 4.3

[75] E. Manousakis, *The spin-1/2 Heisenberg antiferromagnet on a square lattice and its applications to the cuprous oxides*, Phys. Mod. Phys. **63**, 1 (1991). 5

[76] M. Troyer, M. Imada, and K. Ueda, *Critical exponents of the quantum phase transition in a planar antiferromagnet.*, J. Phys. Soc. Jpn. **66**, 2957 (1997). 5.1

[77] W. Brenig, *Finite-temperature properties of the two-dimensional SU(2) Kondo necklace*, Phys. Rev. B **73**, 104450 (2006). 5.1

[78] P. V. Shevchenko, A. W. Sandvik, and O. P. Sushkov, *Double-layer Heisenberg antiferromagnet at finite temperature: Brueckner theory and quantum Monte Carlo simulations*, Phys. Rev. B **61**, 3475 (2000). 5.1, 5.2.1, D.1

[79] V. N. Kotov, O. Sushkov, Z. Weihong, and J. Oitmaa, *Novel Approach to Description of Spin-Liquid Phases in Low-Dimensional Qunatum Antiferromagnets*, Phys. Rev. Lett. **80**, 5790 (1998). 5.1

[80] L. Wang, K. S. D. Beach, and A. W. Sandvik, *High-precision finite-size scaling analysis of the quantum-critical point of S=1/2 Heisenberg antiferromagnetic bilayers*, Phys. Rev. B **73**, 14431 (2006). 5.1

[81] K. S. D. Beach, *Identifying the maximum entropy method as a special limit of stochastic analytic continuation*, (arXiv:cond-mat/0403055), 2004. 5.2.1, 5.3.2, 6.3

[82] S. Sachdev and R. N. Bhatt, *Bond-operator representation of quantum spins: Mean-field theory of frustrated quantum Heisenberg antiferromagnets*, Phys. Rev. B **41**, 9323 (1990). 5.2.2, 5.2.2, 5.2.2

[83] T. Sommer, M. Vojta, and K. W. Becker, *Magnetic properties and spin waves of bilayer magnets in a uniform field*, Eur. Phys. J. B **23**, 329 (2001). 5.2.2

[84] M. Brunner, Ph.D. thesis, Universität Stuttgart, 2000. 5.3.2

[85] G. Martínez and P. Horsch, *Spin polarons in the t-J model*, Phys. Rev. B **44**, 317 (1991). 5.3.2

[86] M. Vojta and K. W. Becker, *Doped bilayer antiferromagnets: Hole dynamics on both sides of a magnetic ordering transition.*, Phys. Rev. B **60**, 15201 (1999). 5.3.2

[87] G. D. Mahan, *Many-Particle Physics*, 2 ed. (Plenum Press, New York and London, 1990). 5.4, 5.4.2

[88] C. Brünger, Diploma thesis: *Loch-Dynamik nahe eines magnetische Quanten-Phasenübergangs im biplanaren Heisenberg Modell*, Universität Würzburg, 2004. 5.4, 5.4.2

[89] O. P. Sushkov, *Spin-1/2 magnetic impurity in a two-dimensional magnetic system close to a quantum critical point*, Phys. Rev. B **62**, 12135 (2000). 5.4.1

[90] S. Sachdev, M. Troyer, and M. Vojta, *Spin Orthogonality Catastrophe in Two-Dimensional Antiferromagnets and Superconductors*, Phys. Rev. Lett. **86**, 2617 (2001). 5.13(a), 5.4.2, 5.4.2

[91] C. Brünger, F. F. Assaad, S. Capponi, F. Alet, M. N. Kiselev, and D. N. Aristov, *Twisting Ferromagnetic Spin Ladders*, to be submitted for publication in Phys. Rev. B. 6

[92] M. Azzouz, L. Chen, and S. Moukouri, *Calculation of the singlet-triplet gap of the antiferromagnetic Heisenberg model on a ladder*, Phys. Rev. B **50**, 6233 (1994). 6.1.1

[93] D. N. Aristov, *Bosonization for a Wigner-Jordan-like transformation: Backscattering and umklapp processes on a fictitious*, Phys. Rev. B **57**, 12825 (1998). 6.1.1

[94] T. S. Nunner and T. Kopp, *Jordan-Wigner approach to dynamic correlations in spin ladders*, Phys. Rev. B. **69**, 104419 (2004). 6.1.1

[95] S. Larochelle and M. Greven, *Susceptibilities and spin gap of weakly coupled spin ladders*, Phys. Rev. B. **69**, 92408 (2004). 6.1.1, 6.2, 6.3.2

[96] C. Lanczos, *An Iteration Method for the Solution of the Eigenvalue Problem of Linear Differential and Integral Operators*, J. Research Nat. Bureau Standards **45**, 255 (1950). 6.2

[97] C. Brünger, F. F. Assaad, F. Alet, S. Capponi, M. N. Kiselev, and D. N. Aristov, *Spin gap and string order parameter in the ferromagnetic Spiral Staircase Heisenberg Ladder: a quantum Monte Carlo study*, accepted for publication in Phys. Rev. Lett. (arXiv:cond-mat/0706.2769) Article is expected to be published in the January 11, 2008 issue. 6.2, 6.3

[98] A. Sandvik, *Stochastic method for analytic continuation of quantum Monte Carlo data*, Phys. Rev. B **57**, 10287 (1998). 6.3

[99] F. Alet, P. Dayal, A. Grzesik, A. Honecker, M. Körner, A. Läuchli, S. R. Manmana, I. P. McCulloch, F. Michel, R. M. Noack, G. Schmid, U. Schollwöck, F. Stöckli, S. Todo, S. Trebst, M. Troyer, P. Werner, and S. Wessel, *The ALPS Project: open source software for strongly correlated systems*, J. Phys. Soc. Jpn. Suppl. **74**, 30 (2005). 6.3, 6.3.2

[100] M. Troyer, B. Ammon, and E. Heeb, in *Computing in Object-Oriented Parallel Environments*, Vol. 1505 of *LNCS*, edited by D. Caromel, R. R. Oldehoeft, and M. Tholburn (Springer-Verlag, Berlin Heidelberg, 1998), pp. 191–198. 6.3, 6.3.2

[101] F. Cooper, B. Freedman, and D. Preston, *Solving* $\phi^4_{1,2}$ *field theory with Monte Carlo*, Nucl. Phys. B **210**, 210 (1982). 6.3

[102] A. Nieto, *Evaluating sums over the Matsubara frequencies*, Computer Physics Communications **92**, 54 (1995), (arXiv:hep-ph/9311210). A

Curriculum Vitae

Personal Details

Name:	Christian Brünger
Date of Birth:	May 5, 1978
Place of Birth:	Bad Oeynhausen, Germany
Nationality:	German

Education

09/2004 - 01/2008	**Julius-Maximilians-Universität Würzburg** PhD work at Institut für Theoretische Physik und Astrophysik Thesis: *Numerical Studies of Quantum Spin Systems* Supervisor: Prof. Dr. Fakher F. Assaad Würzburg, Bavaria (Germany)
08/2001 - 05/2002	**State University of New York at Albany** — Master of Science — Graduate student at SUNY at Albany, New York (USA)
10/1998 - 07/2004	**Julius-Maximilians-Universität Würzburg** — Diplom — Diploma thesis: *Loch-Dynamik nahe eines magnetischen Quanten-Phasenübergangs im biplanaren Heisenberg Modell* Supervisor: Prof. Dr. Fakher F. Assaad Würzburg, Bavaria (Germany)
08/1988 - 05/1997	**Immanuel-Kant-Gymnasium** — Abitur — Bad Oeynhausen, North Rhine-Westphalia (Germany)